The Dissertation Committee for Kang Luo Certifies that this is the approved version of the following dissertation:

Electron Transport in Nanoparticle Single-Electron Transistors

Committee:

Zhen Yao, Supervisor

Alejandro L. de Lozanne

John T. Markert

Qian Niu

Li Shi

Electron Transport in Nanoparticle Single-Electron Transistors

by

Kang Luo, B.A.; M.S.

Dissertation

Presented to the Faculty of the Graduate School of
The University of Texas at Austin
in Partial Fulfillment
of the Requirements
for the Degree of

Doctor of Philosophy

The University of Texas at Austin
December 2007

Dedication

This dissertation is dedicated to my father, Yirong Luo, my mother, Cuibi Kang and my wife, Jingyu Wang

Acknowledgements

Scientific research to pursue Ph.D is not something that can be done alone. At the end of my 6 year graduate research, I do believe that my Ph.D work would never have been possible without others' help and encouragement. I want to take opportunity to express my gratitude to all the people for their generous help and support.

Most of all, I would have my first appreciation to my advisor Professor Zhen Yao for his continuous advice, encouragement and support. I thank him for giving me the chance to explore the transport physics in nanometer scale world and guiding me to realize research work from a scratch. His advice and discussion have helped to expand my interest in physics; his encouragement and support have been the most critical driving force to continue my Ph.D. I would like to thank Professor Qian Niu for his helpful discussion to understand my research results deeply. I am also grateful to Professor Alex de Lozanne, Professor John T. Markert and Professor Li Shi for their serving as my committee members.

I am also indebted to many collaborators for their help in my Ph.D research. They are Dr. Dong-Hun Chae, Dr. Suyong Jung and Professor Saiful I. Khondaker in our group, Professor Chih-Kang Shih (UT at Austin), Professor Brian Korgel (UT at Austin), and Professor Paul F. Barbara (UT at Austin).

I would also like to say thanks to my friends at Austin for their help and discussion in my research. They are Daejin Eom, Junwei Huang, Wei Lu, Shengyong Qin, Yong J Lee, Zhiquan Luo, Frank-Liang Wang, Di Xiao, Shuqiang Yang, and Jianhua Zhou.

Finally, I want to thank my parents, sister and wife for their precious love and persistent encouragement all the way in my life.

Electron Transport in Nanoparticle Single-Electron Transistors

Publication No._____________

Kang Luo, Ph.D
The University of Texas at Austin, 2007

Supervisor: Zhen Yao

Electron transport in nanoparticle single-electron transistors (SETs) is a fruitful method to explore a wide range of physical phenomena at the nanometer scale. In this thesis, we investigate electron transport in SETs incorporating various nanoparticles, including gold nanoparticles in both classical and quantum regimes and Pb nanoparticle in both superconducting and normal states.

SETs have been successfully fabricated by incorporating individual gold nanoparticles into the gaps between two electrodes. Although single-electron tunneling behavior is prominent, quantized energy levels cannot be resolved in these SETs due to their relatively large particle sizes. A novel method has been developed to achieve SETs incorporating gold nanoparticles whose sizes are small enough to resolve discrete quantum energy levels. The devices consist of spontaneously-formed ultrasmall gold nanoparticles linked by alkanedithiols to gold electrodes. The devices reproducibly exhibit addition energies of a few hundred meV, which enables the observation of single-electron tunneling at room temperature. At low temperatures, resonant tunneling through discrete energy levels in the Au nanoparticles is observed, which is accompanied by the excitations of molecular vibrations at large bias voltage.

Having explored the SETs in normal state, we have extended the experiments to superconducting single-electron transistors (SSETs). We first fabricated and characterized Pb superconducting electrodes with nanometer-sized separation. Our observation clearly shows that conventional Barden-Cooper-Schrieffer theory remains valid to interpret the tunneling behavior between two nanometer-spaced Pb electrodes. Furthermore, by incorporating Pb nanoparticles between the two Pb electrodes, we have fabricated SSETs and investigated the transport properties of these devices. In the superconducting state, the conductance is suppressed by a combination of the single-electron tunneling effect and the absence of density of states within the superconducting gap. In the suppression regime, the tunneling spectroscopy shows current features that arise from quasiparticle tunneling caused by singularity matching. At low temperature, the features can only be observed for odd charge states in SSETs. At high temperature, the odd-even parity effect is smeared out. Upon application of a magnetic field, the superconducting state is suppressed and single-electron tunneling behavior for normal metallic nanoparticles is recovered.

Table of Contents

List of Tables xi

List of Figures xii

Chapter 1 Introduction and Background 1

1.1 Background 1

1.2 General Features of Single-Electron Transistors 2

1.3 Previous Approaches to Single-Electron Transistors 5

1.4 Organization of the Thesis 6

References 8

Chapter 2 Single-Electron Tunneling Effect 12

2.1 Introduction 12

2.2 Classical Coulomb Blockade 13

2.3 Quantum Coulomb Blockade 17

2.4 Superconducting Single-Electron Tunneling Effect 22

References 26

Chapter 3 Fabrication of Gold Single-Electron Transistors 27

3.1 Introduction 27

3.2 Electrostatic Trapping of Gold Nanoparticles 28

3.3 Physical Deposition of Gold Nanoparticles 32

3.4 Self-Assembly of Colloidal Gold Nanoparticle 36

3.5 Comparison 37

3.6 Summary 39

References 40

Chapter 4 Room-Temperature Single-Electron Transistors Using Alkanedithiols 42

4.1 Introduction 42

4.2 Device Fabrication 43

4.3 Experimental Results and Discussion 44

4.4 Summary 53
References 54

Chapter 5 Fabrication of Superconducting Electrodes 57
5.1 Introduction 57
5.2 Device Fabrication 58
5.3 Experimental Results and Discussion 61
5.4 Summary 65
References 67

Chapter 6 Superconducting Single-Electron Transistors 69
6.1 Introduction 69
6.2 Device Fabrication 70
6.3 Sequential Tunneling of Quasiparticles 72
6.4 Singularity Matching 77
6.5 Odd-Even Effect 81
6.6 Summary 84
References 85

Chapter 7 Ongoing Project: Single-Molecule Transistors 87
7.1 Introduction 87
7.2 Device Fabrication 88
7.3 Experimental Results and Discussion 89
References 95

Chapter 8 Summary 97

Vita 99

List of Tables

Table 4.1: The excitation energies observed in Figure 4.2 46

List of Figures

Figure 1.1: Schematic diagram of a single-electron transistor. 3

Figure 1.2: Previous approaches to SETs. 6

Figure 2.1: Equivalent circuit of an SET. 14

Figure 2.2: Classical Coulomb blockade effect. 16

Figure 2.3: Coulomb blockade effect and Coulomb oscillations. 18

Figure 2.4: Quantum Coulomb blockade effect. 20

Figure 2.5: Superconductor-superconductor tunneling junction. 22

Figure 2.6: Superconducting single-electron tunneling effect. 24

Figure 3.1: Electrostatic trapping method to fabricate gold nanoparticle SETs in combination with electromigration technique. 29

Figure 3.2: Two-dimensional plot of differential conductance as a function of bias voltage and gate voltage of a gold nanoparticle SET fabricated by using electrostatic trapping method. 31

Figure 3.3: Gold nanoparticle SETs fabricated by using the physical deposition of gold nanoparticles. 33

Figure 3.4: Two-dimensional plot of differential conductance as a function of bias voltage and gate voltage of a gold nanoparticle SET fabricated by using physical deposition of gold nanoparticles. 35

Figure 3.5: Nanoparticle SETs fabricated by using the self-assembly of colloidal gold nanoparticles. 38

Figure 4.1: Representative *I–V* characteristics from a device incorporating C6 molecules at different gate voltages measured at 4.2 K. 43

Figure 4.2: Two-dimensional color plot of differential conductance as a function of bias voltage and gate voltage measured at 4.2 K from the same C6 device as shown in figure 4.1...45
Figure 4.3: Histogram of the observed excitation energies from 22 devices......47
Figure 4.4: (a) Schematic of our proposed device geometry. (b) Energy level diagram for the transport processes. 49
Figure 4.5: (a) Current as a function of gate voltage measured with a bias voltage of 0.5 mV at 6.2 K from the same C6 device as shown in figure 4.1. (b) Current peak height at Vg = -0.5 V as a function of temperature. 51
Figure 4.6: Color plots of differential conductance versus bias and gate voltages from the same device as shown in figure 4.1 measured at different temperatures..52
Figure 5.1: (a) Representative conductance trace during the electromigration process. (b) *I*-*V* characteristics between the Pb electrodes after electromigration at 4.2 K in different magnetic fields.....................59
Figure 5.2: *I*-*V* curves between nanometer-spaced Pb electrodes at different temperatures..62
Figure 5.3: (a) Measured superconducting energy gaps at various temperatures normalized to the gap value at 1.8 K as a function of temperature scaled by T_c. (b) Measured quasiparticle lifetime as a function of temperature scaled by energy gap...64

Figure 5.4: (a) *I*-*V* curve between nanometer-spaced Pb elelctrodes (sample A). (b) differential conductance versus bias voltage from sample A. (c) Second derivative d^2I/d^2V as a function of bias voltage from sample A...66

Figure 6.1: (a) Schematic diagram of an SSET. (b) Schematic energy diagram.71

Figure 6.2: Representative *I*-*V* characteristics from sample #1 at different gate voltages measured at 4.2 K. 72

Figure 6.3: Two-dimensional color plot of conductance as a function of bias voltage and gate voltage from (a) sample #1, (b) sample #2 at *T* = 4.2 K and zero *B* fields and (c) sample #1 at *T* = 4.2 K and *B* = 1.9 T...74

Figure 6.4: Schematic energy diagrams of various quasiparticle tunneling processes. 75

Figure 6.5: Thresholds of various quasiparticle tunneling processes in SSETs..77

Figure 6.6: Two-dimensional color plot of conductance as a function of bias voltage and gate voltage from (a) sample #1, and (b) sample #2 at *T* = 4.2 K and zero *B* fields in the low bias region to clarify the fine features in suppression regimes. 79

Figure 6.7: Two-dimensional plot of differential conductance as a function of bias voltage and gate voltage at *T* = 2 K...83

Figure 7.1: Schematic of a Co-porphyrin single-molecule transistor with superconducting electrodes...89

Figure 7.2: Two-dimensional color plot of conductance as a function of bias voltage and gate voltage from a Co-porphyrin SMT with superconducting electrodes at *T* = 4.2 K with (a) *B* = 0 T (b) *B* = 0.6 T. 92

Figure 7.3: Differential conductance as a function of gate voltage from a Co-SMT with superconducting electrodes at various temperatures and magnetic fields. 94

Chapter 1: Introduction and Background

1.1 BACKGROUND

In the past several decades, the semiconductor industry has been able to successfully follow Moore's law to double the number of transistors on a chip every two years. Through the continuous development of very large-scale integration technology, state-of-the-art microprocessors contain more than 1 billion transistors, with transport channel lengths less than 50 nm. At this length scale, the operation model based on classical physics may not remain valid since it approaches some quantum characteristic length scales such as the electron mean free path. Quantum physics corrections, like ballistic transport mechanism, have been adopted for a more accurate understanding of the transistor performance.

However, as the transistors scale down to below 100 nm, the miniaturization process is confronting several severe limitations. First, the wavelength of UV light used in current optical lithography tools is 193 nm. This wavelength sets the fundamental limit of the resolution of current optical lithography and makes it unfeasible to pattern structures with dimensions smaller than 10 nm. Secondly, as the density of transistors on a chip increases to ~1 billion per chip, the density of power consumed by transistors is approaching up to 100 W/cm^2. The conventional air cooling method is no longer an effective way to solve this heat problem. The gate leakage constitutes the third bottleneck. With current 45 nm technology, the gate oxide thickness is 1.2 nm and the gate leakage current is approaching the off-current of the transistors. Therefore, further scaling-down of gate oxide thickness will result in the malfunction of the transistors.

Many devices and techniques have been proposed as possible future technologies that may supplant current complementary metal-oxide-semiconductor field-effect transistors (FETs) as the dominant device technology. These include spin devices [1, 2], carbon nanotube FETs [3-8], nanowire FETs [9-12], molecular electronic devices [13, 14] and single-electron transistor (SETs) [15, 16]. In the next section, the advantages and general features of SETs will be discussed.

1.2 GENERAL FEATURES OF SINGLE-ELECTRON TRANSISTORS

An SET consists of one small island connected to two electrodes (a “source” and a “drain”) through two tunnel barriers and capacitively coupled to a nearby third electrode (“gate” electrode) [15-17] as depicted in Fig 1.1. The resistance between the island and each of the electrodes must be larger than the quantum resistance. In this case, the number of electrons on the island is well defined. Therefore, the current flowing through the island can only occur by successive addition and removal of single electrons to and from the island. For example, a single electron would tunnel from the source to the island and subsequently from island to drain. The tunneling of electrons can be blocked at low bias voltage due to the Coulomb repulsive interaction until enough energy is provided by applying a voltage difference between the source and drain electrodes. This is known as the Coulomb blockade effect [15, 16, 18]. A gate voltage is applied to the gate electrode and tunes the electrostatic potential of the island. Controlling the gate voltage regulates the number of electrons tunneling on or off the island, one at a time. Due to the unique tunneling transport property, the electron energy is not dissipated and no heat would be produced. Another beneficial property of SETs is that the operation of SETs is extremely sensitive to external charge source that is coupled to the gate electrode. Thus, SETs can be utilized in extremely precise charge detection.

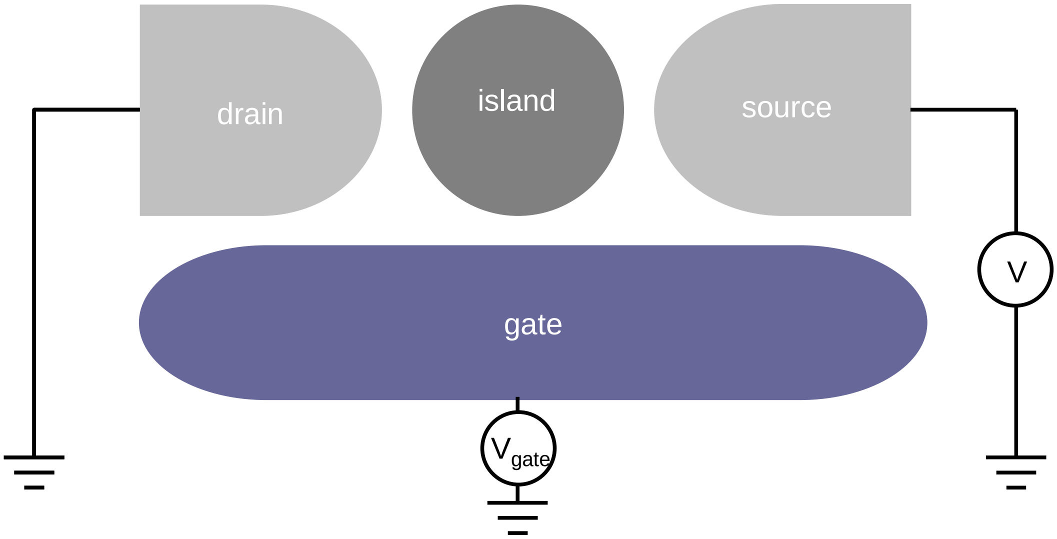

Figure 1.1: Schematic diagram of a single-electron transistor

In addition to the above advantages in application, SETs also show superior properties in fundamental studies. As the central island gets smaller, the energy spectrum of the island becomes discrete or quantized [19, 20]. The confined puddle of electron on the central island is analogous to the case of electron-in-a-box. The typical spacing between energy levels increases as the island size decreases. The energy level spacing reflects the quantum mechanical characteristics in the nanometer scale system. The spacing at the Fermi energy $\Delta E = \frac{1}{N(\varepsilon_F)} \sim \frac{1}{V}$, where $N(\varepsilon_F)$ is the density of states and V is the volume of the island. Other quantum excitations can also significantly modify the transport properties in SETs, such as vibrations of the central island [21-23]. These excitation energies can be extracted from the conductance measurements and studied in detail.

The spin degree of freedom can also be studied by the transport spectroscopy in SETs. For example, the g-factors of Al nanoparticles have been extracted from the transport spectroscopy; which was found to be smaller than that in bulk. This was attributed to the spin-orbital scattering from the surface or impurities [20]. The Kondo effect can also be observed when the island contains unpaired electron acting as local spin [24, 25]. The Kondo effect is originated from the entanglement between local spin and conduction electrons by the spin exchange interaction. Its characteristic temperature, the Kondo temperature, can be used to probe the strength of the exchange interaction between local spin and conduction electrons. Recent studies suggest that the Kondo temperatures from different system can vary from 7 K [26] to 60 K [27]. This variation suggests the difference of exchange interaction strength in different system and constitutes an interesting study topic.

Superconducting SETs is another interesting topic to be explored. In small superconducting island, parity effect has been observed in the transport spectroscopy. This effect results from whether the island contains an unpaired electron or not. By studying this effect, the energy difference between the ground states of the island with odd/even electrons can be obtained [28]. With smaller island, the level spacing ΔE could become larger than the superconducting gap of bulk material Δ. Then, superconductivity would no longer be possible, because Δ looses its special significance as gap in an continuous spectrum [29]. By studying the superconductivity of islands at different sizes, the size limit for the existence of superconductivity can be investigated.

1.3 PREVIOUS APPROACHES TO SINGLE-ELECTRON TRANSISTORS

With the above motivation, various fabrication methods of SETs have been developed in the past several decades. These methods can be classified into two different categories: top-down and bottom-up. The top-down method uses lithography technique to shape the island and source/drain electrodes. It includes the Si transistors [30, 31], the two-dimensional-electron gas SETs [24, 30, 32-38] and the SETs fabricated by angle evaporation of aluminum [28, 39-42]. Examples of the devices fabricated with these methods are shown in Fig 1.2 (a), (b) and (c). The detailed description of each method can be found in the references. With these methods, physics phenomena such as Coulomb blockade, quantized energy states and superconducting single-electron tunneling have been extensively investigated. However, with these methods, the island size is ~100 nm as determined by the resolution limit of current lithography. Therefore, it is difficult to achieve smaller island. Further, the materials of the electrodes and island are limited and SETs involving ferromagnetic materials has never been reported. The bottom-up approach seeks to form SETs by self-assembling an islands into the gaps between two electrodes. It includes the SETs incorporating the ensemble of small metallic islands [43, 44], the nanopore SETs [20, 45-49] and the SETs using the electron beam lithography and self-assembly of nanoparticle techniques [50, 51]. Fig 1.2 (d), (e) and (f) show the devices fabricated using the above methods. With these methods, SETs with various metallic nanoparticles have been implemented. However, the method of Fig 1.2 (d) can not prove the transport is through single particle. Both the methods of Fig 1.2 (e) and (f) involves elaborate fabrication process with less reproducibility.

In 1999, electromigration technique were developed by H. Park [52]. By precisely breaking a prefabricated nanowire, two electrodes with a nanometer-sized separation can be reproducibly achieved. This technique enables the study of nanometer scale structures with relatively less elaborate fabrication process and has attracted extensive attention. Most of the research presented in this thesis is based on electromigration method.

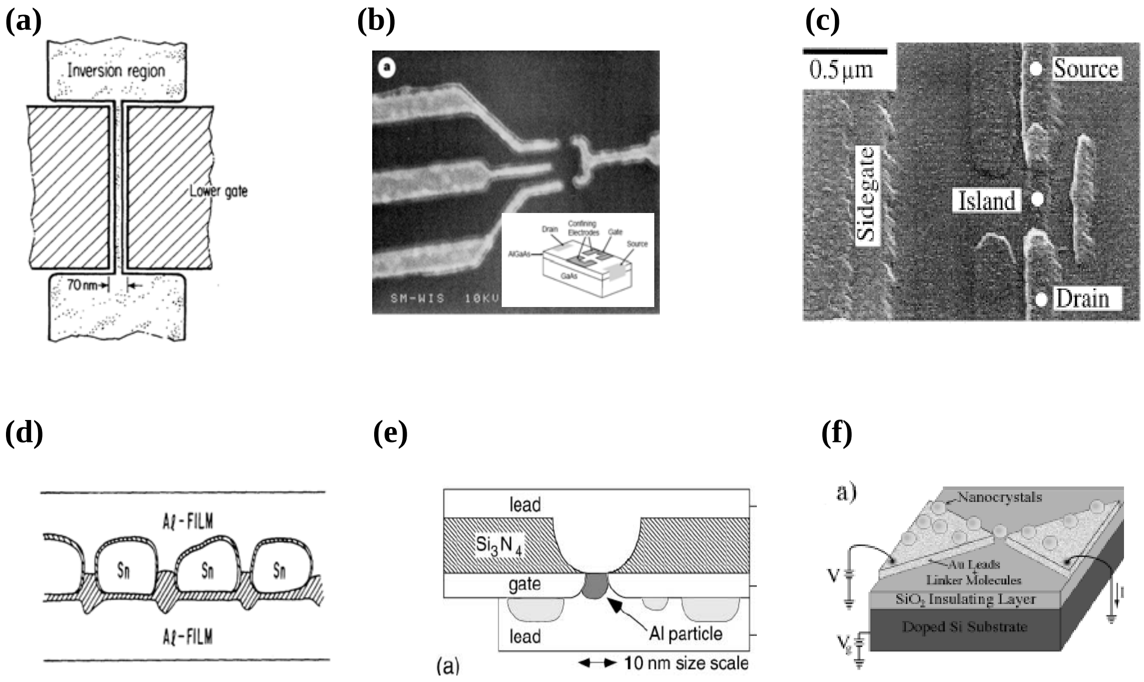

Figure 1.2: Previous approaches to SETs. (a) Si SETs (Adapted from ref. [31]). (b) 2DEG SETs (Adapted from ref. [24]). (c) SETs fabricated by angle evaporation technique (Adapted from ref. [42]). (d) SETs incorporating the ensemble of small metallic islands (Adapted from ref. [43]). (e) Nanopore SETs (Adapted from ref. [49]). (f) SETs fabricated by electron beam lithography and self-assembly of nanoparticles (Adapted from ref. [51]).

1.4 ORGANIZATION OF THIS THESIS

This thesis is organized mainly in chronological order of the experiments I have done in the past five years. This organization represents a logic train process for me, a novice in this field, to gain experience and knowledge; starting in shallow waters to being able to explore the deep sea and finally earning a Ph.D. In Chapter 2, I will introduce the concepts and theory that will be referred to in this thesis. It includes the theory of both classical Coulomb blockade and quantum Coulomb blockade. The single-electron tunneling effect in SSETs is briefly discussed at the end of this chapter. Chapter 3 presents three fabrication methods to realize SETs incorporating various gold nanoparticles. A novel method to achieve SETs with extremely small gold nanoparticle is described in Chapter 4. The excitation features are observed in the SETs and the origin of these excitations is studied in detail. Chapter 5 describes the fabrication of superconducting electrodes with nanometer separation. The tunneling characteristic is investigated and compared with conventional Bardeen-Cooper-Schrieffer theory of superconductivity. In Chapter 6, the investigation of the electronic transport properties of Pb SSETs is presented. The current features involving quasiparticle tunneling is discussed. In Chapter 7, the fabrication of single-molecule transistors (SMTs) by incorporating individual Co-Porphyrin molecules between superconducting electrodes is described. Preliminary electron transport study will be presented and discussed. Finally, I will summarize the work described in this thesis.

REFERENCES

[1] S. A. Wolf, D. D. Awschalom, R. A. Buhrman, J. M. Daughton, S. von Molnar, M. L. Roukes, A. Y. Chtchelkanova and D. M. Treger, Science **294**, 1488 (2001).

[2] I. Zutic, J. Fabian and S. Das Sarma, Rev. Mod. Phys. **76**, 323 (2004).

[3] S. J. Tans, A. R. M. Verschueren and C. Dekker, Nature **393**, 49 (1998).

[4] R. Martel, T. Schmidt, H. R. Shea, T. Hertel and P. Avouris, Appl. Phys. Lett. **73**, 2447 (1998).

[5] Z. Yao, C. Dekker and P. Avouris, Top. Appl. Phys. **80**, 147 (2001).

[6] A. Bachtold, P. Hadley, T. Nakanishi and C. Dekker, Science **294**, 1317 (2001).

[7] A. Javey, J. Guo, Q. Wang, M. Lundstrom and H. J. Dai, Nature **424**, 654 (2003).

[8] P. L. McEuen, M. S. Fuhrer and H. K. Park, IEEE Trans. Nanotechnol. **1**, 78 (2002).

[9] J. T. Hu, T. W. Odom and C. M. Lieber, Acc. Chem. Res. **32**, 435 (1999).

[10] X. F. Duan, Y. Huang, Y. Cui, J. F. Wang and C. M. Lieber, Nature **409**, 66 (2001).

[11] Y. Huang, X. F. Duan, Y. Cui, L. J. Lauhon, K. H. Kim and C. M. Lieber, Science **294**, 1313 (2001).

[12] Y. Cui, Z. H. Zhong, D. L. Wang, W. U. Wang and C. M. Lieber, Nano Lett. **3**, 149 (2003).

[13] A. Aviram and M. A. Ratner, Chem. Phys. Lett. **29**, 277 (1974).

[14] A. Nitzan and M. A. Ratner, Science **300**, 1384 (2003).

[15] H. D. Graber and M. H. Devoret, *Single Charge Tunneling* (Plenum, New York, 1992).

[16] K. K. Likharev, Proc. IEEE **87**, 606 (1999).

[17] L. P. Kouwenhoven, C. M. Marcus, P. L. McEuen, S. Tarucha, R. M. Westervelt and N. S. Wintergreen, in *Mesoscopic Electron Transport*, edited by L. P. Kouwenhoven, G. Schon and L. L. Shon (Kluwer Academic Publishers, Dordrecht, The Netherlands, 1996).

[18] L. P. Kouwenhoven, C. M. Marcus, P. L. McEuen, S. Tarucha, R. M. Westervelt and N. S. Wingreen, in *Mesoscopic Electron Transport*, edited by L. P. Kouwenhoven, G. Schon and L. L. Shon (Kluwer Academic Publishers, Dordrecht, The Netherlands, 1997).

[19] L. P. Kouwenhoven, D. G. Austing and S. Tarucha, Rep. Prog. Phys. **64**, 701 (2001).

[20] J. von Delft and D. C. Ralph, Phys. Rep. **345**, 61 (2001).

[21] H. Park, J. Park, A. K. L. Lim, E. H. Anderson, A. P. Alivisatos and P. L. McEuen, Nature **407**, 57 (2000).

[22] L. H. Yu, Z. K. Keane, J. W. Ciszek, L. Cheng, M. P. Stewart, J. M. Tour and D. Natelson, Phys. Rev. Lett. **93**, 266802 (2004).

[23] D. H. Chae, J. F. Berry, S. Jung, F. A. Cotton, C. A. Murillo and Z. Yao, Nano Lett. **6**, 165 (2006).

[24] D. Goldhaber-Gordon, H. Shtrikman, D. Mahalu, D. Abusch-Magder, U. Meirav and M. A. Kastner, Nature **391**, 156 (1998).

[25] L. Kouwenhoven and L. Glazman, Physics World **14**, 33 (2001).

[26] A. A. Houck, J. Labaziewicz, E. K. Chan, J. A. Folk and I. L. Chuang, Nano Lett. **5**, 1685 (2005).

[27] H. B. Heersche, Z. de Groot, J. A. Folk, L. P. Kouwenhoven, H. S. J. van der Zant, A. A. Houck, J. Labaziewicz and I. L. Chuang, Phys. Rev. Lett. **96**, 017205 (2006).

[28] M. Tinkham, *Introduction to Superconductivity* (McGraw-Hill, New York, 1996).

[29] P. W. Anderson, J. Phys. Chem. Solids **11**, 26 (1959).

[30] J. H. F. Scottthomas, S. B. Field, M. A. Kastner, H. I. Smith and D. A. Antoniadis, Phys. Rev. Lett. **62**, 583 (1989).

[31] S. B. Field, M. A. Kastner, U. Meirav, J. H. F. Scottthomas, D. A. Antoniadis, H. I. Smith and S. J. Wind, Phys. Rev. B **42**, 3523 (1990).

[32] L. I. Glazman and R. I. Shekhter, J. Phys.: Condens. Matter **1**, 5811 (1989).

[33] U. Meirav, M. A. Kastner and S. J. Wind, Phys. Rev. Lett. **65**, 771 (1990).

[34] P. L. McEuen, E. B. Foxman, U. Meirav, M. A. Kastner, Y. Meir, N. S. Wingreen and S. J. Wind, Phys. Rev. Lett. **66**, 1926 (1991).

[35] T. H. Oosterkamp, L. P. Kouwenhoven, A. E. A. Koolen, N. C. vanderVaart and C. Harmans, Phys. Rev. Lett. **78**, 1536 (1997).

[36] L. P. Kouwenhoven, T. H. Oosterkamp, M. W. S. Danoesastro, M. Eto, D. G. Austing, T. Honda and S. Tarucha, Science **278**, 1788 (1997).

[37] T. H. Oosterkamp, J. W. Janssen, L. P. Kouwenhoven, D. G. Austing, T. Honda and S. Tarucha, Phys. Rev. Lett. **82**, 2931 (1999).

[38] S. Tarucha, D. G. Austing, T. Honda, R. J. vanderHage and L. P. Kouwenhoven, Phys. Rev. Lett. **77**, 3613 (1996).

[39] T. A. Fulton and G. J. Dolan, Phys. Rev. Lett. **59**, 109 (1987).

[40] T. M. Eiles, J. M. Martinis and M. H. Devoret, Phys. Rev. Lett. **70**, 1862 (1993).

[41] P. Lafarge, P. Joyez, D. Esteve, C. Urbina and M. H. Devoret, Phys. Rev. Lett. **70**, 994 (1993).

[42] J. Weis, Y. Y. Wei and K. von Klitzing, Physica E **3**, 23 (1998).

[43] I. Giaever and H. R. Zeller, Phys. Rev. Lett. **20**, 1504 (1968).

[44] H. R. Zeller and I. Giaever, Phys. Rev. **181**, 789 (1969).

[45] D. C. Ralph, C. T. Black and M. Tinkham, Phys. Rev. Lett. **74**, 3241 (1995).

[46] C. T. Black, Ph. D. Thesis, Harvard University, (1996).

[47] C. T. Black, D. C. Ralph and M. Tinkham, Phys. Rev. Lett. **76**, 688 (1996).

[48] D. C. Ralph, C. T. Black, J. M. Hergenrother, J. G. Lu and M. Tinkham, in *Mesoscopic Electron Transport*, edited by L. P. Kouwenhoven, G. Schon and L. L. Shon (Kluwer Academic Publishers, Dordrecht, The Netherlands, 1997).

[49] D. C. Ralph, C. T. Black and M. Tinkham, Phys. Rev. Lett. **78**, 4087 (1997).

[50] D. L. Klein, P. L. McEuen, J. E. B. Katari, R. Roth and A. P. Alivisatos, Appl. Phys. Lett. **68**, 2574 (1996).

[51] D. L. Klein, R. Roth, A. K. L. Lim, A. P. Alivisatos and P. L. McEuen, Nature **389**, 699 (1997).

[52] H. Park, A. K. L. Lim, A. P. Alivisatos, J. Park and P. L. McEuen, Appl. Phys. Lett. **75**, 301 (1999).

Chapter 2: Single-Electron Tunneling Effect

2.1 INTRODUCTION

In the previous chapter, we have discussed the general features in SETs. In this chapter, we review the basic theory of electronic transport through SETs with these features. In the theory, several energy scales play important roles. The first energy scale is the Coulomb charging energy, which is the electrostatic energy cost of adding an individual charge to a small island. This energy cost leads to the single-electron tunneling behavior referred to as the Coulomb blockade. The second energy scale is the quantum excitation energy. The most commonly observed excitation energy is due to quantum confinement. For SETs in which quantum levels of nanoparticles are too closely spaced and can be regarded continuous, the Coulomb blockade is classical Coulomb blockade. If the spacing is resolvable discrete in our measurement energy scale, the Coulomb blockade is quantum Coulomb blockade [1, 2]. We can distinguish the two regimes:

(1) $\Delta E << k_B T << E_C$, the classical Coulomb blockade regime.

(2) $k_B T << \Delta E \le E_C$, the quantum Coulomb blockade regime.

where $k_B T$ is the thermal energy, ΔE is the quantum energy level spacing and E_C is the Coulomb charging energy. In order to observe the single-electron tunneling effect, the Coulomb charging energy must be much larger than the thermal energy $E_C > k_B T$. Otherwise, the thermal fluctuation effect will be dominant and the single-electron tunneling effect will be smeared out. Also, the number of electrons on the island must be well defined, which requires that the resistance between the island and each of the electrodes must be larger than the quantum resistance $R > R_0 = \frac{h}{e^2} = 25.81\,\mathrm{k\Omega}$. The theory of the classical Coulomb blockade and quantum blockade are discussed in this Chapter and will be referred to in Chapter 3 and 4 respectively.

The SETs' island and electrodes can be made of superconducting materials, such as Al and Pb. The superconducting gap energy scale must be considered. The tunneling between superconducting electrodes is different from that through normal metallic junction and the Coulomb blockade effect in superconducting single-electron transistors (SSETs) will be modified by the superconductivity [3]. At the end of this Chapter, the tunneling between superconducting electrodes and the Coulomb blockade effect in SSETs are briefly discussed since they will be referred later in this thesis.

2.2 CLASSICAL COULOMB BLOCKADE

The classical Coulomb blockade regime can be described by the so-called "orthodox" Coulomb blockade theory [4]. An SET shown in Fig. 1.1 can be modeled by the equivalent circuit in Fig. 2.1. In the schematic, the two tunneling barriers are represented by tunneling resistances (R_s and R_d) and capacitances (C_s and C_d), where *s* and *d* designate source and drain electrodes respectively. A gate electrode couples to the island through gate capacitance C_g. The charge of the island is the sum of that induced by each of the electrodes:

$$Q = -Ne = (V_{is} - V)C_s + V_{is}C_d + (V_{is} - V_g)C_g + Q_0 \tag{2.1}$$

Here, N is the number of excess electrons on the island, Q_0 is the offset charge induced by the local environment and V_{is} is the potential of the island. Thus the total energy of the island is given by:

$$U(N) = \frac{1}{2}C_{tot}V_{is}^2 = \frac{(-Ne - Q_0 + VC_s + V_gC_g)^2}{2C_{tot}} \tag{2.2}$$

where $C_{tot} = C_s + C_d + C_g$ is the total capacitance of the island in the SET.

Let us now consider the transport process where the *N*th electron is added to the island from the drain. The energy required to add the *N*th electron to the island with *N*-1 electrons is:

$$\mu_N = U(N) - U(N-1) = \frac{e}{C_{tot}}\left(\left(N - \frac{1}{2}\right)e + Q_0 - VC_s - V_{gate}C_g\right) \qquad (2.3)$$

If the *N*th electron is added/removed to the island from the source, the energy required is:

$$\mu_N = U(N) - U(N-1) + eV = \frac{e}{C_{tot}}\left(\left(N - \frac{1}{2}\right) + Q_0 + VC_{tot} - VC_s - V_{gate}C_g\right) \qquad (2.4)$$

We call μ_N the electrochemical potential of the island for the *N*th electron.

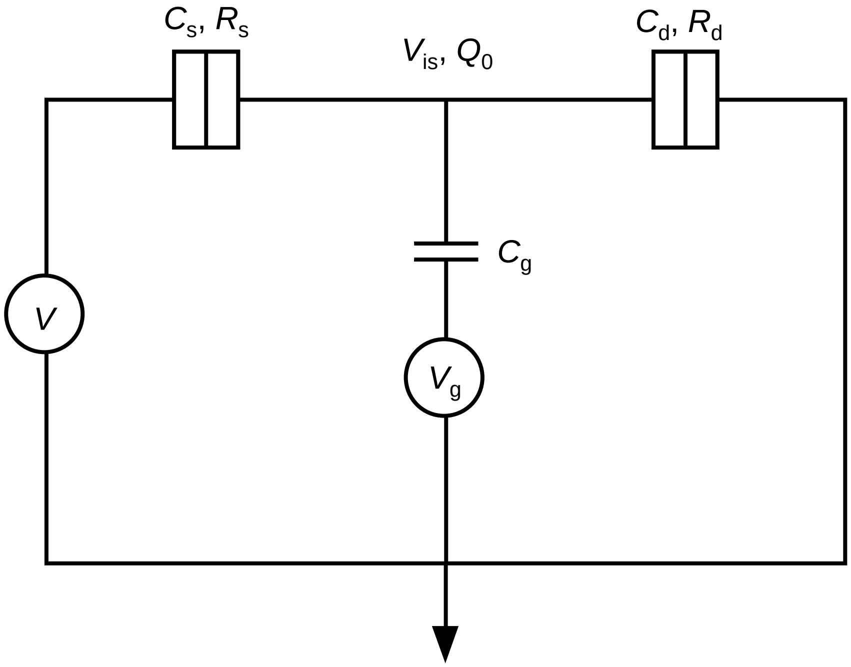

Figure 2.1: Equivalent circuit of an SET.

Below, the electron transport process between the island and the drain is described; the analysis of transport between the island and the source is similar.

At a certain V_g with zero V, μ_N is always no less than zero to keep the system stable with N-1 electrons. As V increases from zero to certain value, μ_N decreases from a positive to a negative value. In Fig 2.2, the energy diagrams and current features [5] with different values of μ_N are depicted. When μ_N is positive, the system is energetically stable with N-1 electrons, the transport of the Nth electron is energetically prohibited, therefore the current is suppressed as indicated in Fig 2.2 (a) by arrow (a) [the energy diagram is depicted in Fig 2.2 (b)]. This is called the Coulomb blockade regime. In the blockade regime, the bias voltage V cannot provide enough energy to overcome the Coulomb charging energy required to add the Nth electron to the island. The current is suppressed. As V increase to a voltage V_t (threshold voltage of the Coulomb blockade) shown by arrow (b) in Fig 2.2 (a), μ_N reaches zero, the systems with N and N-1 electrons are energetically degenerate. The energy supplied by the bias voltage equals the Coulomb charging energy and the Nth electron can be added to the island. The fluctuation of charges between N and N-1 electrons in the island leads to the transport current. The corresponding energy diagram is shown in Fig 2.2 (d). As V increases more, μ_N becomes negative, the current increases further as the region shown by arrow (c). Fig 2.2 (c) shows the energy diagram in this case.

As gate voltage V_g is tuned, the voltage of the island is changed. Therefore the electrochemical potential of the dot is changed and the threshold voltage of the Coulomb blockade V_t is modulated as well. The change of V_t leads to different current-voltage (I-V) characteristics. I-V characteristics at various V_g are shown in Fig 2.3 (a). In the plot, V_t varies from a maximum value to zero. The maximum V_t gives the measurement of the

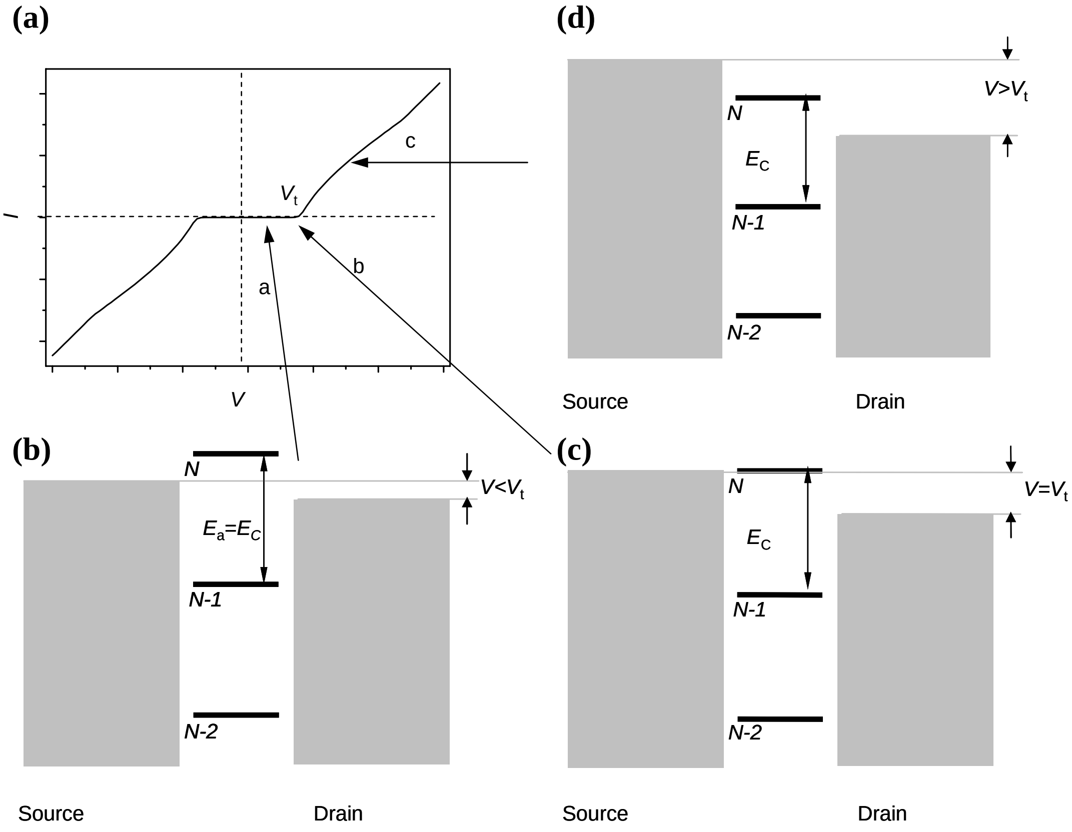

Figure 2.2: Classical Coulomb blockade effect. (a) Characteristic current-voltage curve. Schematic energy diagram when voltage is (b) smaller than, (c) equal to, and (d) larger than Coulomb blockade threshold voltage.

Coulomb charging energy E_C. The value of the Coulomb charging energy is determined by total capacitance of the island as $E_C = \frac{e^2}{C_{tot}}$. Fig 2.3 (b) plots the differential conductance of SETs as a function of bias voltage V and gate voltage V_g. At low bias voltage, the conductance is suppressed and the suppression regime is indicated by dark diamonds which are called the Coulomb diamonds. At higher bias voltage, the transport is allowed and the diamond of light color represents the high conductance regime. The value of the Coulomb charging energy E_C can be extracted from the plot and it is the bias voltage where the boundaries of the Coulomb blockade regimes intersect as shown in Fig 2.3 (b). At the boundaries of the Coulomb diamonds, the electrochemical potential of the island for *N*th electron $\mu_N = 0$, transport starts. The slopes of the Coulomb diamonds are the relationship between V_{gate} and V by solving $\mu_N = 0$. At certain gate voltages, $\mu_N = 0$ at zero bias voltage, these points are called degeneracy points. If we plot the conductance as a function of gate voltage at a fixed bias, conductance peaks are observed at the degeneracy points and conductance valleys are observed between the degeneracy points. The periodicity of the conductance peaks is $\frac{e}{C_g}$. This phenomenon is plotted in Fig 2.3 (d). Around the degeneracy points, the line shape of the conductance peaks is [1, 2]:

$$G = G_\infty \frac{\delta / k_B T}{2 \sinh(\delta / k_B T)} \quad \text{for} \quad E_C >> k_B T \tag{2.5}$$

where $\delta = e(C_g / C_{tot}) \cdot |V_g - V_g^*|$, V_g^* is the gate voltage where the degeneracy point is. This formula gives the temperature dependence of the conductance peak. The plot in Fig 2.3 (c) shows that as temperature increases, the peak width increases whereas the peak height keeps constant.

2.3 QUANTUM COULOMB BLOCKADE

The above description does not include any quantum behavior except the charge quantization on the island. The energy levels are assumed to be continuous. However, this assumption may not remain valid as the size of the nanoparticles shrinks to less than

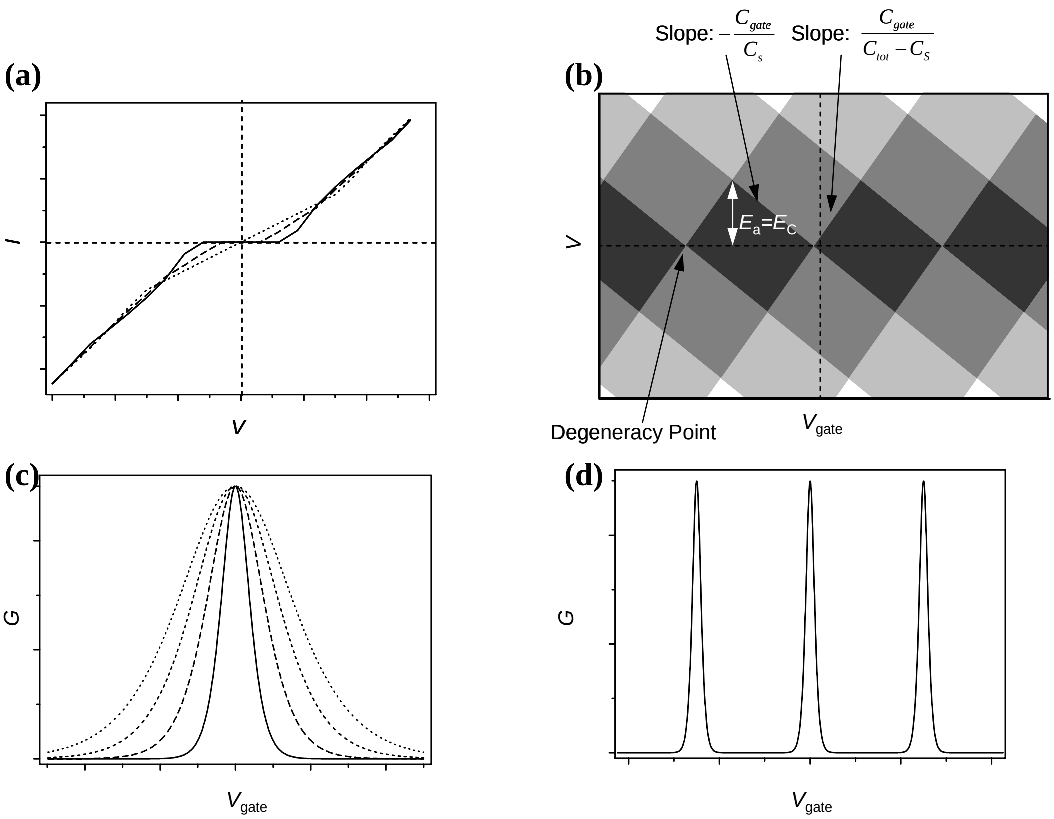

Figure 2.3: Coulomb blockade effect and Coulomb oscillations. (a) Characteristic *I*-*V* curves at gate voltages of ne/C_{tot} (solid line), $(n+1/2)e/C_{tot}$ (dotted line) and between (dashed line). (b) Two-dimensional plot of differential conductance as a function of bias and gate voltage. Bright (dark) color corresponds to high (low) conductance. The slopes are determined by ratios of the capacitances. (c) The effect of temperature on the Coulomb oscillation peak. (d) Conductance oscillation versus gate voltage at a small bias voltage.

a few nanometers. In this case, the quantum energy level spacing must be considered and the Coulomb blockade is quantum Coulomb blockade. Fig 2.4 (a) plots the estimations of the Coulomb charging energy and the energy level spacing due to quantum confinement in gold nanoparticles [2, 6]. The estimation shows that as the size reduces to ~0.5 nm, the quantum energy level spacing becomes comparable with the Coulomb charging energy.

Therefore, the energy levels cannot be regarded as continuous any more. A schematic energy diagram of a nanoparticle is shown in Fig 2.4 (c). The size of the nanoparticle is so small that the quantum energy level spacing cannot be negligible. The solid line represents the ground state of each charge state and the dashed lines correspond to the quantum excited states. By taking into account these excitations, we can rewrite the electrochemical potential of the island for the *N*th electron as:

$$\mu_N = U(N) - U(N-1) = \frac{e}{C_{tot}}\left(\left(N - \frac{1}{2}\right) + Q_0 - VC_s - V_g C_g\right) + \sum_{i=1}^{N} \Delta E_i^N - \sum_{i=1}^{N-1} \Delta E_i^{N-1} \quad (2.6)$$

where ΔE_i^N and ΔE_i^{N-1} are the excitation energies of the *N* and *N*-1 electron configurations. If the energy levels of the *N* electron configuration are similar to those of the *N*-1 configuration, we can rewrite the equation as:

$$\mu_N = U(N) - U(N-1) = \frac{e}{C_{tot}}\left(\left(N - \frac{1}{2}\right) + Q_0 - VC_s - V_{gate} C_g\right) + \Delta E_N \quad (2.7)$$

In equation (2.7), an extra energy ΔE_N is required to add the *N*th electron to the island. In the *I*-*V* curve, the threshold voltage of the Coulomb blockade is offset to higher bias by ΔE_N and additional features can be observed due to the presence of excitation states. Fig 2.4 (b) shows a representative *I*-*V* curve of an SET in the quantum Coulomb blockade

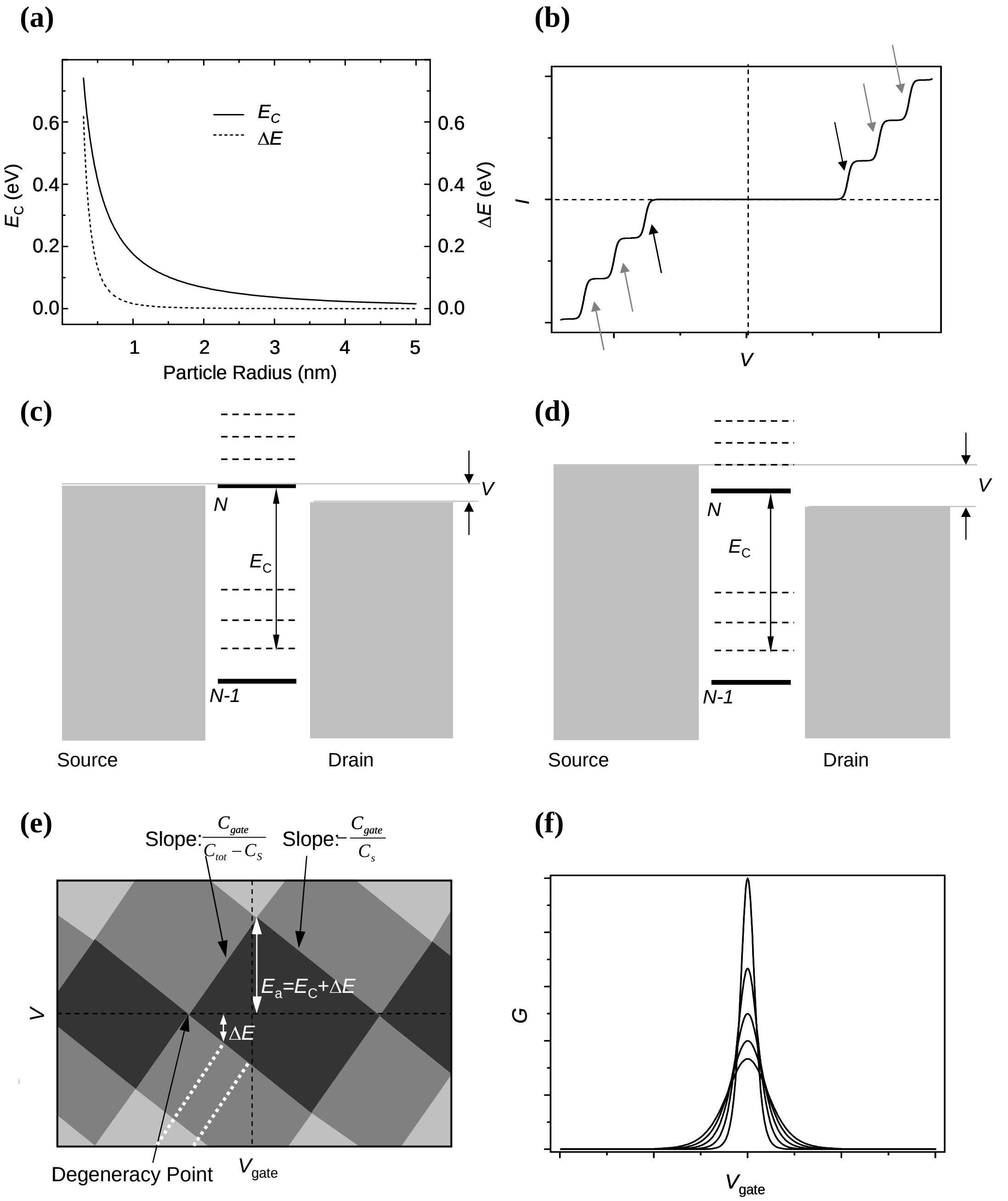

Figure 2.4: Quantum Coulomb blockade effect. (a) Charging energy (solid line) and quantum confinement energy level spacing (dotted line) as a function of the radius of a gold nanoparticle. (b) Characteristic *I*-*V* curve with excitation steps. Schematic energy diagram at the bias voltages indicated in (b) by black (c) and grey (d) arrows. (e) Conductance vs. bias and gate voltages. (f) Temperature effect of the Coulomb oscillation peak in the quantum regime.

regime. In the plot of Fig 2.4 (b), the dark arrow indicates the threshold voltage of the Coulomb blockade. At this voltage, the applied bias aligns the Fermi energy level of the source electrode with the ground state of the island with *N* electrons as shown in Fig 2.4 (c). The *N*th electron can be added to the island and transport starts. As bias voltage increases further, the excited state enters the energy window opened by the bias voltage as indicated in Fig 2.4 (d). The excited state contributes an extra transport channel, which results in a stepwise current increase as indicated in Fig 2.4 (b) by the gray arrows. These step increases result in conductance peaks. In Fig 2.4 (e), the conductance is plotted as a function of bias voltage and gate voltage. The peaks appear as the dotted lines parallel to the Coulomb blockade boundary. The measurement of the excitation energies are indicated by the intersections of the dotted lines and Coulomb blockade boundaries. The additional energy E_a should be the sum of the Coulomb charging energy E_C and the excitation energy ΔE_N as illustrated in Fig 2.4 (e).

At the degeneracy points in Fig 2.4 (e), the conductance peaks are observed at zero bias. The line shape of the conductance peaks is [1, 2]:

$$G = G_\infty \frac{\Delta E}{4k_B T} \cosh^{-2}\left(\frac{\delta}{2k_B T}\right) \tag{2.8}$$

It shows different temperature dependence from the classical Coulomb blockade. In Fig 2.4 (f), the conductance as a function of gate voltage at fixed small bias voltage is plotted at various temperatures. The peak width increases as temperature increases and the peak height decreases.

Based on the above description, we can utilize the electron transport measurement as a spectroscopic tool to understand electronic structures of a small island in the Coulomb blockade regime.

2.4 SUPERCONDUCTING SINGLE-ELECTRON TUNNELING EFFECT

In the above theory, the SETs consist of the island and electrodes made of normal metals. When superconducting materials are used in the SETs, the Coulomb blockade effect will be modified. In this section, the tunneling theory between superconducting electrodes will be briefly described first and then the superconducting single-electron tunneling effect will be presented.

Electron tunneling through a junction with two electrodes has been widely used to examine the properties of the electrodes. If the two electrodes are normal metal, the tunneling current is proportional to the density of states (DOS) of the two electrodes $I \propto N_L(0)N_R(0)eV$, where V is the applied bias voltage, $N_L(0)/N_R(0)$ is the DOS of

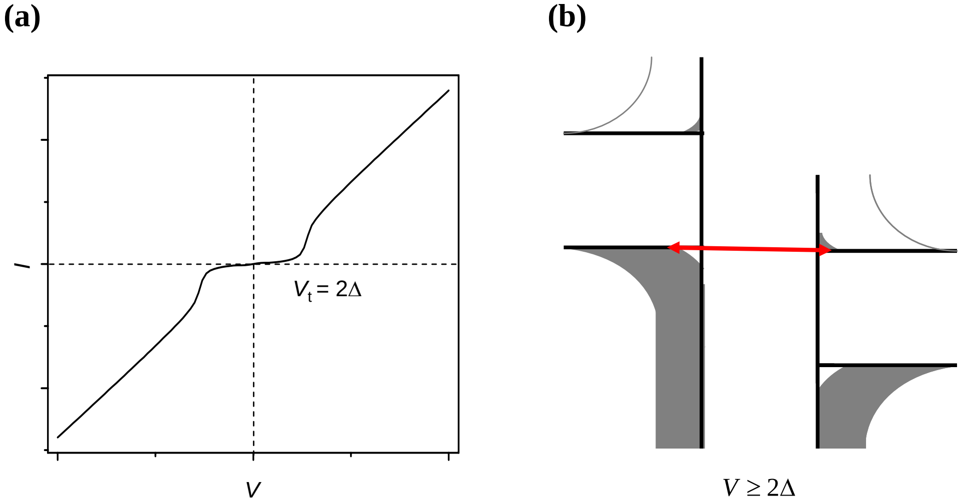

Figure 2.5: Superconductor-superconductor (SS) tunneling junction. (a) tunneling *I*-*V* characteristic through an SS junction. (b) Schematic energy diagram of an SS junction at the bias voltage $V \geq 2\Delta$. The red line corresponds to the tunneling of quasiparticles created by the applied bias voltage.

The left/right electrode. When the electrodes are made of superconductor, the quasiparticle tunneling characteristic can be described [3]:

$$\begin{aligned} I_{SS} &= \frac{G_{nn}}{e}\int_{-\infty}^{\infty}\frac{N_{RS}(E)N_{LS}(E+eV)}{N_R(0)N_L(0)}\left[f(E)-f(E+eV)\right]dE \\ &= \frac{G_{nn}}{e}\int_{-\infty}^{\infty}\frac{|E|}{\left[E^2-\Delta_R^2\right]^{1/2}}\frac{|E+eV|}{\left[(E+eV)^2-\Delta_L^2\right]^{1/2}}\left[f(E)-f(E+eV)\right]dE \end{aligned} \tag{2.9}$$

where G_{nn} is the differential conductance of the junction when the electrodes are in normal state, $f(E)$ is Fermi distribution function at energy E and Δ_L / Δ_R is the superconducting gap of the left/right electrode. In this thesis, the two electrodes are of the same material and $\Delta_L = \Delta_R \equiv \Delta$. At $T = 0$, no current can flow until $eV = 2\Delta$ as indicated by Fig 2.5 (a) due to the absence of available states in the superconducting gap. At $eV \geq 2\Delta$, the potential difference between the two electrodes supplies enough energy to create quasiparticles on both the left and the right electrode and the tunneling of quasiparticles starts as illustrated in Fig 2.5 (b). In the suppression regime, the tunneling of normal quasiparticles created by bias voltage is not allow, high order tunneling such as multiple Andreev reflection (MAR) [7-9] can contribute fine current features. The feature's magnitude is inversely proportional to the junction resistance. This thesis focuses on the tunneling spectroscopy through junctions with high resistance and MAR has not been studied.

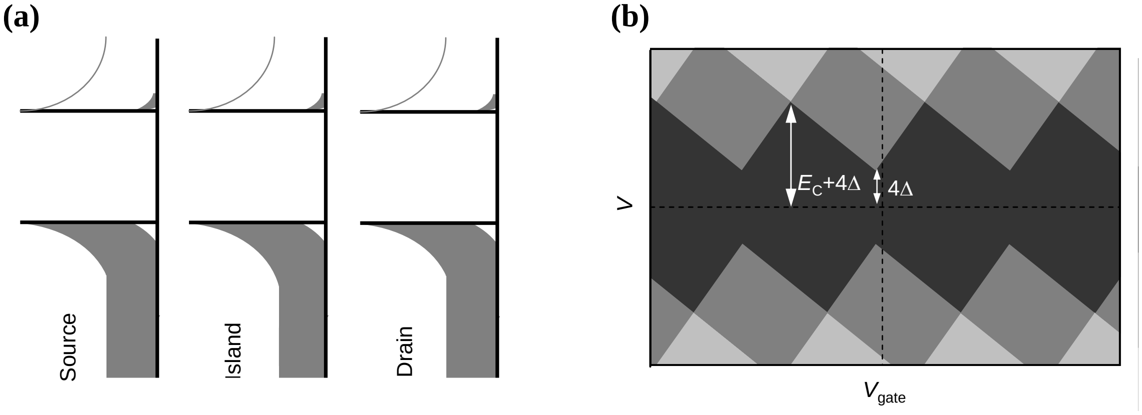

Figure 2.6: Superconducting single-electron tunneling effect. (a) A schematic energy diagram of an SSET at zero bias voltage and gate voltage. (b) Differential conductance of an SSET as a function of bias voltage and gate voltage due to the sequential tunneling of the normal quasiparticles through an SSET.

An SSET can be implemented by placing superconducting nanoparticles between two superconducting electrodes. The energy diagram of an SSET is plotted in Fig 2.6 (a). At $T = 0\,\mathrm{K}$, to add one quasiparticle to the island from the source electrode, the energy required is:

$$\mu_N = U(N) - U(N-1) = \frac{e}{C_{tot}}\left(\left(N - \frac{1}{2}\right) - VC_s - V_{gate}C_g\right) + 2\Delta \qquad (2.10)$$

where 2Δ results from the energy required to create quasiparticles on both the source electrode and the island. This equation gives the threshold of the Coulomb blockade in SSETs. To produce net current, another quasiparticle must tunnel out of the island to the drain electrode. An extra 2Δ energy will be required to create quasiparticles on both the island and the drain electrode. Consequently, 4Δ extra energy is necessary to realize the tunneling processes of the quasiparticles through both tunneling junctions. The quasiparticle tunneling conductance is plotted in Fig 2.6 (b) as a function of bias voltage and gate voltage. The boundaries of conductance suppression regime are the thresholds of the sequential tunneling of normal quasiparticles created by bias voltage and at these boundaries, $\mu_N = 0$. The plot clearly shows that the thresholds of the quasiparticle tunneling are offset to high bias by 4Δ compared with the classical Coulomb blockade in normal SETs.

In the transport study of SSETs, a broad family of fine features may be observed in the suppression regime. These features originate from various tunneling processes, such as the Josephson quasiparticle tunneling [10] and the quasiparticle tunneling involving singularity matching [11]. More detailed discussions of the fine features due to various tunneling processes can be found in several review articles and textbooks [3, 12, 13].

REFERENCES

[1] H. D. Graber and M. H. Devoret, *Single Charge Tunneling* (Plenum, New York, 1992).

[2] L. P. Kouwenhoven, C. M. Marcus, P. L. McEuen, S. Tarucha, R. M. Westervelt and N. S. Wintergreen, in *Mesoscopic Electron Transport*, edited by L. P. Kouwenhoven, G. Schon and L. L. Shon (Kluwer Academic Publishers, Dordrecht, The Netherlands, 1997).

[3] M. Tinkham, *Introduction to Superconductivity* (McGraw-Hill, New York, 1996).

[4] I. O. Kulik and R. I. Shekhter, Zhurnal Eksperimentalnoi I Teoreticheskoi Fiziki **68**, 623 (1975).

[5] The simulation program is available at http://qt.tn.tudelft.nl/CHARGE.

[6] C. Kittel, *Introduction to Solid State Physics* (Wiley, New York, 2004).

[7] A. F. Andreev, Sov. Phys. JETP **19**, 1228 (1964).

[8] A. W. Kleinsasser, R. E. Miller, W. H. Mallison and G. B. Arnold, Phys. Rev. Lett. **72**, 1738 (1994).

[9] E. Scheer, P. Joyez, D. Esteve, C. Urbina and M. H. Devoret, Phys. Rev. Lett. **78**, 3535 (1997).

[10] T. A. Fulton, P. L. Gammel, D. J. Bishop, L. N. Dunkleberger and G. J. Dolan, Phys. Rev. Lett. **63**, 1307 (1989).

[11] Y. Nakamura, A. N. Korotkov, C. D. Chen and J. S. Tsai, Phys. Rev. B **56**, 5116 (1997).

[12] D. C. Ralph, C. T. Black, J. M. Hergenrother, J. G. Lu and M. Tinkham, in *Mesoscopic Electron Transport*, edited by L. P. Kouwenhoven, G. Schon and L. L. Shon (Kluwer Academic Publishers, Dordrecht, The Netherlands, 1997).

[13] J. von Delft and D. C. Ralph, Phys. Rep. **345**, 61 (2001).

Chapter 3: Fabrication of Gold Single-Electron Transistors

3.1 INTRODUCTION

In the past two decades, single-electron transistors (SETs) made from normal metallic nanoparticles have attracted extensive research interests for their application potentials [1-6] as future generation of integrate circuit unit and ultra sensitive electrometers. For these applications, it is desirable to minimize the size of the central island of the transistors, so as to increase the charging energy, optimize the charge sensitivity of electrometers and raise the operation temperature. The metallic SETs also constitute model systems to probe the individual "electron-in-box" quantum states within the nanoparticles if the size of the central island is smaller than a few nanometers [7]. With metallic SETs, a variety of fundamental charge transport studies have been carried out in the past several years [8-10]. Several techniques have been developed to realize the fabrication of metallic SETs, such as high resolution electron-beam lithography [11, 12], nanopore technique [7, 13-17]. However, wide applications and systematical fundamental investigations of nanoparticle SETs are still limited by several technical obstacles including (1) the complexity of the process to fabricate electrodes with nanometer-sized separation, (2) precise placement of the nanoparticles between the electrodes, (3) the challenge to have the nanoparticles efficiently coupling with gate electrode to enable the accessibility to enough number of charge states [17, 18].

In this chapter, three methods to fabricate SETs incorporating various gold nanoparticles are presented. The yield of SET devices is discussed and the electron transport measurement results are analyzed with classical Coulomb blockade theory presented in the previous chapter.

3.2 ELECTROSTATIC TRAPPING OF GOLD NANOPARTICLES

This fabrication contains three steps [18]. In the first step, gold nanobridge is formed by assembling gold nanoparticles between the electrodes with hundreds nanometer separation by AC electric field. Then, DC voltage is ramped up across the nanobridge; the bridge is broken due to current induced electromigration. This process consistently produces stable electrodes with sub-10 nanometer spacing. Finally, colloid gold nanoparticles are self-assembled between electrodes to realize nanoparticle SETs.

The starting electrodes are first patterned on top of Si/SiO_2 wafer using standard lithography. Thermal evaporation of Cr/Au (5nm/30nm) followed by lift-off process are used to define the electrodes. The initial separation between the electrodes varies from 40 nm to 200 nm. The electrodes are cleaned by oxygen plasma for 30 minutes and rinsed in ethanol. The gold nanoparticles with sizes of 5, 10, 20 and 50 nanometer are suspended in water and dropped on top of electrodes. A schematic of our experimental setup is shown in Fig 3.1 (a). An AC voltage is applied between the electrodes using a function generator. Due to the presence of an electric field gradient, the nanoparticles are attracted to the gap where they experience the largest dielectrophoretic force. An output signal can be observed by an oscilloscope as soon as the electrodes are bridged by conducting gold nanoparticles. After this process, the sample is blown dry immediately with N_2 gas. The AC voltage is around 1 ~ 3 V at the frequency of 1 MHz. When the initial gap size is around 100 nm, the bridging process takes around 10 seconds to complete. The size of the particles is 50 nm and the concentration is $3\times10^{10}\ \text{Particles/ml}$ for this bridging condition. Fig 3.1 (b) shows a high resolution scanning electron microscopy (HRSEM) image of a device with nanobridge formed by gold nanoparticles between two electrodes with 400 nm initial separation.

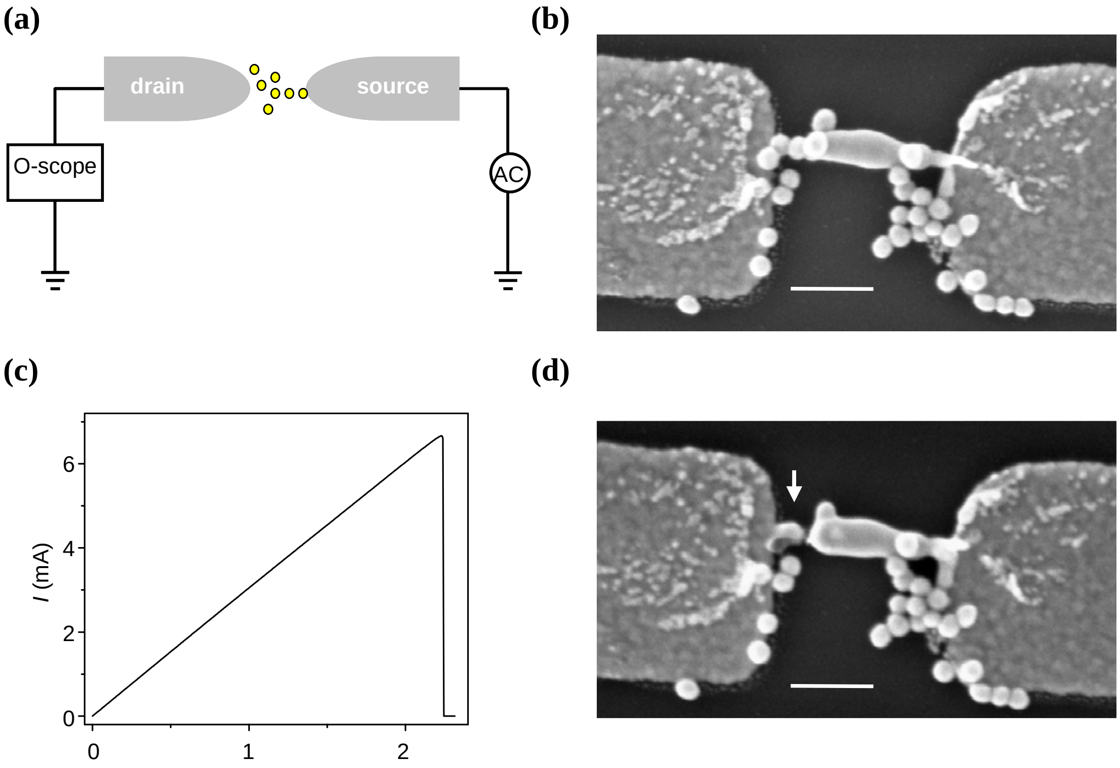

Figure 3.1: Electrostatic trapping method to fabricate gold nanoparticle SETs in combination with electromigration technique. (a) A schematic diagram of electrostatic trapping experimental setup. (b) HRSEM image of a pair of electrodes with 400 nm gap bridged by a chain of 50 nm gold particles. (c) Current trace of a gold nanoparticle bridge during electromigration process. (d) HRSEM image of the gold nanoparticle bridge after breaking. The gap is indicated by an arrow. The scale bars in the images correspond to 200 nm. (b), (c) and (d) are adapted from ref. [18].

In the second step, a DC voltage is ramped up across the nanobridge, and the current through the bridge is monitored. When the voltage reaches certain value that is always less than 3 V, the current shows an abrupt decrease to almost zero, which indicates the breaking of the nanobridge due to the current-induced electromigration. A typical current versus applied voltage is plotted in Fig 3.1 (c), and a HRSEM image of the nanobridge after electromigration is shown in Fig 3.1 (d) where a sub-10 nm gap is indicated by an arrow.

The electrodes with sub-10 nm separation are immediately put into water solution containing gold nanoparticles passivated by dithiothreitol ($C_4H_{10}O_2S_2$) molecules. An AC voltage is applied to trap the nanoparticles between the electrodes for ~1 min. The dithiothreitol molecules prevent the formation of conduction nanobridge and act as the tunneling barriers between the nanoparticle and electrodes. With the Si back gate electrode, gold nanoparticle SETs are realized.

The gold nanoparticle SETs are measured immediately after fabrication at liquid helium temperature. The current as a function of bias voltage and gate voltage is measured. By numerically differentiating the current with respect to the bias voltage, the conductance can be obtained. Fig 3.2 shows a two-dimensional plot of differential conductance (dI/dV) as a function of bias and gate voltages. Around zero bias the conductance is suppressed and the size of the voltage gaps can be modulated with the application of a gate voltage. Five diamond-shaped regions can be identified in which the conductance is suppressed.

These features are characteristic of the classical Coulomb blockade. Each diamond-shaped region corresponds to a charge state of the nanoparticle. The slopes of the boundaries of blockaded regions are determined by the capacitances of the nanoparticle with respect to the source, drain and gate electrodes. The observation of constant slopes for the five diamonds in Fig. 3.2 indicates that a single nanoparticle is bridging the gap. The bias voltage at which the boundaries of Coulomb diamonds intersect is a measure of the Coulomb charing energy, which is E_C ~ 12 meV. The total capacitance can be estimated $C_{tot} = e/E_C = 14\,\mathrm{aF}$. The source/drain capacitance is around 7 aF, and gate capacitance is around 0.45 aF. A simple model of a metal sphere island between two parallel plate electrodes is adopted to estimate the sized of the nanoparticle. In this model, the relationship between the Coulomb charging energy and the radius of the sphere island is $E_C = \frac{0.7}{\varepsilon r}\left(1+\frac{r}{2d}\right)^{-1} \mathrm{eV}\cdot\mathrm{nm}$, where r is the radius of the nanoparticle, d is the distance between the nanoparticle and the electrode, ε is the dielectric constant of the environment [19]. By assuming $d \approx 1\,\mathrm{nm}$ and $\varepsilon \approx 2$ [20] for the dithiothreitol molecules, we can estimate the radius of the nanoparticle, i.e. $r = 7.4\,\mathrm{nm}$

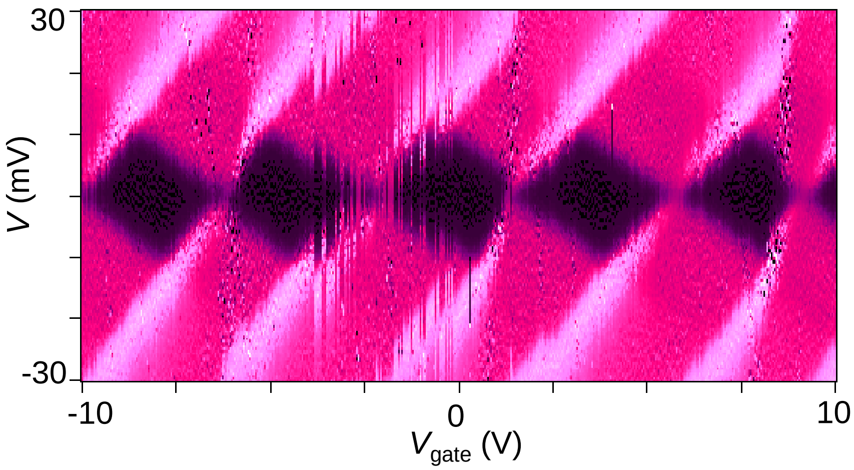

Figure 3.2: Two-dimensional plot of differential conductance as a function of bias voltage and gate voltage of a gold nanoparticle SET fabricated by using electrostatic trapping method. The dark (light) color corresponds to low (high) conductance. The plotted conductance ranges from 0 to 10^{-7} S.

With this method, we have <5% devices showing the Coulomb blockade behaviors and the Coulomb charging energies are ~ 10 meV. This indicates that trapping smaller nanoparticles is difficult. This may due to the lack of detail information of the local electric field around the gap area. The shape of the electrode tip is rarely known because the electromigration process cannot precisely control the breaking of the nanobridge. The electric field $\vec{E}$ at the electrode tip is not controllable. The dielectrophoretic force experienced by the gold nanoparticles in the electric fields is proportional to $\left(\vec{p}\bullet\nabla\right)\vec{E}$ and out of control, where $\vec{p}$ is the dipole of nanoparticle [21, 22].

The major advantage of this technique is that it does not require EBL and other special instrumentation. The initial electrodes with 1 μm gap can be easily fabricated using photolithography. However, its further application in our study is limited by the several disadvantages including (1) the yield of small gap is only 50% [18], (2) the yield of SETs is low as discussed above, (3) the coupling between the nanoparticle and the Si back gate is not efficient. To solve the second issue, we adopted Al gate in this process. However, after the trapping process, the gate electrode becomes unstable and large leakage current is observed.

3.3 PHYSICAL DEPOSITION OF GOLD NANOPARTICLES

To improve the yield of devices and gate coupling, the physical deposition method is introduced. This method consists of two steps. The first step is to fabricate the electrodes with sub-10 nm spacing by applying the electromigration process to the prefabricated Au nanowires [23, 24]. Then the SETs are realized by physical deposition of gold nanoparticles into the nanometer gaps between two electrodes.

The devices are fabricated on top of oxidized silicon wafers. Al gate electrodes are first fabricated by conventional photolithography and electron-beam deposition of Al with the wafer at liquid nitrogen temperature, and subsequently oxidized by exposing to air [25]. Electron-beam lithography using standard PMMA/P(MMA-MAA) bilayer resist is then used to pattern the nanowires. In order to reliably break the gold nanowires, the

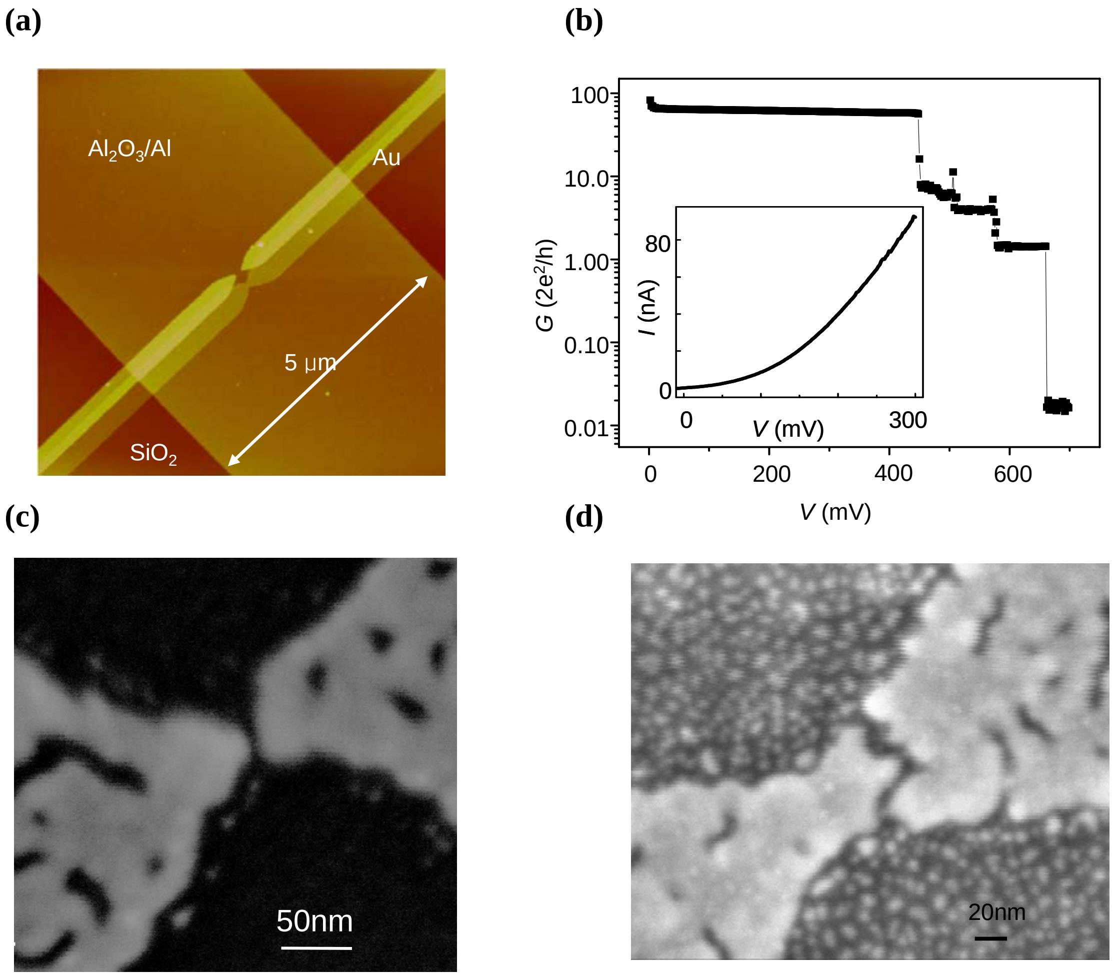

Figure 3.3: Gold nanoparticle SETs fabricated by using the physical deposition of gold nanoparticles. (a) AFM image of an gold nanowire on top of Al gate electrode. (b) Breaking condition of the electromigration process of a bare gold nanowire. (c) HRSEM image of a gold nanowire after electromigration. (d) HRSEM image of an SET with gold nanoparticles deposited into the nanogaps.

cross section at the constriction has to be kept small. To achieve this, gold is evaporated in two steps: ~15 nm of gold is first evaporated normal to the substrate to form the conducting gold nanowires, followed by ~30 nm of gold evaporated at an angle of ~40^o with respect to the substrate normal. The thick layer from the second evaporation ensures the electrical connection between the constriction area and the coarse gold contact pads, but is disconnected in the middle because of the shadow effect and therefore does not increase the cross section of the constriction. The detail fabrication process is presented in detail in reference [26]. An atomic force microscopy (AFM) image of a gold nanowire on top of the Al gate is shown in Fig 3.3 (a).

The nanowires are then cooled down to liquid helium temperature to perform electromigration to create nanometer-sized gaps. A DC voltage is ramped up across the nanowires at a speed of 10 mV per second. The resistance of the nanowires is monitored simultaneously. Fig 3.3 (b) shows one of the representative conductance traces during electromigration. As shown in Fig 3.3 (b), the nanowires start to break at several hundred mV and exhibit a series of discrete conductance decrease steps. These steps imply that the atomic conduction channels are broken up one by one discretely. As the conductance decreases to less than the quantum of conductance, which indicates the complete breaking of nanowires, the process is terminated. The tunneling behavior shown in the inset of Fig 3.3 (b) is always observed after the electromigration which can confirm the complete breaking of gold nanowires. A HRSEM image of the gap after electromigration is shown in Fig 3.3 (c), where the gap size is less than 10 nm. In most devices, the gap sizes are smaller than the resolution limit of our facilities and can not be imaged clearly.

We then put gold nanoparticles into the gaps by thermal evaporation of a thin layer of gold on top of the broken nanowires at room temperature. For most samples, 12 Å gold is evaporated at the rate of ~ 1 Å/s and the pressure of 4×10^{-6} Torr. An HRSEM image in Fig 3.3 (d) shows the broken nanowire with the evaporated 12 Å thick gold on top. Because the gold layer is to thin to form continuous film, gold nanoparticles are formed. The size of the nanoparticles is around 10 nm.

The gold nanoparticle SETs are measured at liquid helium temperature. Fig 3.4 shows the two-dimensional plot of conductance as a function of bias voltage and gate voltage. The conductance suppression regime is observed around zero bias. In our gate voltage region, 13 complete diamond-shaped regions are identified, in which the conductance is suppressed. All the regions show identical sizes.

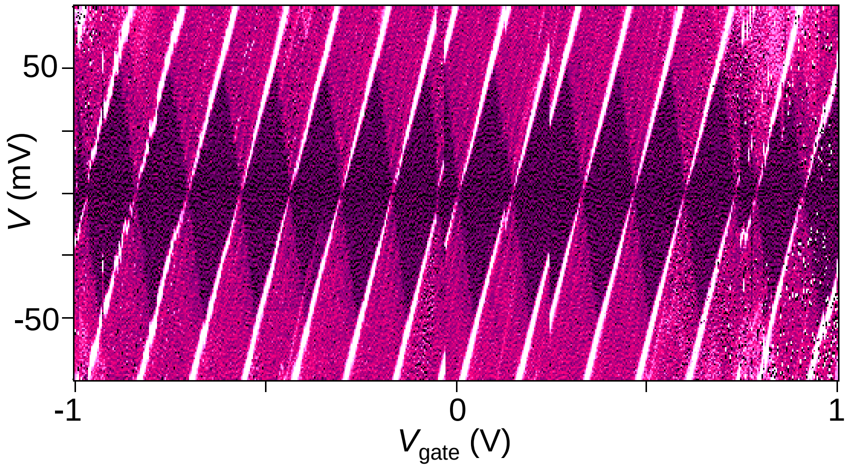

Figure 3.4: Two-dimensional plot of differential conductance as a function of bias voltage and gate voltage of a gold nanoparticle SET fabricated by using physical deposition of gold nanoparticles. The dark (light) color corresponds to low (high) conductance. The plotted conductance ranges from 0 to 10^{-9} S.

These features are characteristic of classical Coulomb blockade. The bias voltage at which the boundaries of Coulomb diamonds intersect is a measure of the Coulomb charing energy, which is ~46 meV. Using the model described in subsection 3.2, the radius of the gold nanoparticles is ~4.4 nm. Here, we assume $d \approx 1\,\mathrm{nm}$ and $\varepsilon \approx 1$ for the vacuum gaps between the nanoparticle and the electrodes. This estimated size is consistent with the size of nanoparticles measured with the HRSEM image shown in Fig 3.3 (d).

With this method, more than 15% of ~50 devices (7 out of 47 devices) show the classical Coulomb blockade behavior. The Coulomb charging energies are ~50 meV.

We carried out similar fabrication process except thicker gold is deposited. We found that the number of short electrodes increases in this case and the yield of nanoparticles SETs decreases. If we evaporate less gold, fewer gold nanoparticles are found and the yield of SETs decreases.

With this method, we can get gold nanoparticle SETs with relatively high yield. But the shape and size of gold nanoparticles are not well controlled.

3.4 SELF-ASSEMBLY OF COLLOIDAL GOLD NANOPARTICLES

The third method is based on the self-assembly of colloidal gold nanoparticles within the gaps between two electrodes. Colloidal gold nanoparticles have well defined shape and uniform size distribution. They constitute a standard model to study the “electron-in-box” quantum states.

This method contains two steps. The first step is to fabricate electrodes with nanometer scale separation. The process in this step involves applying electromigration to the gold nanowires at liquid helium temperature and is the same as the first step of the physical deposition of gold nanoparticles method.

Gold nanoparticles with diameter of ~6 nm are chemically synthesized in toluene and passivated with alkanedithiol molecules [27]. Fig 3.5 (a) shows a transmission electron microscopy (TEM) image of the nanoparticles. The solution is placed onto the device while the wafer is rotating at a speed of 1000 revolutions per minute (1000 RPM). The spin process is used to help the nanoparticles spread on the wafer more uniformly.

Fig 3.5 (b) is an HRSEM image after spin-coating of nanoparticles with the electrodes. The whole devices are fabricated on top of Al gate electrode to implement nanoparticle SETs.

The SETs are measured at *T* = 4.2 K. A plot of two-dimensional conductance as a function of bias voltage and gate voltage is shown in Fig 3.5 (c). The conductance suppression regime is observed around zero bias. Four Coulomb diamonds are identified, in which the conductance is suppressed. The Coulomb charging energy is ~100 meV. The radius of the nanoparticles can be estimated with the charging energy to be ~3 nm. This value is consistent with the TEM image observation.

With this method, we get 3 SETs out of ~50 devices. The yield is ~6%. One possible reason is that it is still difficult to control the density of the gold nanoparticles on the wafer. At different spots on the same wafer, the density of nanoparticles varies a lot.

3.5 COMPARISON

We first compare the yield of SETs from these three methods. The physical deposition of gold nanoparticles shows the highest yield, ~15%. The yields of another two methods are less than 10%. With the physical deposition method, the gold nanoparticles cover the wafer more uniformly; the density of nanoparticles can be controlled by adjust the amount of deposition. While for another two methods, it is difficult to control the placement of the gold nanoparticles in the gaps.

By adopting the Al gate electrode, the gate coupling is improved compared with the Si back gate. The gate capacitance of the SET in Fig 3.2 is 0.45 aF, while for the SETs in Fig 3.4 and Fig 3.5 (c), the gate capacitances are 1.3 aF and 0.74 aF. The larger gate capacitance results from the thinner gate insulation layer and higher dielectric

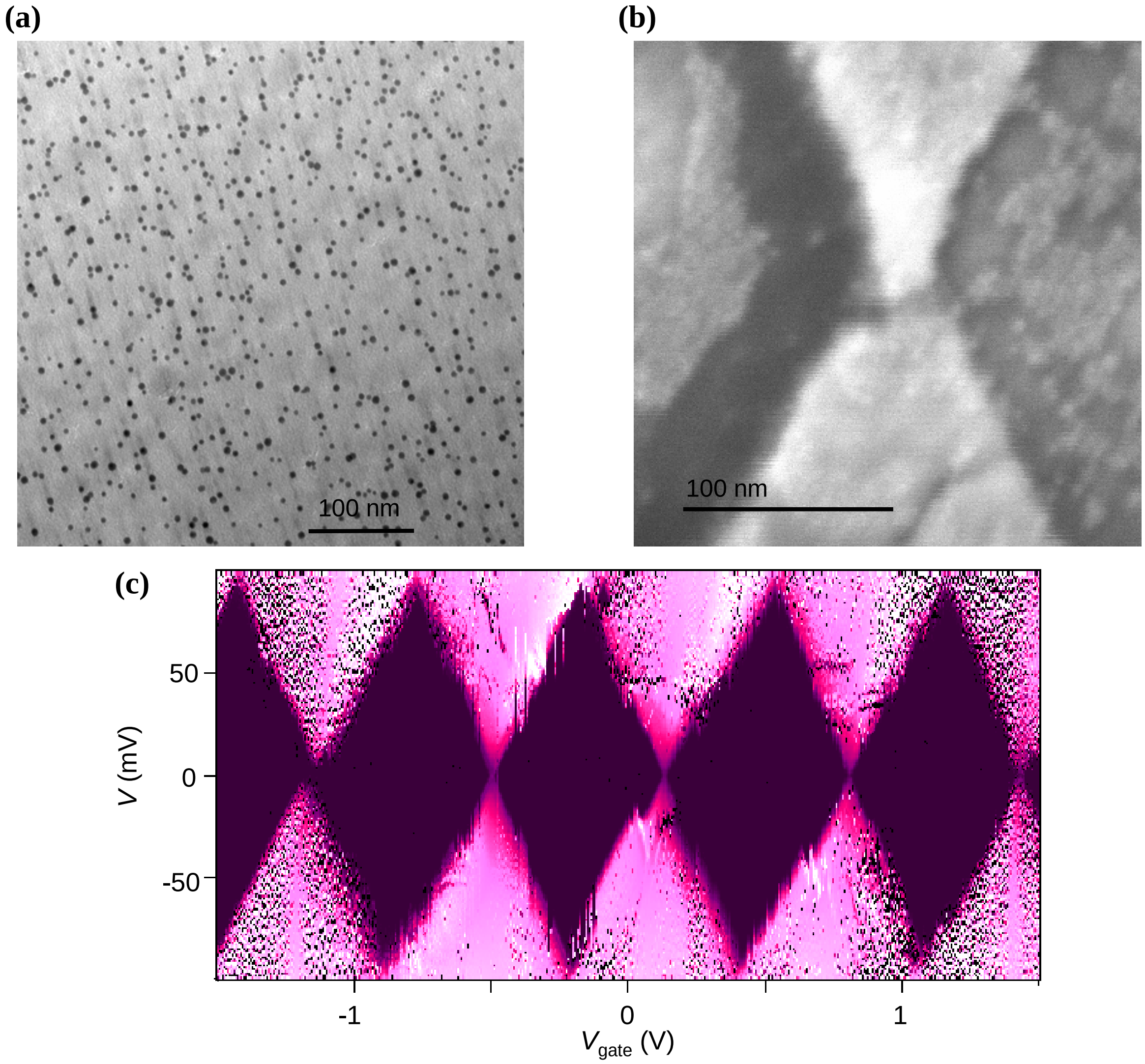

Figure 3.5: Nanoparticle SETs fabricated by using the self-assembly of colloidal gold nanoparticles. (a) TEM image of 6 nm diameter colloid gold nanoparticles. (b) HRSEM image of gold nanoparticles near the pre-created nanogap by electromigration of nanowires. (c) Two-dimensional plot of differential conductance as a function of bias voltage and gate voltage of a gold nanoparticle SET fabricated by using self-assembly of gold nanoparticles. The dark (light) color corresponds to low (high) conductance. The plotted conductance ranges from 0 to 10^{-7} S.

constant of insulation layer. The SiO_2 has the thickness d = 300 nm and $\varepsilon = 2.9$. The Al_2O_3 has the thickness d < 10 nm and $\varepsilon \approx 7$.

In general, the physical deposition of gold nanoparticle method has high yield and strong gate coupling. This method is more promising in the study of nanoparticle SETs.

3.6 SUMMARY

In summary, we have demonstrated three techniques to fabricate gold nanoparticle SETs. The nanometer separated electrodes are created by current-induced electromigration. Various gold nanoparticles are placed into the nanometer gaps between the electrodes to implement nanoparticle SETs with Al/Si back gate electrode. Singe-electron tunneling characteristics are observed. Because of the different sizes of gold nanoparticles, the SETs exhibit different Coulomb charging energies.

REFERENCES

[1] H. D. Graber and M. H. Devoret, *Single Charge Tunneling* (Plenum, New York, 1992).

[2] M. J. Yoo, T. A. Fulton, H. F. Hess, R. L. Willett, L. N. Dunkleberger, R. J. Chichester, L. N. Pfeiffer and K. W. West, Science **276**, 579 (1997).

[3] R. J. Schoelkopf, P. Wahlgren, A. A. Kozhevnikov, P. Delsing and D. E. Prober, Science **280**, 1238 (1998).

[4] K. K. Likharev, Proc. IEEE **87**, 606 (1999).

[5] M. H. Devoret and R. J. Schoelkopf, Nature **406**, 1039 (2000).

[6] R. G. Knobel and A. N. Cleland, Nature **424**, 291 (2003).

[7] J. von Delft and D. C. Ralph, Phys. Rep. **345**, 61 (2001).

[8] D. V. Averin and K. K. Likharev, J. Low Temp. Phys. **62**, 345 (1986).

[9] T. A. Fulton and G. J. Dolan, Phys. Rev. Lett. **59**, 109 (1987).

[10] P. Lafarge, H. Pothier, E. R. Williams, D. Esteve, C. Urbina and M. H. Devoret, Z. Phys. B **85**, 327 (1991).

[11] D. L. Klein, P. L. McEuen, J. E. B. Katari, R. Roth and A. P. Alivisatos, Applied Physics Letters **68**, 2574 (1996).

[12] D. L. Klein, R. Roth, A. K. L. Lim, A. P. Alivisatos and P. L. McEuen, Nature **389**, 699 (1997).

[13] D. C. Ralph, C. T. Black and M. Tinkham, Phys. Rev. Lett. **74**, 3241 (1995).

[14] C. T. Black, Ph. D. Thesis, Harvard University, (1996).

[15] C. T. Black, D. C. Ralph and M. Tinkham, Phys. Rev. Lett. **76**, 688 (1996).

[16] D. C. Ralph, C. T. Black, J. M. Hergenrother, J. G. Lu and M. Tinkham, in *Mesoscopic Electron Transport*, edited by L. P. Kouwenhoven, G. Schon and L. L. Shon (Kluwer Academic Publishers, Dordrecht, The Netherlands, 1997).

[17] D. C. Ralph, C. T. Black and M. Tinkham, Phys. Rev. Lett. **78**, 4087 (1997).

[18] S. I. Khondaker and Z. Yao, Appl. Phys. Lett. **81**, 4613 (2002).

[19] D. L. Klein, Ph. D. Thesis, University of California at Berkeley, (1997).

[20] M. D. Porter, T. B. Bright, D. L. Allara and C. E. D. Chidsey, J. Am. Chem. Soc. **109**, 3559 (1987).

[21] P. Lorrain and D. R. Corson, *Electromagnetic Fields and Waves* (W. H. Freeman, San Francisco, CA, 1970).

[22] T. B. Jones, *Electromechanics of Particles* (Cambridge University Press, Cambridge; New York, 1995).

[23] H. Park, A. K. L. Lim, A. P. Alivisatos, J. Park and P. L. McEuen, Appl. Phys. Lett. **75**, 301 (1999).

[24] D. H. Chae, J. F. Berry, S. Jung, F. A. Cotton, C. A. Murillo and Z. Yao, Nano Lett. **6**, 165 (2006).

[25] A. Bachtold, P. Hadley, T. Nakanishi and C. Dekker, Science **294**, 1317 (2001).

[26] D. H. Chae, Ph. D. Thesis, the University of Texas at Austin, (2006).

[27] The gold nanoparticles are synthesized by Aaron E. Saunders, from Brian A. Korgel's group in the department of chemical engineer at the University of Texas at Austin.

Chapter 4: Room-Temperature Single-Electron Transistors Using Alkanedithiols

4.1 INTRODUCTION

A single-electron transistor (SET) consists of a small conducting island connected to two electron reservoirs through tunnel barriers [1, 2]. If the island is small enough, the electrostatic energy for adding an electron to the island can become greater than the thermal energy. In this regime, electrons tunnel on and off the island one by one, a process that can be precisely controlled by a nearby gate electrode. Although SETs have been considered as promising candidates for future high-density low-power logic and memory devices [2], their applications have been hindered by the difficulty to achieve room-temperature operation, which requires the size of the island to be only a few nanometers. Several techniques for creating room-temperature SETs have been demonstrated [3-8]. However, the fabrication processes have been generally complicated and difficult to reproduce.

In this chapter, I present a simple method for the fabrication of room-temperature SETs based on the self-assembly of alkanedithiol molecules. Our devices consist of spontaneously formed ultrasmall Au nanoparticles linked by alkanedithiols to nanometer-spaced Au electrodes created by electromigration. Because of the small sizes of the Au particles, the devices exhibit extraordinarily large addition energies, which enable SET operation at room temperature. Additionally, excitation structures are observed in the device characteristics, which can be attributed to the well-known vibrational modes of the alkanedithiol molecules.

4.2 DEVICE FABRICATION

Our devices are fabricated on oxidized silicon substrates. Electron-beam lithography is first used to make ~15 nm thick Au nanowires with constrictions of ~100 nm in width on top of naturally oxidized aluminum electrodes acting as gates. The nanowires are then cooled down to 77 K, where a dc voltage is ramped across the wires at a rate of ~10 mV s^{-1} in order to break the wires to create nanometer-spaced gaps via

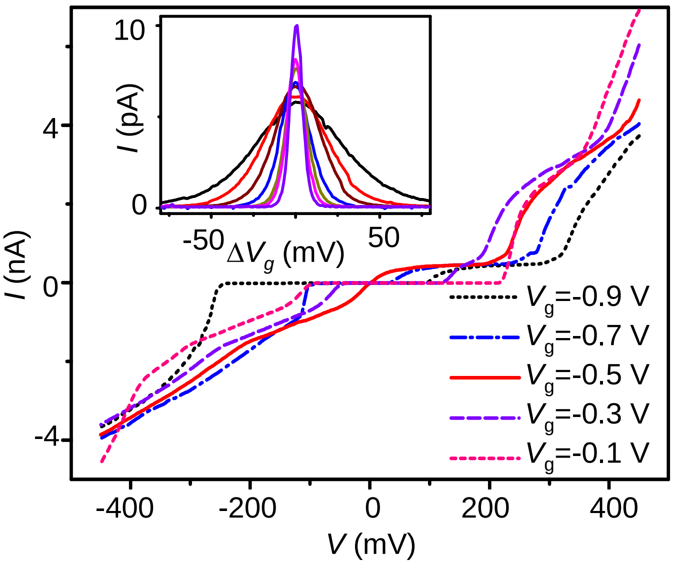

Figure 4.1: Representative *I–V* characteristics from a device incorporating C6 molecules at different gate voltages measured at 4.2 K. The inset shows the current as a function of gate voltage measured with a bias voltage of 0.5 mV at temperatures of 39.0, 25.1, 18.0, 12.3, 7.8, 6.2, and 4.2 K. A higher (lower) and narrower (wider) peak corresponds to lower (higher) temperature. The gate voltage is measured relative to the center of the current peak, which occurs at Vg = −0.5 V.

the electromigration process [9, 10]. The two-terminal resistance of our starting nanowires is 250 Ω, including ~50 Ω series resistance in the circuit. The electromigration process is typically observed as a sudden increase in resistance at ~0.7 V followed by a series of resistance increase steps before the wires are completely broken at ~1 V. After electromigration, the substrates are warmed up to room temperature and are immersed in a solution of 5 mM alkanedithiols in isopropyl alcohol (IPA) for 24 h. The devices are then rinsed in fresh IPA to remove physisorbed alkanedithiol molecules and blown dry with nitrogen gas. Three different alkanedithiolmolecules, butanedithiol (C4), hexanedithiol (C6), and octanedithiol (C8), have been used in our studies. We have also fabricated the devices by performing molecular assembly first and subsequently breaking the Au nanowires in the cryostat at 77 K. The device characteristics are qualitatively the same.

4.3 EXPERIMENTAL RESULTS AND DISCUSSION

Fig. 4.1 shows a set of current–voltage (I–V) characteristics as a function of gate voltage V_{gate} measured at 4.2 K from a device incorporating C6 molecules. The current is strongly suppressed at low bias voltage and the size of the voltage gap can be modulated by the gate. This is a signature of single-electron tunneling effect due to the Coulomb blockade effect [1]. Additional current steps are observed at larger bias in the I–V curves. These generally occur when the excited states of the system enter the bias voltage window providing additional current pathways [11]. These features can be more clearly seen in the two-dimensional color plot of numerical differential conductance ($\mathrm{d}I/\mathrm{d}V$) as shown in Fig 4.2. Three dark diamond-shaped regions in which the current is blockaded can be identified and signify three successive charge states. Peaks in $\mathrm{d}I/\mathrm{d}V$ corresponding to the current steps are manifested as lines parallel to the boundaries of the Coulomb blockade. Qualitatively similar features have been observed in other C6 devices as well as devices incorporating C4 and C8 molecules. Overall we have studied a total of

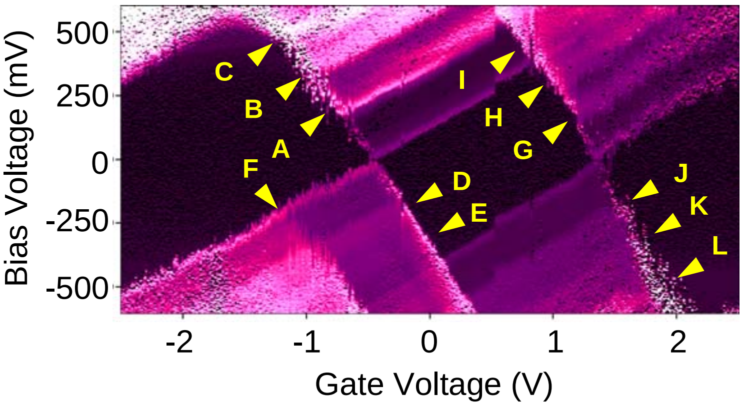

Figure 4.2: Two-dimensional color plot of differential conductance as a function of bias voltage and gate voltage measured at 4.2 K from the same C6 device as shown in figure 4.1. A bright (dark) color corresponds to high (low) conductance. The plotted conductance ranges from 10^{-12} to 10^{-7} S.

165 C6 and 10 C4 and 25 C8 devices, among which 19 C6, 1 C4 and 3 C8 devices display *I–V* curves with large voltage gaps ($\gtrsim$300 mV) and gate modulation. Furthermore, 22 of these devices exhibit excitation structures in the conductance map. We note, however, that the device in Fig 4.1 and Fig 4.2 is the only one in which three consecutive charge states can be accessed due to the limited voltage range that can be applied to the aluminium gate before the gate oxide breaks down. All the other devices show only one charge degeneracy point between two adjacent charge states.

We first focus on the excitation structures. In the Coulomb blockade model, the energies of the excited states in a particular charge state can be obtained directly from the bias voltage values at which the lines associated with the excited states intersect the boundaries of the Coulomb blockade in that charge state. The most common origin for the excitations is discrete electronic energy levels which occur in, for example, small semiconductor quantum dots and carbon nanotubes [11, 12]. In molecular systems, however, it has been shown that electronic transport can be strongly coupled to vibrational excitations [10, 13-15]. Significantly, the excitations in Fig 4.2 are almost equally spaced and they appear for both bias polarities around both charge degeneracy points with approximately the same values. These features strongly suggest that the excitations are vibrational in nature. In particular, multiple excitations can be naturally explained by the excitations of multiple vibrational quanta.

Table 4.1: The excitation energies observed in Figure 4.2.

	Energy (mV)		**Energy (mV)**		**Energy (mV)**		**Energy (mV)**
A	**178**	**D**	**164**	**G**	**176**	**J**	**176**
B	**326**	**E**	**324**	**H**	**325**	**K**	**325**
C	**484**	**F**	**184**	**I**	**446**	**L**	**446**

Table 4.1 lists the values of the excitation energies extracted from the data in Fig 4.2. The lowest energy is in the range of 160–185 meV. Remarkably, this is consistent with the well-known twisting (~160 meV), wagging (~160 meV), and scissoring (~180 meV) modes of the CH_2 groups, which have previously been characterized extensively using a variety of techniques [16-18]. To gain more insight into the excitations, we plot the histogram of the excitation energies extracted from all 22 devices that showed excitation structures in Fig 4.3. In addition to the appearance of the CH_2 vibrational modes in the range of 160–190 meV, the histogram is characterized by prominent peaks at 30 and 120 meV. These energies agree very well with the Au–S stretch and C–C

stretch [16, 17] modes. Interestingly, these modes have also been identified in the inelastic electron tunneling spectroscopy studies of alkanedithiol self-assembled monolayers [19, 20]. Taking these together, we believe that most of the excitations in our data are indeed associated with molecular vibrations.

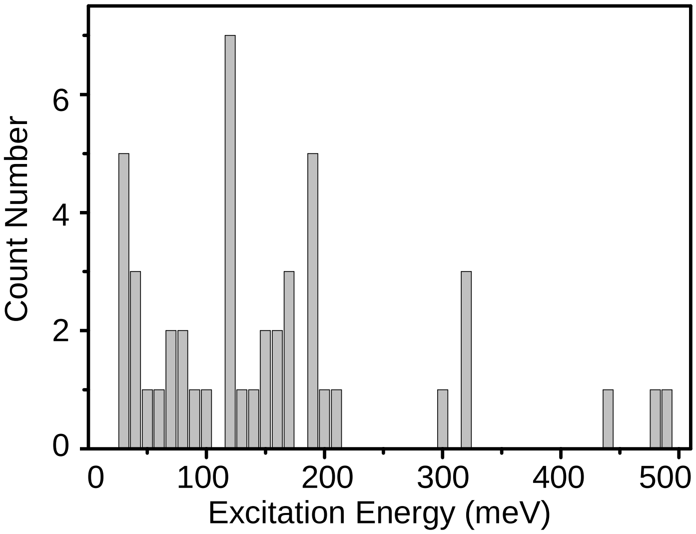

Figure 4.3: Histogram of the observed excitation energies from 22 devices. The bin size is 10 meV.

The observed Coulomb blockade effect suggests that there exist well-defined charge states in the central island. To further elucidate the transport mechanism, we measured one of the conductance peaks for the device shown in Fig 4.1 at different temperatures, as shown in the inset to Fig 4.1. As the temperature *T* increases, the height of the peak decreases as 1/*T*, while the full width at half maximum increases in proportion to temperature. This behavior signifies that the transport occurs via tunneling through discrete electronic states in the central island [11].

The observed transport characteristics are not possible if the two Au electrodes in our devices are directly bridged by one or a few alkanedithiol molecules. This is because these molecules are known to be insulating with a large gap (~8 eV) between the highest occupied molecular orbital (HOMO) and the lowest unoccupied molecule orbital (LUMO) [21-23]. When the molecules are connected to the Au electrodes, the Fermi energy of the electrodes lies deep in the gap, leading to direct tunneling transport which has been consistently observed in different measurement geometries [19, 20, 24-27]. The charge degeneracy points observed in our devices suggest electronic states which are only hundreds of meV away from the Fermi level of Au electrodes. These states cannot be attributed to the HOMO and LUMO of the molecules.

The only other possibility that can explain the observed behavior is the transport through Au nanoparticles. It has been known that small Au nanoparticles can form in the nanogaps during electromigration, which often leads to the Coulomb blockade behavior [28-32]. The size of the particles and the frequency at which they occur depend critically on the breaking conditions. We have carried out control experiments in 65 devices by performing electromigration in Au nanowires at 77 K followed by warming up the devices to room temperature and then cooling down to low temperatures without alkanedithiol assembly. Among these devices, only two showed gated transport with small addition energies and no excitation features. As mentioned earlier, 22 out of 165 devices with alkanedithiol assembly exhibited addition energies larger than 300 meV as well as distinct excitation features. The disparity clearly suggests that the molecular self-assembly process is responsible for the formation of the ultrasmall Au nanoparticles in the present devices. This may not be too surprising considering the strong chemical

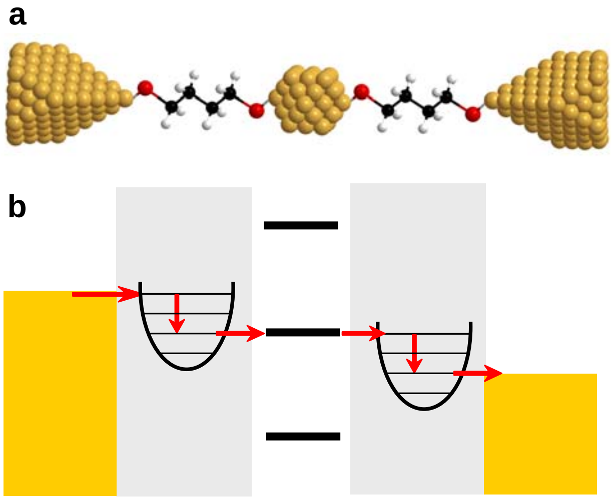

Figure 4.4: (a) Schematic of our proposed device geometry. (b) Energy level diagram for the transport processes.

between Au and sulfur end groups during the assembly process. Fig 4.4 (a) is a schematic drawing that we believe describes the transport characteristics of our devices, showing the Au nanoparticles bound to the nanometer-spaced electrodes by alkanedithiols which act as tunnel barriers. As indicated in the energy diagram in Fig 4.4 (b), the electrons tunnel through the discrete electronic states in the Au nanoparticles. As the electrons tunnel across the alkanedithiol tunnel barriers, molecular vibrations can be excited.

We can roughly estimate the size of the Au nanoparticle for the device as shown in Fig 4.1 and Fig 4.2. For an isolated particle of radius r, the charging energy E_c scales as $1/r$, while the energy level spacing ΔE scales as $1/r^3$. Thus the energy level spacing is expected to become increasingly important for smaller particles. The addition energy depends on whether the initial number of electrons is even or odd. For an even number of electrons, the addition of an extra electron requires energy of $E_c + \Delta E$, whereas for an odd number of electrons, the addition energy is simply E_c because the added electron can occupy the same energy level as the topmost electron. The alternating large and small addition energies for the three successive charge states observed in Fig 4.2 seem to be consistent with the even–odd effect. We can therefore associate the difference in the addition energies between the left two charge states (the addition energy of the rightmost charge state cannot be determined because the maximum voltage gap is not seen), which is 190 meV, with the energy level spacing. Using $\Delta E = 2E_F/3N$ [33], where $E_F \sim 5.5$ eV is the Fermi energy of Au and N the number of electrons, we estimate that the nanoparticle contains only ~ 20 Au atoms.

The quantum energy level spacing ΔE is comparable to the charging energy E_c. The tunneling occurs through a single level and it is in quantum Coulomb blockade regime. The experimental data are studied with quantum Coulomb blockade theory. Fig 4.5 (a) shows the current as a function of gate voltage measured with a bias voltage of 0.5 mV at 6.2 K from the same C6 device as shown in figure 1. The open circles are experimental data. The data are fitted by formula (2.6) and the fitting curve is shown as the red solid line. In Fig 4.5 (b), the current peak heights at Vg = −0.5 V is plotted at various temperatures. The peak heights are extracted from the data shown in the inset of Fig 4.1. From formula (2.6), as $\delta = 0$, the peak height is inversely proportional to temperature $G = G_\infty \frac{\Delta E}{4k_B T}$. This is confirmed by the good linear fitting between the current peak heights I and inverse temperature T^1 shown as red solid line. The good agreement between experimental data and theory prediction further justified our assumption that the electron tunneling transport must occur through single quantum level in the extreme small gold nanoparticle.

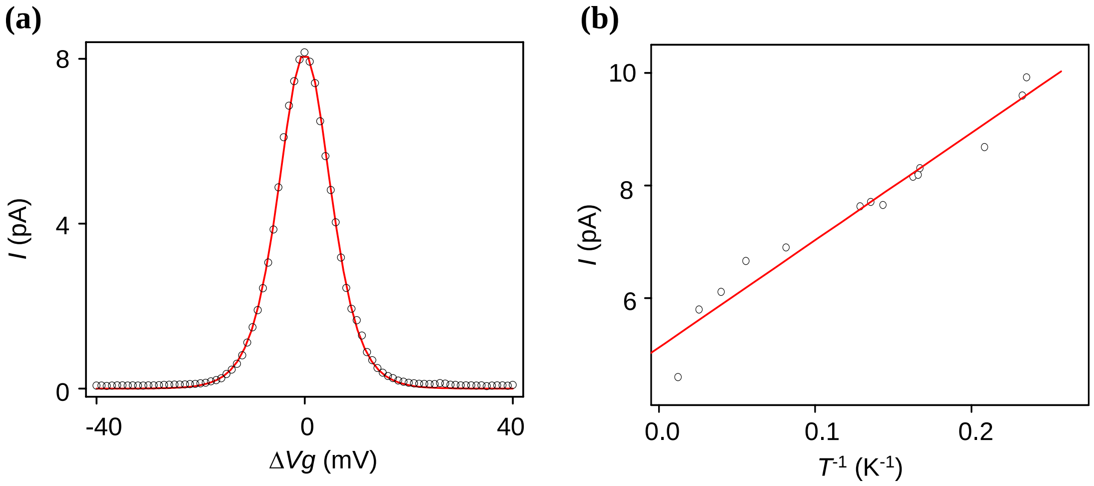

Figure 4.5: (a) Current as a function of gate voltage measured with a bias voltage of 0.5 mV at 6.2 K from the same C6 device as shown in figure 4.1. The open circles are experimental data and the solid line corresponds to the theoretical fitting curve predicted by quantum Coulomb blockade theory. The gate voltage is measured relative to the center of the current peak, which occurs at *V*g = −0.5 V. (b) Current peak height at *V*g = −0.5 V as a function of temperature. The open circles are experimental data and the solid line corresponds to the prediction by quantum Coulomb blockade theory.

The addition energies in our devices are well above the thermal energy at room temperature (26 meV at 300 K) and are also much higher than the values reported in previous SETs operating at room temperature [3-8]. This suggests the possibility of our devices to operate at high temperatures. Fig 4.6 shows the conductance plots from the same device as shown in Fig 4.2 measured at 77, 150 K, and room temperature (290 K). Similar behavior has also been observed in a few other devices. At both 4.2 and 77 K, the Coulomb blockade as well as the excitation features can be clearly observed. As the temperature increases further, the excitation structures become smeared out. Nevertheless, the diamond structures associated with the Coulomb blockade persist up to room temperature. Note that the conductance plot seems to have shifted along the gate axis with respect to the low-temperature data, indicating a change in the local electrostatic environment presumably due to the charge trap noise in the gate oxide. We expect that by optimizing the substrates and gate structures, more stable operation can be achieved at room temperature.

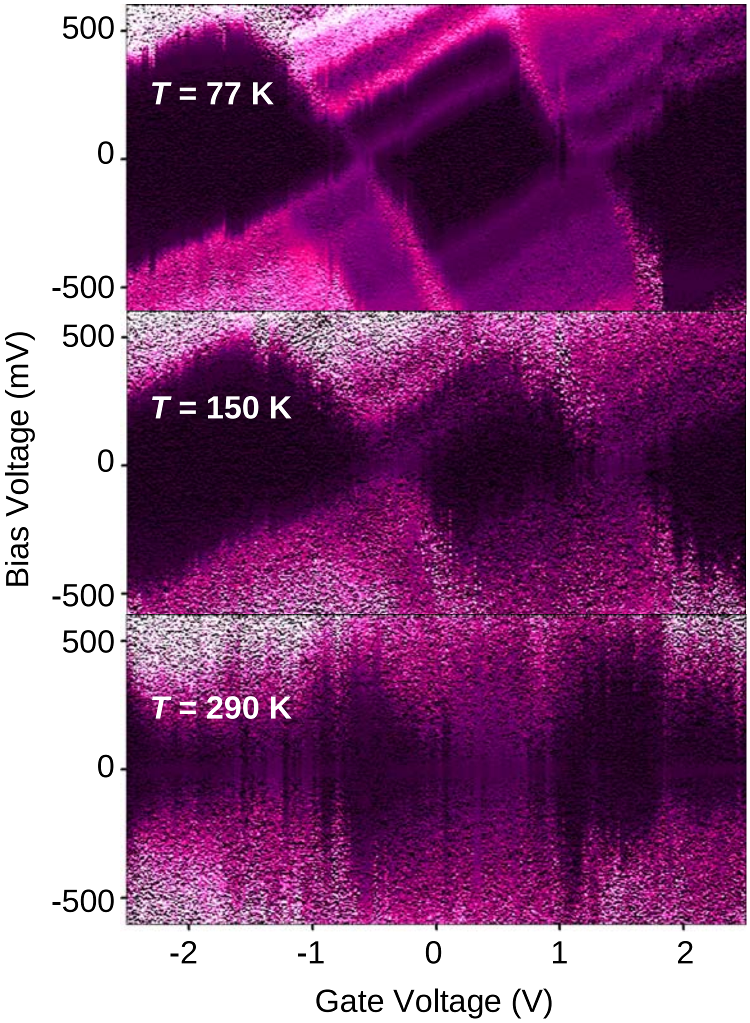

Figure 4.6: Color plots of differential conductance versus bias and gate voltages from the same device as shown in figure 4.1 measured at different temperatures. A bright (dark) color corresponds to high (low) conductance. The plotted conductance ranges from 10^{-12} to 1.2×10^{-7} S.

4.4 SUMMARY

In conclusion, we have fabricated SETs consisting of ultrasmall Au nanoparticles connected to nanometer-spaced Au electrodes through alkanedithiol molecular tunnel barriers. Clear single-electron tunneling behavior can be observed at room temperature because of the very large addition energies of the devices. Low-temperature transport shows features associated with excitations of molecular vibrations in alkanedithiols.

REFERENCES

[1] H. D. Graber and M. H. Devoret, *Single Charge Tunneling* (Plenum, New York, 1992).

[2] K. K. Likharev, Proc. IEEE **87**, 606 (1999).

[3] Y. Takahashi, M. Nagase, H. Namatsu, K. Kurihara, K. Iwdate, K. Nakajima, S. Horiguchi, K. Murase and M. Tabe, Electron. Lett. **31**, 136 (1995).

[4] K. Matsumoto, M. Ishii, K. Segawa, Y. Oka, B. J. Vartanian and J. S. Harris, Appl. Phys. Lett. **68**, 34 (1996).

[5] L. Zhuang, L. J. Guo and S. Y. Chou, Appl. Phys. Lett. **72**, 1205 (1998).

[6] H. W. C. Postma, T. Teepen, Z. Yao, M. Grifoni and C. Dekker, Science **293**, 76 (2001).

[7] K. Matsumoto, S. Kinoshita, Y. Gotoh, K. Kurachi, T. Kamimura, M. Maeda, K. Sakamoto, M. Kuwahara, N. Atoda and Y. Awano, Jpn. J. Appl. Phys., Part 1 **42**, 2415 (2003).

[8] C. Dubuc, J. Beauvais and D. Drouin, Appl. Phys. Lett. **90**, 113104 (2007).

[9] H. Park, A. K. L. Lim, A. P. Alivisatos, J. Park and P. L. McEuen, Appl. Phys. Lett. **75**, 301 (1999).

[10] D. H. Chae, J. F. Berry, S. Jung, F. A. Cotton, C. A. Murillo and Z. Yao, Nano Lett. **6**, 165 (2006).

[11] L. P. Kouwenhoven, C. M. Marcus, P. L. McEuen, S. Tarucha, R. M. Westervelt and N. S. Wintergreen, in *Mesoscopic Electron Transport*, edited by L. P. Kouwenhoven, G. Schon and L. L. Shon (Kluwer Academic Publishers, Dordrecht, The Netherlands, 1996).

[12] Z. Yao, C. Dekker and P. Avouris, Top. Appl. Phys. **80**, 147 (2001).

[13] H. Park, J. Park, A. K. L. Lim, E. H. Anderson, A. P. Alivisatos and P. L. McEuen, Nature **407**, 57 (2000).

[14] L. H. Yu, Z. K. Keane, J. W. Ciszek, L. Cheng, M. P. Stewart, J. M. Tour and D. Natelson, Phys. Rev. Lett. **93**, 266802 (2004).

[15] A. N. Pasupathy, J. Park, C. Chang, A. V. Soldatov, S. Lebedkin, R. C. Bialczak, J. E. Grose, L. A. K. Donev, J. P. Sethna, D. C. Ralph and P. L. McEuen, Nano Lett. **5**, 203 (2005).

[16] C. Castiglioni, M. Gussoni and G. Zerbi, J. Chem. Phys. **95**, 7144 (1991).

[17] M. A. Bryant and J. E. Pemberton, J. Am. Chem. Soc. **113**, 8284 (1991).

[18] H. S. Kato, J. Noh, M. Hara and M. Kawai, J. Phys. Chem. B **106**, 9655 (2002).

[19] W. Y. Wang, T. Lee, I. Kretzschmar and M. A. Reed, Nano Lett. **4**, 643 (2004).

[20] J. G. Kushmerick, J. Lazorcik, C. H. Patterson, R. Shashidhar, D. S. Seferos and G. C. Bazan, Nano Lett. **4**, 639 (2004).

[21] M. Fujihira and H. Inokuchi, Chem. Phys. Lett. **17**, 554 (1972).

[22] S. G. Lias, J. E. Bartmess, J. F. Liebman, J. L. Holmes, R. D. Levin and W. G. Mallard, J. Phys. Chem. Ref. Data Suppl. **17**, 1 (1988).

[23] C. Boulas, J. V. Davidovits, F. Rondelez and D. Vuillaume, Phys. Rev. Lett. **76**, 4797 (1996).

[24] D. J. Wold and C. D. Frisbie, J. Am. Chem. Soc. **122**, 2970 (2000).

[25] X. D. Cui, A. Primak, X. Zarate, J. Tomfohr, O. F. Sankey, A. L. Moore, T. A. Moore, D. Gust, G. Harris and S. M. Lindsay, Science **294**, 571 (2001).

[26] B. Q. Xu and N. J. J. Tao, Science **301**, 1221 (2003).

[27] W. Y. Wang, T. Lee and M. A. Reed, Phys. Rev. B **68**, 035416 (2003).

[28] J. I. Gonzalez, T. H. Lee, M. D. Barnes, Y. Antoku and R. M. Dickson, Phys. Rev. Lett. **93**, 147402 (2004).

[29] R. Sordan, K. Balasubramanian, M. Burghard and K. Kern, Appl. Phys. Lett. **87**, 013106 (2005).

[30] A. A. Houck, J. Labaziewicz, E. K. Chan, J. A. Folk and I. L. Chuang, Nano Lett. **5**, 1685 (2005).

[31] H. B. Heersche, Z. de Groot, J. A. Folk, L. P. Kouwenhoven, H. S. J. van der Zant, A. A. Houck, J. Labaziewicz and I. L. Chuang, Phys. Rev. Lett. **96**, 017205 (2006).

[32] T. Taychatanapat, K. I. Bolotin, F. Kuemmeth and D. C. Ralph, Nano Lett. **7**, 652 (2007).

[33] C. Kittel, *Introduction to Solid State Physics* (Wiley, New York, 2004).

Chapter 5: Fabrication of Nanometer-Spaced Superconducting Pb Electrodes

5.1 INTRODUCTION

Over the past few years, development of techniques for making nanometer-spaced metal electrodes has enabled the fabrication of devices incorporating individual nanostructures including molecules [1-7] and nanoparticles [8-11]. Similar to lithographically patterned semiconductor quantum dots [12, 13] these devices have shown the Coulomb blockade behavior [1, 2, 4, 7-9] and the many-body Kondo effect [2, 3, 5, 6, 10, 11] which results from the screening of localized impurity spins in the central molecule or nanoparticle by conduction electrons in the electrodes. These devices offer the advantage that their metal electrodes can in principle be made with different materials which could allow the transport to be probed in new regimes that are not accessible in semiconductor quantum dots and potentially lead to devices with new functionalities. Of particular interest are magnetic or superconducting electrodes. For example, spin-polarized transport has been studied in single-C_{60} molecular transistors using ferromagnetic Ni electrodes in the Kondo regime [6], where the Kondo effect was found to be suppressed leading to highly nontrivial magnetoresistance behavior. Superconducting Al has been used as electrodes in the transport study of individual carbon nanotubes and nanowires [14-16]. To the best of our knowledge, however, superconducting electrodes with nanometer-sized separation has not been demonstrated.

In this chapter, I present the realization of superconducting Pb electrodes with nanometer-sized gap. We choose Pb because its superconducting transition temperature, T_c, is well above the liquid helium temperature, which should facilitate the general use of these electrodes. The fabrication is achieved by electromigration-induced breaking of a conducting Pb wire patterned by electron-beam lithography. These electrodes exhibit current-voltage characteristics consistent with the tunneling between two superconductors. The electrodes can be switched reversibly between the normal and superconducting states by changing the temperature or by applying an external magnetic field.

5.2 DEVICE FABRICATION

The fabrication process starts by using photolithography to make Cr/Au (5nm/25nm) contact pads and a 30 nm thick Al gate electrode (not used in the data presented in this paper) on top of oxidized Si substrates. Electron-beam lithography using standard PMMA/P(MMA-MAA) bilayer resist is then performed to define the Pb wire, which is ~500 nm in width and has a constriction of ~100 nm in the middle. Pb is thermally evaporated in a vacuum chamber with a base pressure of $\sim 8 \times 10^{-7}$ Torr. During evaporation, the substrate is kept at liquid nitrogen temperature in order to minimize the roughness and grain size of the Pb film. In order to reliably break the Pb wire, the cross section at the constriction has to be kept small. To achieve this, Pb is evaporated in two steps: ~50 nm of Pb is first evaporated normal to the substrate forming the conducting Pb bridge, followed by ~100 nm of Pb evaporated at an angle of $\sim 40^{o}$ with respect to the substrate normal. The thick layer from the second evaporation ensures the electrical connection between the Pb wire and the coarse Au contact pads, but is disconnected in the middle because of the shadow effect and therefore does not increase the cross section of the constriction. The inset to Fig. 5.1 (a) shows a scanning electron microscope (SEM) image of the resultant Pb bridge.

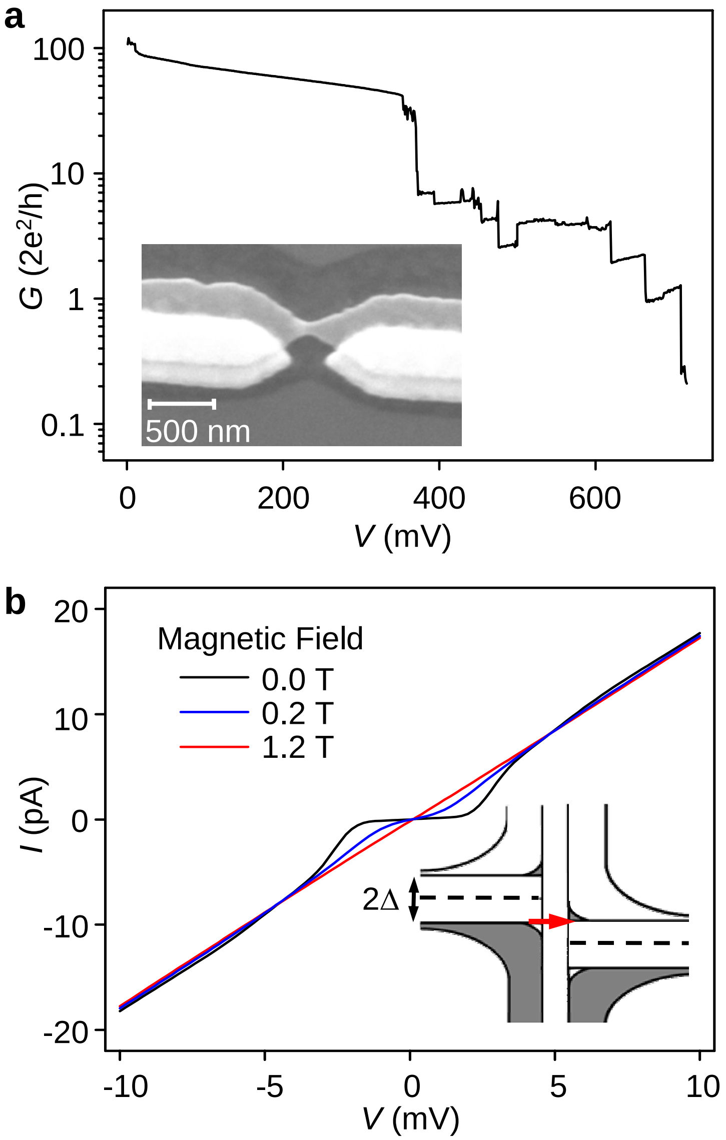

Figure 5.1: (a) Representative conductance trace during the electromigration process. The inset shows an SEM image of a Pb wire before breaking. (b) *I*-*V* characteristics between the Pb electrodes after electromigration at 4.2 K in different magnetic fields. The inset depicts the quasiparticle tunneling process between two superconductors.

To create nanometer-sized gaps in the Pb wires, electromigration is carried out at liquid helium temperature. During cool down, the resistance of the Pb bridge shows an abrupt decrease at 7.2 K, signaling the transition of Pb from the normal to the superconducting state. The Pb bridge is broken by slowly ramping up a dc voltage at a rate of ~10 mV/s across the bridge [7, 17]. Figure 5.1 (a) shows a representative conductance trace during the electromigration process. At the bias voltage of ~11 mV, there is a small sudden decrease in conductance, which is consistently observed in all our devices. This can be attributed to the transition of Pb from the superconducting to the normal state in the constriction. Indeed, the current density through the constriction is estimated to be ~10^7 A/cm^2, which is comparable to the critical current density of Pb [18]. As the bias voltage increases further, the Pb bridge starts to break at ~370 mV as manifested by an abrupt decrease in conductance. This is followed by a series of conductance steps before the conductance eventually drops to a value lower than the conductance quantum at ~700 mV, which indicates that the bridge has been completely broken.

We have broken a total of 347 Pb wires. Among these, 151 electrode pairs showed no measurable current after breaking suggesting the formation of large gaps. 182 pairs displayed measurable current with no gate voltage modulation and overall characteristics similar to those presented below. These are associated with the formation of nanometer-sized tunneling gaps in the Pb wires and are the focus of this paper. We did not observe supercurrents in any of the devices, presumably because the final tunnel resistances were too high. There are also 14 devices which exhibited superconducting single-electron transistor behavior and the detailed characteristics will be presented in next chapter. These devices can be explained by the formation of Pb nanoparticles within the gaps during electromigration, similar to the Au nanoparticles which are known to occasionally form in electromigrated Au junctions [10, 11, 19].

5.3 EXPERIMENTAL RESULTS AND DISCUSSION

Fig 5.1 (b) shows representative current-voltage (*I*-*V*) characteristics measured across a pair of Pb electrodes after breaking at 4.2 K. In the absence of a magnetic field, the current shows strong suppression around zero bias. Above a certain threshold voltage, the current rises sharply. Furthermore, the current is symmetric with respect to the bias polarity. The voltage gap corresponding to the maximum slope in *I*-*V* is around 3 meV. The gap is suppressed upon the application of a magnetic field *B* as shown in Fig. 5.1 (b). At B = 1.2 T, the gap completely vanishes and the *I*-*V* becomes approximately linear. Similarly, the gap can also be suppressed by increasing the temperature as shown in Fig. 5.2, and disappears completely at 7.2 K, T_c of Pb.

These characteristics are consistent with the tunneling between two superconducting electrodes. The energy diagram for the quasiparticle tunneling process is depicted in the inset of Fig. 5.1 (b). At small bias voltage, the absence of quasiparticle density of states (DOS) within the superconducting energy gap, 2Δ, results in the suppression of quasiparticle tunneling current. When a potential difference equal to 2Δ is applied, the alignment of the DOS peaks at the gap edge gives rise to a sharp increase in the tunneling current. As the temperature increases or when an external magnetic field is applied, the superconducting gap becomes smaller and the peaks in DOS decrease, leading to smaller voltage gap with more gradual increase of current around the gap edge.

We can analyze the *I*-*V* characteristics quantitatively within the Bardeen-Cooper-Schrieffer (BCS) theory [18]. The tunneling current can be expressed as

$$I = G_N \int_{-\infty}^{\infty} \rho(E)\rho(E+V)\left[f(E) - f(E+V)\right]dE \qquad (5.1)$$

where $\rho(E)$ is the DOS of quasiparticles, f is Fermi-Dirac function, and G_N is the normal-state conductance of the junction. We find that good fits of the experimental data are obtained by using a modified BCS DOS proposed by Dynes *et al.* [20], $\rho(E,\Gamma)=(E-i\Gamma)/\left[(E-i\Gamma)^2-\Delta^2\right]^{1/2}$, where Γ is a phenomenological parameter used to

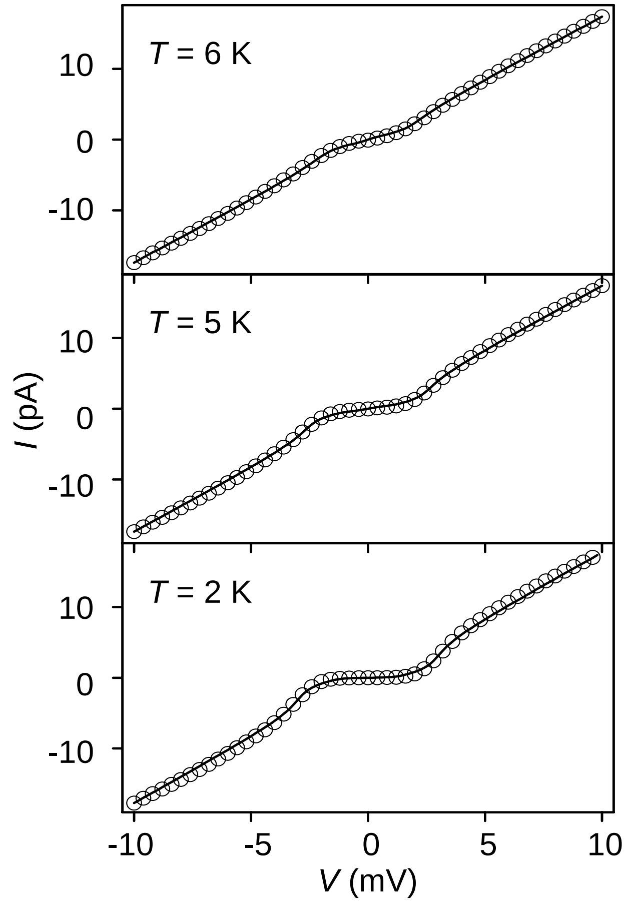

Figure 5.2: *I-V* curves between nanometer-spaced Pb electrodes at different temperatures. The open circles are experimental data and the solid lines are fitting curves using modified BCS DOS with Δ and Γ as adjustable parameters.

describe the broadening of the singularity peaks at the gap edge. The solid lines in Fig. 5.2 are the fitting curves using different values of Δ and Γ at different temperatures as adjustable parameters.

Figure 5.3 (a) plots $\Delta(T)$ normalized to the zero-temperature gap value $\Delta(0)$ (for which we use the gap value at 1.8 K, Δ = 1.46 meV) as a function of temperature T normalized to T_c. The behavior can be very well described by the BCS theory [18] as shown by the solid curve. The ratio of $2\Delta(0)/k_B T_C \sim 5$ is consistent with the fact that Pb is a strongly coupled superconductor. The temperature dependence of the Γ values extracted from the fitting can be used to infer the mechanism for the smearing of the energy gap. One possible mechanism is the shortened quasiparticle lifetime due to the recombination of quasiparticles at or near the energy gap edge to form Cooper pairs with phonon emission. Within this mechanism, the quasiparticle lifetime τ is given by [21]:

$$\frac{1}{\tau} = \left(\frac{k_B T}{\Delta}\right)^{1/2} \frac{1}{\tau_0} \exp(-\Delta / k_B T) \tag{5.2}$$

where τ_0 is related to the electron-phonon coupling strength. Fig. 5.3 (b) displays τ, which is calculated from the experimental Γ value by $\Gamma\tau \approx \hbar/2$, as a function of $k_B T/\Delta$. The good agreement with the above expression (solid line) confirms that the reduced quasiparticle lifetime due to recombination indeed contributes to the gap broadening observed in our *I-V* characteristics.

Finally we describe an interesting feature which is consistently observed from our devices at high bias voltage. Fig 5.4 shows the current, differential conductance and second derivative d^2I/d^2V data taken at T = 4.2 K from sample A as a function of bias

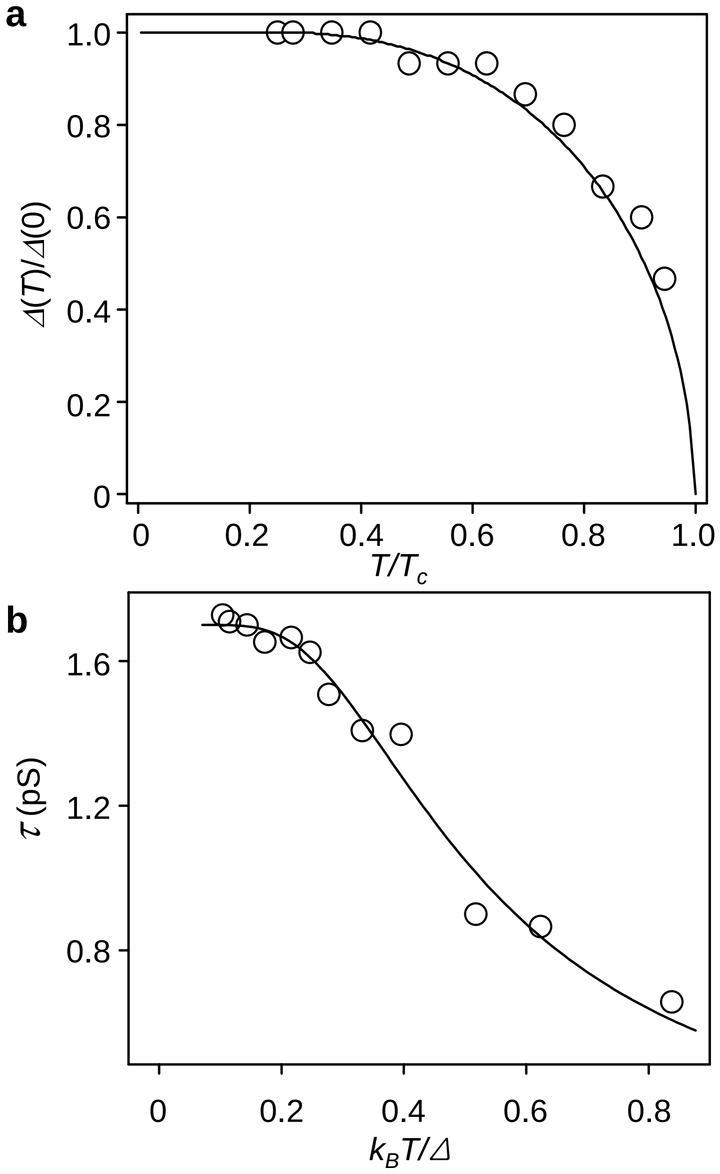

Figure 5.3: (a) Measured superconducting energy gaps at various temperatures normalized to the gap value at 1.8 K as a function of temperature scaled by T_c . The open circles are experimental data and the solid line corresponds to the prediction by the BCS theory. (b) Measured quasiparticle lifetime as a function of temperature scaled by energy gap. The open circles are experimental data and the solid line is a theoretical fitting curve predicted by the quasiparticle recombination model.

voltage. This device has higher conductance in normal state and the features can be distinguished more clearly than the sample shown in Fig 5.1. As indicated by the arrows in Fig 5.4, fine step increases of current, peaks in conductance and dips in d^2I/d^2V are observed. These features consistently happen at bias voltages of 7 mV and 11 mV. These features can be attributed to phonon excitation modes. During the tunneling transport, the phonon excitations are excited and result in conductance peaks in the tunneling spectroscopy. The phonon energies can be extracted as ~4.4 meV and ~8.4 meV, which are the values of the bias voltage where the peaks are observed minus 2Δ. These energies coincide with the energy of the transverse and longitudinal phonon modes of Pb [22-24]. The phonon spectral function $\alpha^2(\omega)F(\omega)$ and the strength of the electron-phonon coupling can be in principle obtained from the tunneling data [23, 24].

5.4 SUMMARY

In summary, we have developed a simple and reproducible technique to create a pair of superconducting electrodes with nanometer-sized separation. Well-behaved *I-V* characteristics across the junctions consistent with tunneling between two superconductors are observed, confirming the small sizes and high quality of the tunnel junctions. We believe that these nanoscale electrodes have opened up opportunities for exploring new transport phenomena in devices incorporating individual chemical nanostructures.

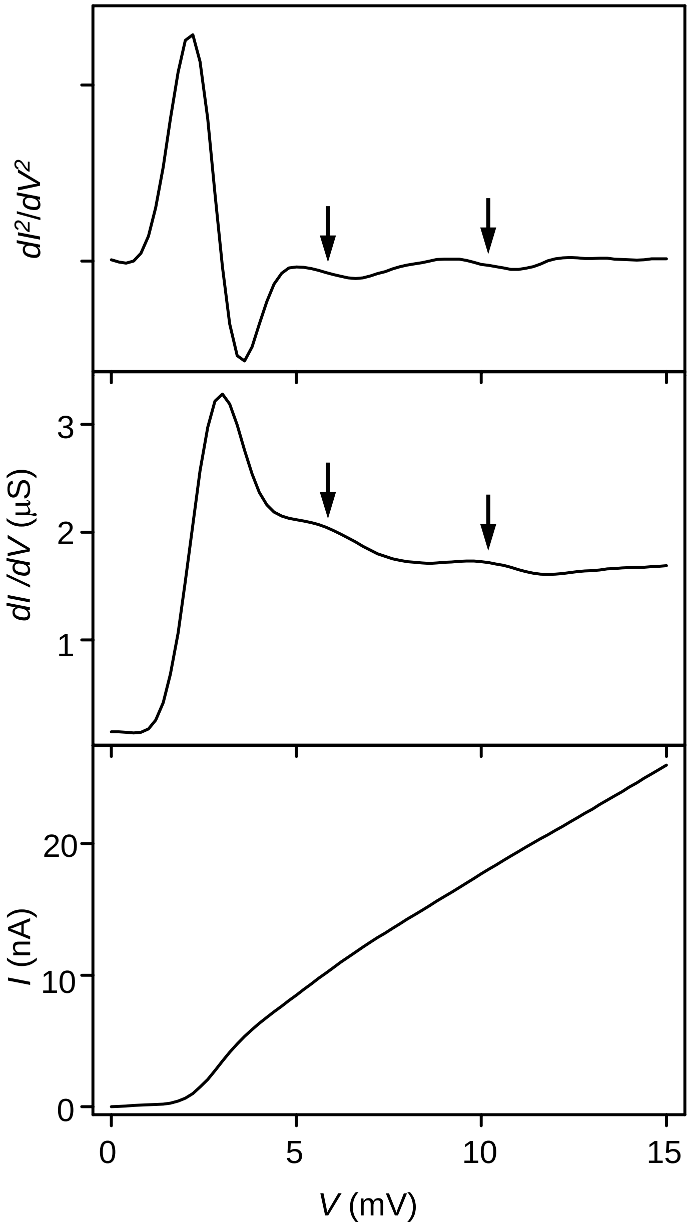

Figure 5.4: (a) *I*-*V* curve between nanometer-spaced Pb electrodes (sample A). (b) Differential conductance versus bias voltage from sample A. (c) Second derivative d^2I/d^2V as a function of bias voltage from sample A.

REFERENCES

[1] H. Park, J. Park, A. K. L. Lim, E. H. Anderson, A. P. Alivisatos and P. L. McEuen, Nature **407**, 57 (2000).

[2] J. Park, A. N. Pasupathy, J. I. Goldsmith, C. Chang, Y. Yaish, J. R. Petta, M. Rinkoski, J. P. Sethna, H. D. Abruna, P. L. McEuen and D. C. Ralph, Nature **417**, 722 (2002).

[3] W. J. Liang, M. P. Shores, M. Bockrath, J. R. Long and H. Park, Nature **417**, 725 (2002).

[4] S. Kubatkin, A. Danilov, M. Hjort, J. Cornil, J. L. Bredas, N. Stuhr-Hansen, P. Hedegard and T. Bjornholm, Nature **425**, 698 (2003).

[5] L. H. Yu, Z. K. Keane, J. W. Ciszek, L. Cheng, M. P. Stewart, J. M. Tour and D. Natelson, Phys. Rev. Lett. **93** (2004).

[6] A. N. Pasupathy, R. C. Bialczak, J. Martinek, J. E. Grose, L. A. K. Donev, P. L. McEuen and D. C. Ralph, Science **306**, 86 (2004).

[7] D. H. Chae, J. F. Berry, S. Jung, F. A. Cotton, C. A. Murillo and Z. Yao, Nano Lett. **6**, 165 (2006).

[8] D. L. Klein, R. Roth, A. K. L. Lim, A. P. Alivisatos and P. L. McEuen, Nature **389**, 699 (1997).

[9] K. I. Bolotin, F. Kuemmeth, A. N. Pasupathy and D. C. Ralph, Appl. Phys. Lett. **84**, 3154 (2004).

[10] A. A. Houck, J. Labaziewicz, E. K. Chan, J. A. Folk and I. L. Chuang, Nano Lett. **5**, 1685 (2005).

[11] H. B. Heersche, Z. de Groot, J. A. Folk, L. P. Kouwenhoven, H. S. J. van der Zant, A. A. Houck, J. Labaziewicz and I. L. Chuang, Phys. Rev. Lett. **96**, 017205 (2006).

[12] L. P. Kouwenhoven, C. M. Marcus, P. L. McEuen, S. Tarucha, R. M. Westervelt and N. S. Wintergreen, in *Mesoscopic Electron Transport*, edited by L. P. Kouwenhoven, G. Schon and L. L. Shon (Kluwer Academic Publishers, Dordrecht, The Netherlands, 1996).

[13] L. P. Kouwenhoven, D. G. Austing and S. Tarucha, Rep. Prog. Phys. **64**, 701 (2001).

[14] M. R. Buitelaar, T. Nussbaumer and C. Schonenberger, Phys. Rev. Lett. **89**, 256801 (2002).

[15] Y. J. Doh, J. A. van Dam, A. L. Roest, E. Bakkers, L. P. Kouwenhoven and S. De Franceschi, Science **309**, 272 (2005).

[16] P. Jarillo-Herrero, J. A. van Dam and L. P. Kouwenhoven, Nature **439**, 953 (2006).

[17] H. Park, A. K. L. Lim, A. P. Alivisatos, J. Park and P. L. McEuen, Appl. Phys. Lett. **75**, 301 (1999).

[18] M. Tinkham, *Introduction to Superconductivity* (McGraw-Hill, New York, 1996).

[19] J. I. Gonzalez, T. H. Lee, M. D. Barnes, Y. Antoku and R. M. Dickson, Phys. Rev. Lett. **93**, 147402 (2004).

[20] R. C. Dynes, V. Narayanamurti and J. P. Garno, Phys. Rev. Lett. **41**, 1509 (1978).

[21] S. B. Kaplan, C. C. Chi, D. N. Langenberg, J. J. Chang, S. Jafarey and D. J. Scalapino, Phys. Rev. B **14**, 4854 (1976).

[22] B. N. Brockhouse, T. Arase, G. Caglioti, K. R. Rao and A. D. B. Woods, Phys. Rev. **128**, 1099 (1962).

[23] D. J. Scalapino, J. R. Schrieffer and J. W. Wilkins, Phys. Rev. **148**, 263 (1966).

[24] R. D. Parks, *Superconductivity* (Dekker, New York, 1969).

Chapter 6: Superconducting Single-Electron Transistors

6.1 INTRODUCTION

Superconducting single-electron transistors (SSETs) have been investigated intensively in the last two decades for various topics, such as the parity effect [1-5] and quantum computation [6-10]. An SSET consists of a small superconducting island that is coupled to two superconducting electrodes through small tunnel junctions. A gate electrode is capacitively coupled to the island and can be used to manipulate the charge states of the island. In the previous study, two techniques have been developed to fabricate SSETs, including planar Al superconducting devices with the angle evaporation technique [1] and vertical Al superconducting devices with the nanopore technique [11]. However, both of these techniques involve elaborate fabrication process. The devices can only be investigated at milliKelvin temperature due to their relatively small energy scales, which severely hinders the research progress in this field.

In this chapter, we present the realization and characterization of Pb SSETs. The Pb SSETs are fabricated by applying electromigration to Pb nanowires. During the electromigration process, Pb nanoparticles are formed simultaneously. Our SSETs consist of the resultant Pb nanoparticles coupled to the Pb electrodes with an Al back gate electrode. Due to the small size of the nanoparticles, the devices show the Coulomb charging energy of ~11 meV. The superconducting gap of Pb is ~1.3 meV and the transition temperature is ~7 K, which enables the study of superconductivity-related single-electron transport behavior at liquid helium temperature. The normal metallic single-electron tunneling behavior can be recovered by suppressing the superconductivity upon the application of an external magnetic field or by increasing the temperature. Additionally, fine conductance features are observed with odd-even parity effect at 2 K, which are smeared out at 4 K. These features can be attributed to the tunneling process involving singularity matching.

6.2 DEVICE FABRICATION

The fabrication process of Pb nanowires has been presented in the previous chapter. Cr/Au (5nm/25nm) contact pads and a 30 nm thick Al gate electrode are first fabricated on top of oxidized Si substrates by using photolithography. Electron-beam lithography using standard PMMA/P(MMA-MAA) bilayer resist is then performed to define the Pb wire, which is ~500 nm in width and has a constriction of ~100 nm in the middle. Angle evaporation followed by lift-off process is used to deposit Pb wires. The Pb nanowires are cooled down to 4.2 K and electromigration process [12, 13] is applied. It is well known that gold nanoparticles can form during electromigration [14-18]. In our study, small Pb nanoparticles simultaneously form during the electromigration process in the nanogaps and lead to the resultant nanoparticle single-electron transistors (SETs). We have broken 347 Pb nanowires. Among them, 14 devices exhibit conductance suppression at low bias with gate modulation and are identified as SSETs.

Fig 6.1 shows a schematic of a Pb SSET and its schematic energy diagram at zero bias voltage and zero gate voltage. The Pb superconducting central island is connected to the source/drain electrodes through two tunnel junctions and capacitively coupled to the underneath Al gate electrode. The tunnel junctions are characterized by the tunneling resistances and capacitances.

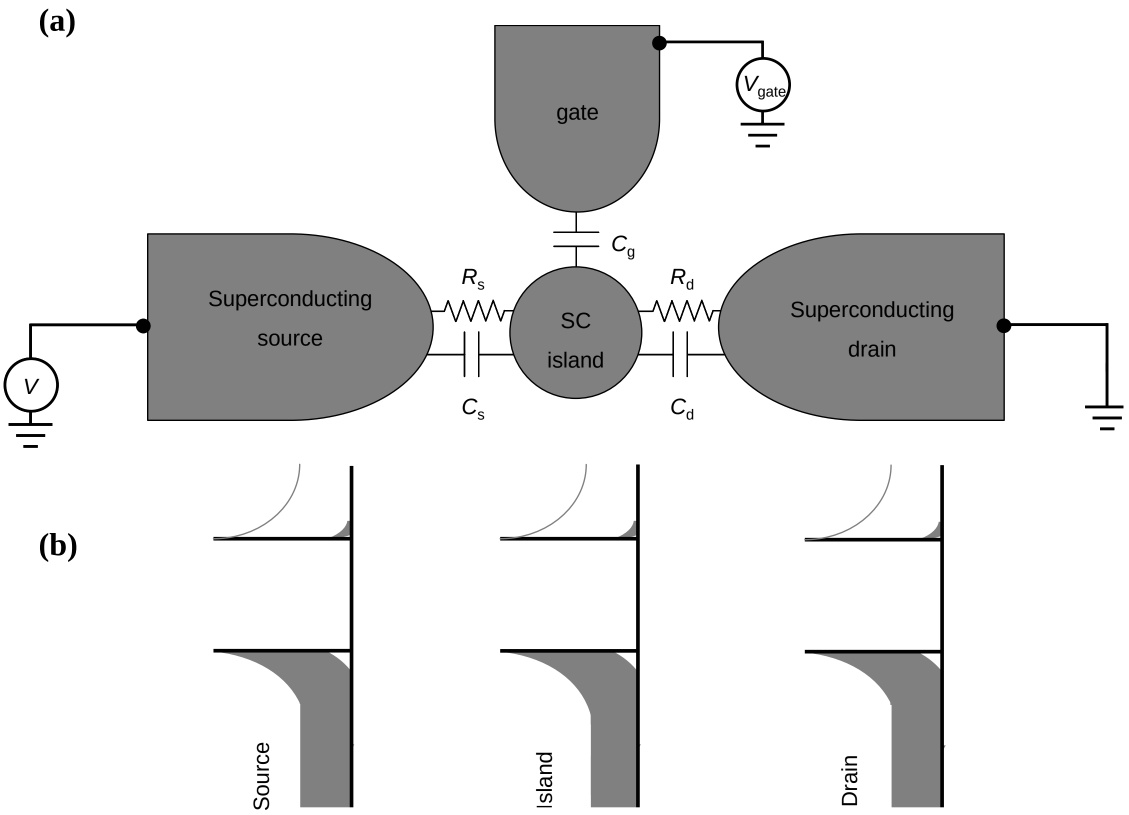

Figure 6.1: (a) Schematic diagram of an SSET. (b) Schematic energy diagram.

6.3 SEQUENTIAL TUNNELING OF QUASIPARTICLES

To avoid oxidation of the Pb, the transport properties of SSETs are investigated at 4.2 K immediately after electromigration without warming up and exposure to air. Current-voltage (*I*-*V*) characteristics of a representative SSET (sample #1) are measured at various gate voltages applied to the Al gate electrodes and plotted in Fig 6.2. The current is suppressed at low bias voltage and the size of the voltage gaps can be modulated with the application of a gate voltage.

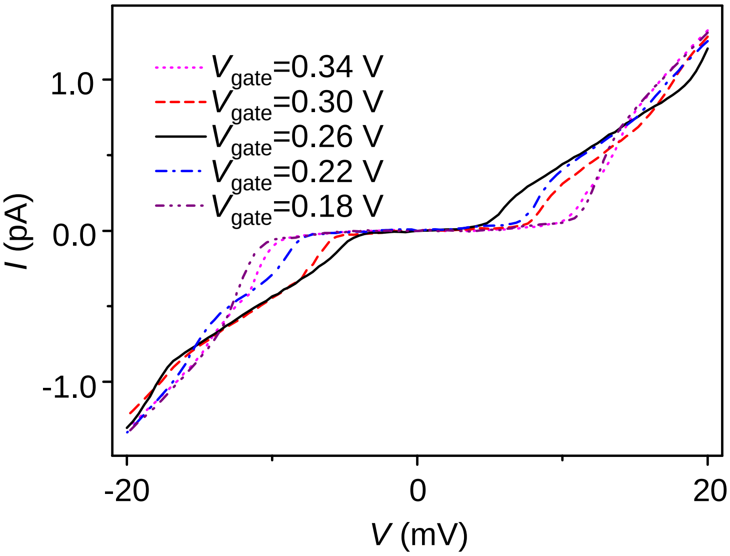

Figure 6.2: Representative *I*-*V* characteristics from sample #1 at different gate voltages measured at 4.2 K.

Numerical differentiation is then carried out on the *I*-*V* characteristics to obtain the differential conductance. The conductance as a function of bias and gate voltage at T = 4.2 K is plotted in Fig 6.3 (a) and (b) for sample #1 and #2 respectively. The conductance is suppressed around zero bias. There are five suppression regimes that can be identified in the gate range of device #1. The boundaries of the suppression regimes of device #1 are offset to high bias and intersect at the bias voltages of ~5.2 mV and ~16.2 mV. Sample #1 is then measured at the magnetic field B = 1.9 T. Fig 6.3 (c) shows the two-dimensional plot of conductance as a function of bias and gate voltages for sample #1. Five diamond-shaped regions are observed in which the conductance is suppressed. The boundaries of the five diamond-shaped regions intersect at zero bias voltage compared with the plot in Fig 6.3 (a).

The critical field of bulk Pb is $H_C = 0.0803\,\mathrm{T}$. However, due to its geometry, the length scale of the devices are comparable to the penetration length of Pb ~32 nm, and a field much larger than H_C is required to fully suppress the superconductivity of the electrodes and the island. The magnetic field B = 1.9 T is large enough to suppress the superconductivity of sample #1. The features observed in Fig 6.3 (c) are characteristic of the Coulomb blockade in normal metallic SETs. We believe that the features observed in Fig 6.3 (a) and (b) are related to the superconductivity. In the low bias region, the conductance is suppressed by not only the Coulomb blockade effect but also by the absence of available quasiparticles in the superconducting gap. As the bias voltage increases, the quasiparticles can be created on the island and the electrodes. These quasiparticles can tunnel through the device, which results in the onset of the high conductance regime. A schematic energy diagram of this transport is depicted in Fig 6.4 (a). The transport consists of two tunneling steps: the initial tunneling and the final tunneling. In both tunneling steps, a bias voltage of 2Δ is required to break a Cooper pair to create quasiparticle tunneling. Therefore, a minimum energy requirement of 4Δ is mandatory. The thresholds of this sequential tunneling of quasiparticles created by bias voltage can be obtained by solving [19]:

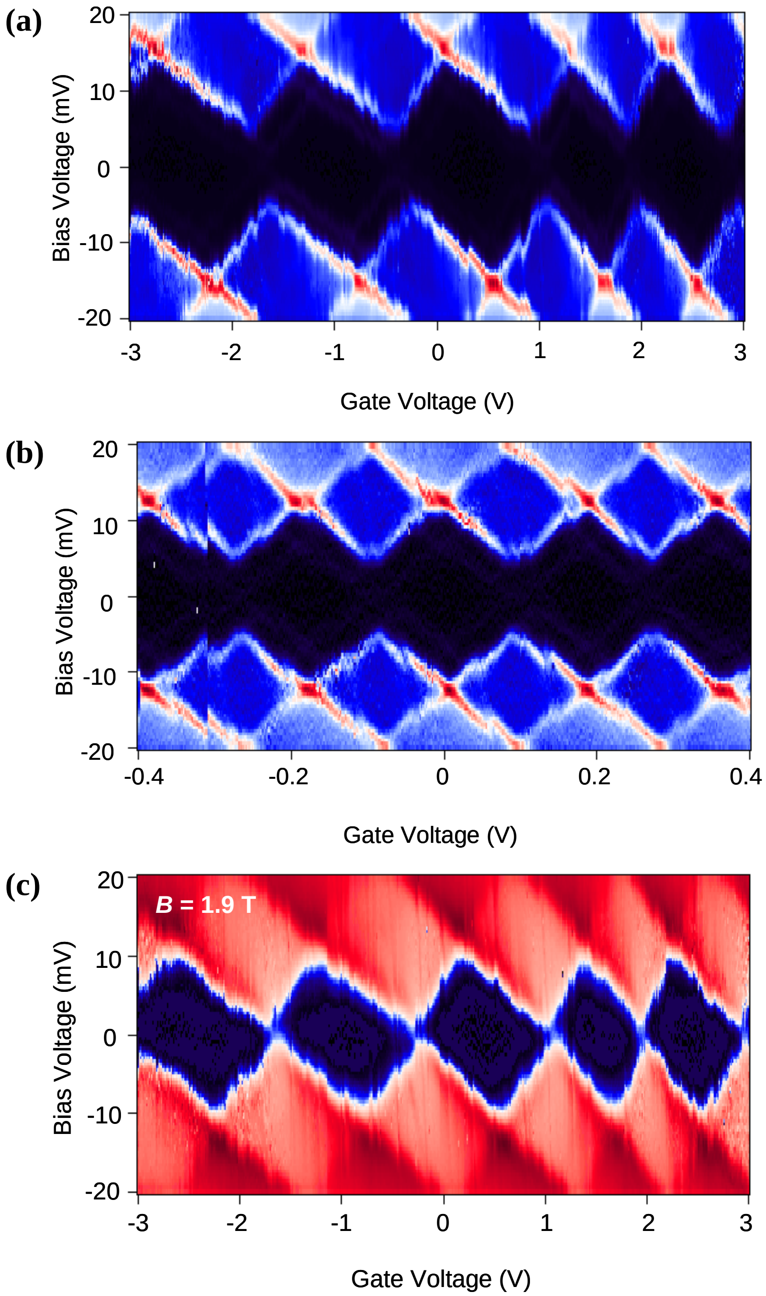

Figure 6.3: Two-dimensional color plot of conductance as a function of bias voltage and gate voltage from (a) sample #1, (b) sample #2 at T = 4.2 K and zero B fields and (c) sample #1 at T = 4.2 K and B = 1.9 T. A blue (red) color corresponds to high (low) conductance. The plotted conductance ranges from zero to (a) 7×10^{-9} S, (b) 3×10^{-10} S and (c) 4×10^{-9} S

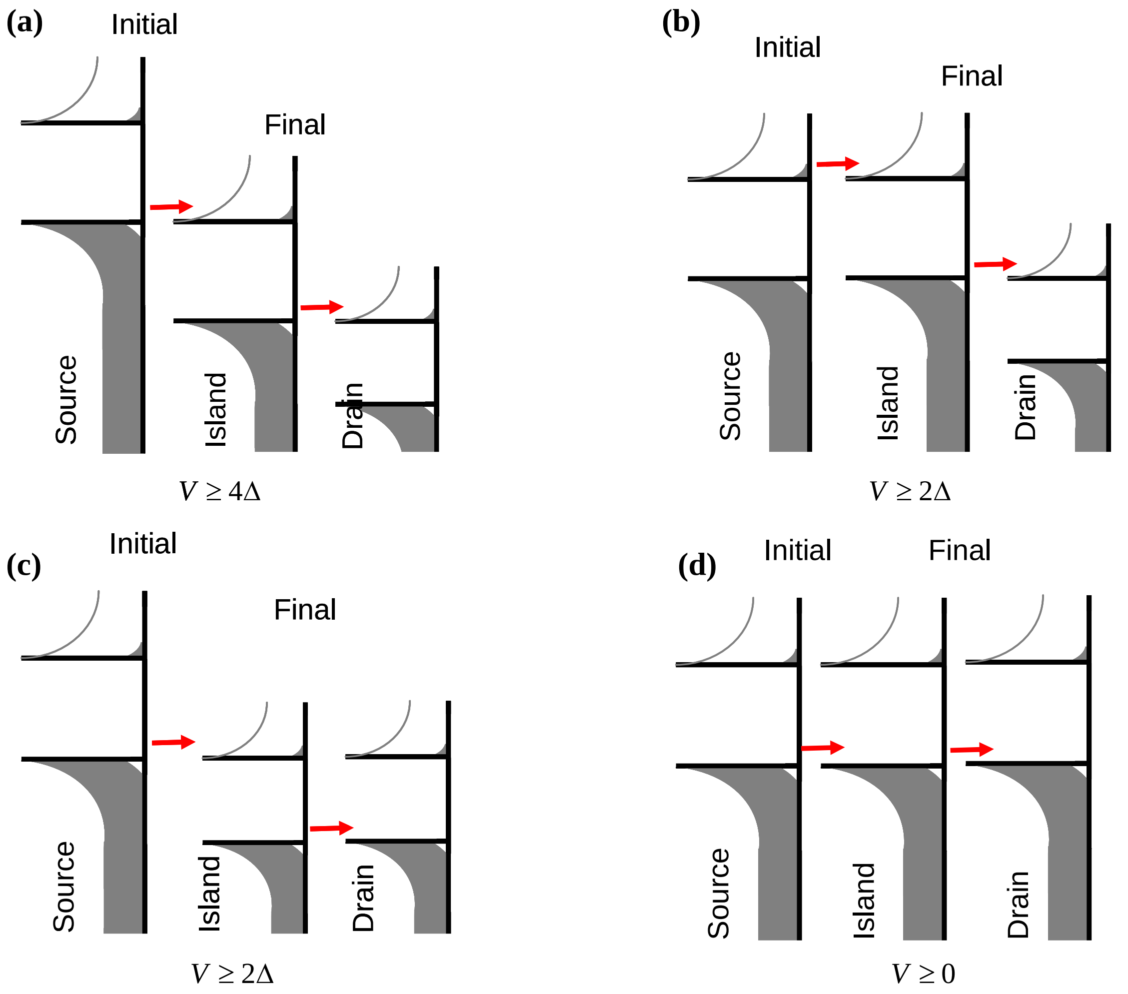

Figure 6.4: Schematic energy diagrams of various quasiparticle tunneling processes. (a) Sequential tunneling of quasiparticle. (b) Quasiparticle tunneling involving singularity matching as the initial tunneling process. (c) Quasiparticle tunneling involving singularity matching as the final tunneling process. (d) Quasiparticle tunneling involving singularity matching happening as both the initial and final tunneling processes. The red lines correspond to the quasiparticle tunneling processes in the transport.

$$\frac{e}{C_{tot}}\left(\left(N-\frac{1}{2}\right)-VC_s-V_gC_g\right)+2\Delta=0 \qquad (6.1)$$

and $$\frac{e}{C_{tot}}\left(\left(N-\frac{1}{2}\right)+VC_{tot}-VC_s-V_gC_g\right)+2\Delta=0 \qquad (6.2)$$

These equations consider both the Coulomb blockade effect and the superconducting gap. We calculated the thresholds for sequential tunneling of quasiparticles in sample #1. The capacitances of sample #1 can be extracted from the plot in Fig 6.3 (c) in the following way. The Coulomb charging energy is E_C ~11 meV. The total capacitance is $C_{tot}=\frac{e^2}{E_C}=\frac{1.6\times10^{-19}}{11\times10^{-3}}=14.5\,\text{aF}$. From the slopes of the boundaries of the blockade regime, the ratios of capacitances are $\frac{C_g}{C_s}=0.012$ and $\frac{C_g}{C_g+C_d}=0.028$. Therefore, $C_g=0.12\,\text{aF}, C_d=4.22\,\text{aF},$ and $C_s=10.20\,\text{aF}$. The calculated threshold for sequential tunneling of quasiparticles of sample #1 is plotted in Fig 6.5 as the dark solid lines. They agree well with the observed thresholds in Fig 6.3 (a). Here, the superconducting gap Δ for electrodes and island may be different, but we could not resolve the difference. Therefore, we assume them to be the same in my analysis. By comparing the calculated thresholds with the observation in Fig 6.3 (a), we find that the offset of the boundaries of the suppression regimes in the superconducting state equals 4Δ. This gives the superconducting gap of the Pb island and electrodes, which is $\Delta=1.3\,\text{meV}$. This value is consistent with the superconducting gap of bulk Pb, ~1.365 mV [20] even though the size of the Pb nanoparticle in our devices is much smaller than the intrinsic coherence length of Pb ξ_0~83 nm [20]. We assume a sphere Pb island between two parallel Pb plate electrodes, the size of the Pb island can be estimated as $r\sim10\,\text{nm}$, where r is the radius of the island. This is not surprising since the superconducting gap changes significantly only when the quantum energy level spacing is comparable with the superconducting gap [21]. The quantum energy level spacing of a Pb nanoparticle with $r \sim 10\,\text{nm}$ is $\Delta E = 2E_F/3N \approx 6\,\mu\text{eV}$, where E_F = 9.37 eV is the Fermi energy of Pb, N is the total number of electrons on the nanoparticle [20]. This energy level spacing is much smaller than 1.3 meV.

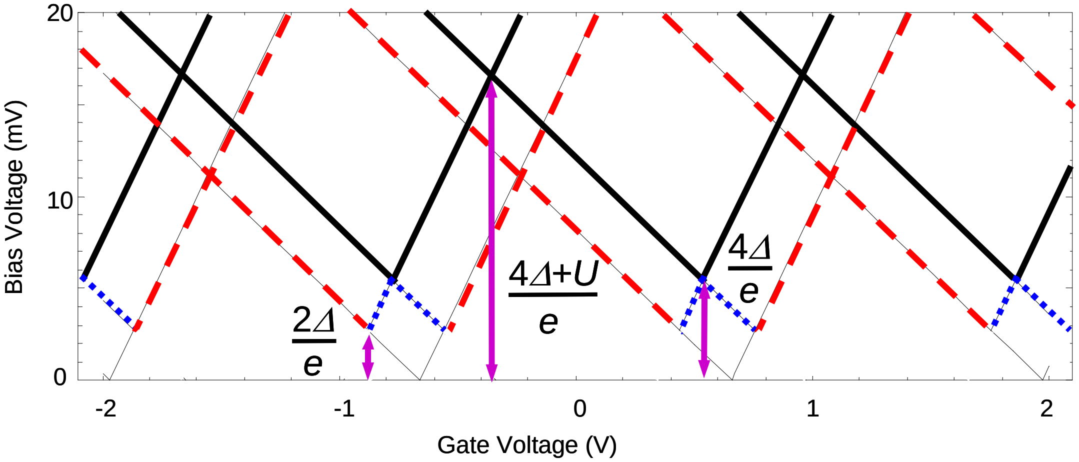

Figure 6.5: Thresholds of various quasiparticle tunneling processes in SSETs. Black solid lines represent that of quasiparticle sequential tunneling. Red dashed and blue dotted lines correspond to quasiparticle tunneling involving singularity matching happening as the initial tunneling or the final tunneling respectively. Thin solid lines correspond to quasiparticle tunneling involving singularity matching happening in both the initial and final tunneling processes.

6.4 SINGULARITY MATCHING

We observed interesting fine features in the suppression regime of Fig 6.3 (a) and (b). For clarity, Fig 6.3 (a) and (b) are redrawn in the low bias region in Fig 6.6 (a) and (b) respectively. There are additional fine conductance features running parallel to the boundaries of the suppression regions corresponding to extremely conductance signals. Dashed yellow lines are used to highlight these features in the plots of Fig 6.6 (a) and (b).

Various transport features have previously been observed in the suppression regime of the Al SSETs, such as the Josephson-quasiparticle cycle (JQP) [1], Andreev reflection (AR) [22], and 3*e* tunneling processes [19]. The magnitudes of the transport current involving JQP, AR and 3e tunneling processes can be estimated as $I_0 = \Delta / 4eR_n$, R_n is the tunneling resistance, in our devices, it is $\sim 2 \times 10^{10}\ \Omega$ and leads to $I_0 \leq 8 \times 10^{-15}\ \mathrm{A}$. This current is too small to be resolved in our system. We further calculate the thresholds of these processes with the parameters of sample #1. The results of calculation do not coincide with the features observed in Fig 6.3 (a) and Fig 6.6 (a).

Another feasible mechanism for the observed fine features is the processes including quasiparticle tunneling caused by singularity matching [23, 24]. In the singularity matching process, the quasiparticles tunnel between the electrode and the island when the singularities of the density of states are aligned. There are three kinds of transport involving singularity matching.

In case one, the initial tunneling is singularity matching. The quasiparticles tunnel between the source electrode and the island. Here, these quasiparticles are not created by bias voltage as the tunneling process described in previous section, but are either created by thermal excitations or due to the unpaired electron. The latter mechanism will be discussed in detail later. After the initial tunneling, the tunneling of quasiparticles created by bias voltage returns the system to its original state and the transport can start over again. The energy diagram of this transport is depicted in Fig 6.4 (b). The thresholds of this transport are determined by the initial tunneling and can be obtained by solving:

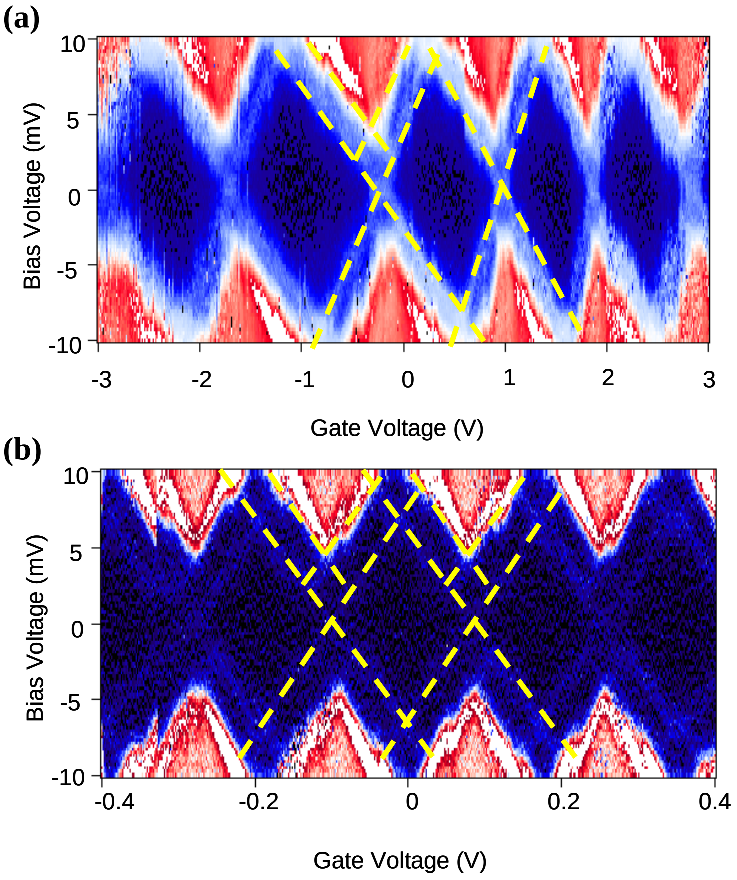

Figure 6.6: Two-dimensional color plot of conductance as a function of bias voltage and gate voltage from (a) sample #1, and (b) sample #2 at T = 4.2 K and zero B fields in the low bias region to clarify the fine features in suppression regimes. The dashed yellow lines are used to indicate these features. A blue (red) color corresponds to low (high) conductance. The plotted conductance ranges from zero to (a) 2×10^{-9} S and (b) 1×10^{-9} S.

$$\frac{e}{C_{tot}}\left(\left(N-\frac{1}{2}\right)-VC_s-V_{gate}C_g\right)=0 \tag{6.3}$$

$$\frac{e}{C_{tot}}\left(\left(N-\frac{1}{2}\right)+VC_{tot}-VC_s-V_{gate}C_g\right)=0 \tag{6.4}$$

From the energy diagram, we can clearly see that 2Δ energy is required in the final tunneling to create quasiparticles. Therefore, the thresholds can only be observed at bias voltage greater than 2Δ.

In case two, the final tunneling is singularity matching. A quasiparticle created by the bias voltage first tunnels onto the island, and subsequently tunnels to the drain electrode through singularity matching to return the system to its original state. The energy diagram is depicted in Fig 6.4 (c). The thresholds of the transport in this case are:

$$\frac{e}{C_{tot}}\left(\left(N-\frac{1}{2}\right)-VC_s-V_{gate}C_g\right)+2\Delta=0 \tag{6.5}$$

$$\frac{e}{C_{tot}}\left(\left(N-\frac{1}{2}\right)+VC_{tot}-VC_s-V_{gate}C_g\right)+2\Delta=0 \tag{6.6}$$

These thresholds coincide with the thresholds of sequential tunneling of quasiparticles described in previous section. But in this case, the final tunneling is singularity matching. Therefore no 2Δ energy is required. From the energy diagram, we can see that 2Δ energy is required in the initial tunneling to create quasiparticles. Thus, the thresholds can be observed at bias voltage greater than 2Δ while the thresholds of sequential tunneling of quasiparticles can only be observed when the bias voltage is greater than 4Δ.

In case three, both the initial and final tunneling are singularity matching. The energy diagram is depicted in Fig 6.7 (d). The thresholds are given as:

$$\frac{e}{C_{tot}}\left(\left(N-\frac{1}{2}\right)-VC_s-V_{gate}C_g\right)=0 \tag{6.7}$$

$$\frac{e}{C_{tot}}\left(\left(N-\frac{1}{2}\right)+VC_{tot}-VC_s-V_{gate}C_g\right)=0 \tag{6.8}$$

These thresholds are the same as the thresholds of case one. But in this case, no bias voltage is required to create quasiparticles in the transport, therefore the transport features can be observed even at the bias voltage smaller than 2Δ.

With the values of capacitances of sample #1, all the above thresholds are calculated and shown in Fig 6.5. The red dashed lines, blue dotted lines and gray solid lines are the thresholds of the transport in case one, two and three respectively. The plotted patterns agree well with the features observed in Fig 6.3 (a) and Fig 6.4 (a), which justifies our discussion that these features originate from the tunneling process caused by singularity matching.

6.5 ODD-EVEN EFFECT

The conductance features originate from the transport involving both singularity matching and sequential tunneling of quasiparticles. The strength of sequential tunneling of quasiparticles is independent of the temperature, because the quasiparticles in these tunneling are created by bias voltage. The strength of singularity matching depends on the number of quasiparticles on the island [24].The temperature dependence of the devices is measured as well. Sample #1 is then measured at T = 2 K. The two-dimensional plot of conductance as a function of bias and gate voltage is shown in Fig 6.7. Compared with the plot in Fig 6.6 (a), the fine conductance features exhibit odd-even effect, i.e., these features appear the same as those in Fig 6.6 (a) in the suppression regimes of N-2, N, and N+2 charge states and disappear in the suppression regimes of N-1, N+1 and N+3 charge states. At the bias voltage smaller than 2Δ or 2.6 mV, all fine features are not observed.

The conductance features originate from the transport involving both singularity matching and sequential tunneling of quasiparticles. The strength of sequential tunneling of quasiparticles is independent of the temperature, because the quasiparticles in these tunneling are created by bias voltage. The strength of singularity matching depends on the number of quasiparticles on the island [24]. As temperature decreases, the number of thermally excited quasiparticles decreases. The appearance of the odd-even effect must be related to the number of quasiparticles on the island. The number of thermal excited quasiparticles decreases to one at a temperature T^*, and vanishes rapidly at the temperature below T^* [24]. $T^* = \frac{\Delta}{k_B \ln N_{eff}}$, where N_{eff} is essentially the total number of quasiparticle states within $k_B T$ above the gap in the entire island volume given by $N_{eff} \approx 2\sqrt{2} V \rho(0) \times (\Delta / k_B T)^{1/2}$ [3], where V is the volume of the Pb nanoparticle, $\rho(0)$ is the normal-metal density of states (including spin) per unit volume at the Fermi energy. For sample #1, the radius is 10 nm, $\Delta = 1.3\,\mathrm{meV}$. We use $\rho(0) = \frac{3N}{2E_F}$, where N is the total number of electrons on the island and E_F = 9.37 eV for Pb. With these values, we can obtain that $N_{eff} \approx 1000$, which leads to $T^* = \frac{\Delta}{k_B \ln N_{eff}} \sim 3\,\mathrm{K}$. This value of T^* indicates that the number of thermally excited quasiparticles is zero at T = 2 K, and larger than one at T = 4.2 K.

At 2 K, there are no thermally excited quasiparticles. For the process in case one, if the number of electrons on the Pb island is even, at T = 2 K, all the electrons are paired and there is no quasiparticles. Therefore, the singularity matching is not possible, and the conductance features disappear. However, if the total number of electrons on the Pb island is odd, at T = 2 K, there is one unpaired electron which makes the number of quasiparticles one. Therefore, the tunneling involving singularity matching is possible and the conductance features remain. For the transport process in case two, the tunneling of singularity matching is the final step and its strength is determined by the number of quasiparticles on the island after the initial tunneling. If the island is in even charge state, after the initial tunneling, there is an odd number of electrons on the island, the singularity matching can happen as the final tunneling. But if the island has an odd number of electrons, the initial tunneling will put the island into even charge state. There is no available quasiparticle for the final tunneling of singularity matching

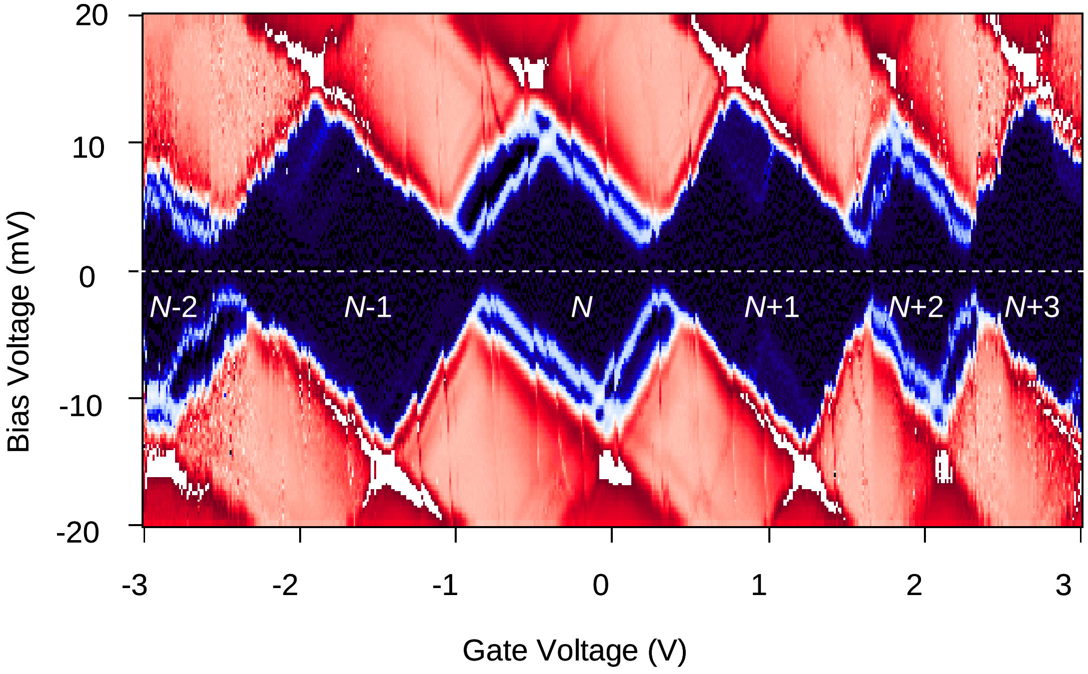

Figure 6.7: Two-dimensional plot of differential conductance as a function of bias voltage and gate voltage at T = 2 K. A blue (red) color corresponds to low (high) conductance. The plotted conductance ranges from zero to 4×10^{-9} S.

and the conductance features will not be observed. With the above analysis, the N-2, N and N+2 charge states can be naturally associated with the odd charge states and the others even charge states.

With similar analysis, we can understand the disappearance of the fine features at the bias voltage smaller than 2Δ. These features correspond to the transport in case three in which both tunneling steps involve singularity matching. At 2 K, if the Pb island is in the even state, the initial singularity matching is not possible. If the Pb island is in the odd charge state, after the initial tunneling, there is an even number of electrons. The number of quasiparticles on the island is zero and the final singularity matching is not possible. Thus In both even and odd charge states, these features can not be observed at 2 K.

6.6 SUMMARY

In summary, we have successfully fabricated Pb SSETs by electromigration of Pb nanowires. In the superconducting state, the conductance is suppressed due to the Coulomb blockade effect and the absence of available states in the superconducting gap. Within the region of suppressed conductance, fine structures are observed that can be attributed to quasiparticle tunneling processes involving singularity matching. These features exhibit a strong odd-even parity effect at 2 K and become smeared out at 4.2 K.

REFERENCES

[1] T. A. Fulton, P. L. Gammel, D. J. Bishop, L. N. Dunkleberger and G. J. Dolan, Phys. Rev. Lett. **63**, 1307 (1989).

[2] D. V. Averin and Y. V. Nazarov, Phys. Rev. Lett. **69**, 1993 (1992).

[3] M. T. Tuominen, J. M. Hergenrother, T. S. Tighe and M. Tinkham, Phys. Rev. Lett. **69**, 1997 (1992).

[4] P. Lafarge, P. Joyez, D. Esteve, C. Urbina and M. H. Devoret, Phys. Rev. Lett. **70**, 994 (1993).

[5] P. Joyez, P. Lafarge, A. Filipe, D. Esteve and M. H. Devoret, Phys. Rev. Lett. **72**, 2458 (1994).

[6] Y. Nakamura, Y. A. Pashkin and J. S. Tsai, Nature **398**, 786 (1999).

[7] Y. Makhlin, G. Schon and A. Shnirman, Rev. Mod. Phys. **73**, 357 (2001).

[8] D. Vion, A. Aassime, A. Cottet, P. Joyez, H. Pothier, C. Urbina, D. Esteve and M. H. Devoret, Science **296**, 886 (2002).

[9] J. Mannik and J. E. Lukens, Phys. Rev. Lett. **92** (2004).

[10] J. Aumentado, M. W. Keller, J. M. Martinis and M. H. Devoret, Phys. Rev. Lett. **92** (2004).

[11] J. von Delft and D. C. Ralph, Phys. Rep. **345**, 61 (2001).

[12] H. Park, A. K. L. Lim, A. P. Alivisatos, J. Park and P. L. McEuen, Appl. Phys. Lett. **75**, 301 (1999).

[13] D. H. Chae, J. F. Berry, S. Jung, F. A. Cotton, C. A. Murillo and Z. Yao, Nano Lett. **6**, 165 (2006).

[14] J. I. Gonzalez, T. H. Lee, M. D. Barnes, Y. Antoku and R. M. Dickson, Phys. Rev. Lett. **93**, 147402 (2004).

[15] A. A. Houck, J. Labaziewicz, E. K. Chan, J. A. Folk and I. L. Chuang, Nano Lett. **5**, 1685 (2005).

[16] R. Sordan, K. Balasubramanian, M. Burghard and K. Kern, Appl. Phys. Lett. **87**, 013106 (2005).

[17] H. B. Heersche, Z. de Groot, J. A. Folk, L. P. Kouwenhoven, H. S. J. van der Zant, A. A. Houck, J. Labaziewicz and I. L. Chuang, Phys. Rev. Lett. **96**, 017205 (2006).

[18] T. Taychatanapat, K. I. Bolotin, F. Kuemmeth and D. C. Ralph, Nano Lett. **7**, 652 (2007).

[19] P. Hadley, E. Delvigne, E. H. Visscher, S. Lahteenmaki and J. E. Mooij, Phys. Rev. B **58**, 15317 (1998).

[20] C. Kittel, *Introduction to Solid State Physics* (Wiley, New York, 2004).

[21] P. W. Anderson, J. Phys. Chem. Solids **11**, 26 (1959).

[22] R. J. Fitzgerald, S. L. Pohlen and M. Tinkham, Phys. Rev. B **57**, R11073 (1998).

[23] Y. Nakamura, A. N. Korotkov, C. D. Chen and J. S. Tsai, Phys. Rev. B **56**, 5116 (1997).

[24] A. J. Manninen, Y. A. Pashkin, A. N. Korotkov and J. P. Pekola, Europhys. Lett. **39**, 305 (1997).

Chapter 7: Ongoing Project: Single-Molecule Transistors

7.1 INTRODUCTION

In the past several years, electronic transport through nanostructures in the presence of superconducting electrodes has been studied intensively. These studies cover various nanostructures, including two-dimensional systems – graphene [1, 2] and one dimensional systems – carbon nanotube [3-8], as well as the zero dimensional systems – nanoparticles [9, 10]. In most of the studies, Al was used as the superconducting electrode material and the experiments were all carried out in a dilution refrigerator. Recently, individual molecules have been incorporated in transistor geometry, i.e. between the source and the drain electrodes with a gate electrode nearby [11-18] . The electron transport through individual molecules has been investigated. Transport in these devices at low temperature is dominated by single-electron tunneling [19] or the Coulomb blockade effect, which has provided a new spectroscopic tool to investigate the states at the level of individual molecules. These measurements have revealed a number of interesting phenomena including strong coupling of electron transport with molecular vibrational excitations [11, 16, 18], and the Kondo effect [12, 13, 15] due to correlations between unpaired electrons in the molecules and conduction electrons in the electrodes. However, superconductivity-related transport in individual molecules has not been studied due to the lack of successful fabrication of superconducting electrodes with nanometer-sized separation.

In Chapter 5, we presented work demonstrating successful fabrication of superconducting Pb electrodes with nanometer-sized separation. By incorporating individual molecules into the nanogaps, single-molecule transistors (SMTs) with superconducting electrodes can be realized.

In our work, we use Co-porphyrin to fabricate SMTs with the following motivation. Co-porphyrin is one species of metalloporphyrins, which work as important functional units in biological systems, such as photosynthetic units in plant and heme proteins in blood [20]. In the previous studies of Co-porphyrin SMTs with normal metal electrodes [21], a broad family of interesting transport phenomena have been observed including cotunneling and the Kondo effect. In this chapter, the fabrication process of Co-porphyrin SMTs with superconducting electrodes will first be presented and the preliminary experimental results of SMTs and discussions follow.

7.2 DEVICE FABRICATION

A schematic diagram of a Co-porphyrin SMT with superconducting Pb electrodes is shown in Fig 7.1. A diluted (~0.2 μM) solution of Co-porphyrin in dichloromethane is spin-deposited on pre-fabricated Pb nanowires at a speed of 1000 RPM. Then, the electromigration process is applied to the Pb nanowires at liquid helium temperature; in-situ electronic transport measurement follows immediately. The transport measurement shows that most devices exhibit tunneling between the superconducting electrodes without any gate dependence, but ~5% of the devices exhibit the conductance suppression in the low bias region with gate modulation. For these devices, conductance is measured in detail as a function of bias voltage and gate voltage by numerically differentiating *I*-*V* curves at different gate voltages. As will be discussed later, these current features can only be associated with the presence of Co-porphyrin molecules bridging into the nanogaps, but not the Pb nanoparticles formed simultaneously during electromigration.

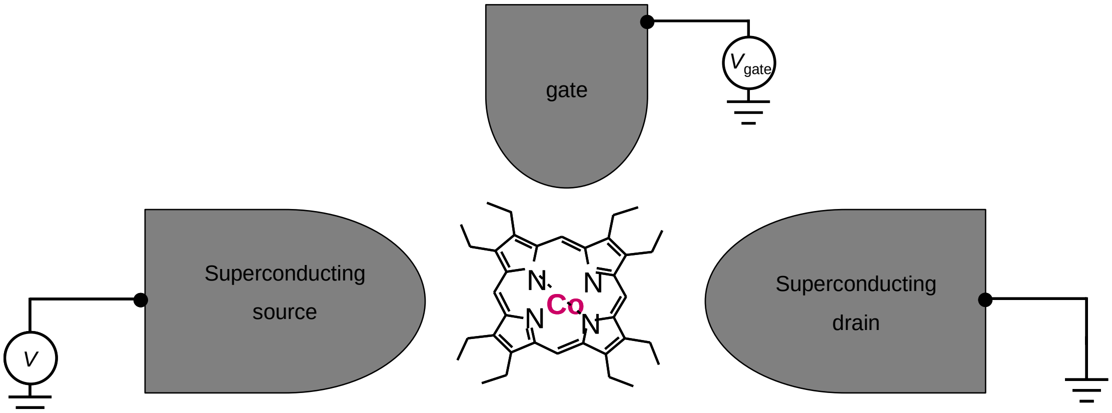

Figure 7.1: Schematic of a Co-porphyrin single-molecule transistor with superconducting electrodes.

7.3 EXPERIMENTAL RESULTS AND DISCUSSION

Fig 7.2 (a) shows the two-dimensional color plot of differential conductance as a function of bias voltage and gate voltage for a Co-porphyrin device at 4.2 K, which shows some generic features of the Coulomb blockade: the conductance is suppressed at low bias voltage and the size of the bias voltage gap are modulated by a gate voltage. Sky blue dashed lines are used to indicate the boundaries of the Coulomb suppression regimes. Two Coulomb diamonds can be identified with three degeneracy points. Interestingly, we observed two horizontal line features in both these two suppression regimes. Green dashed lines are drawn in Fig 7.2 (a) to indicate these features. These features intersect the boundaries of the suppression regimes at the bias voltage of 2.6 mV. The device is measured with a magnetic field B = 0.6 T. The two-dimensional color plot of differential conductance as a function of bias voltage and gate voltage is shown in Fig 7.2 (b). The features in the left suppression regime disappear. In the right suppression regime, a conductance peak at zero bias voltage is observed.

First, the Coulomb blockade behavior can not be associated with the Pb nanoparticles in the nanogaps which form during electromigration as discussed in chapter 6. In those devices, all charge states exhibit the same addition energy ~10 meV, which does not happen in Fig 7.2 (a) and (b). Furthermore, the zero-bias conductance peak show in Fig 7.2 (b) has never been observed in Pb SSETs and the features in the suppression regimes observed in Pb SSETs are not observed in this device. Therefore, the observed features must originate from the Co-porphyrin molecules.

The critical field of bulk Pb is $H_C = 0.0803\,\mathrm{T}$. However, due to its geometry, a field (~0.4 T) much larger than H_C is required to fully suppress the superconductivity of the electrodes and the island in our device. Nevertheless the magnetic field B = 0.6 T is large enough to suppress the superconductivity of the electrodes. The data shown in Fig 7.2 (b) should correspond to a Co-porphyrin SMT with normal metallic electrodes. The zero-bias conductance peak has been observed in the previous SMT studies with a variety of molecules including Co-porphyrin and are attributed to the Kondo effect [12, 13, 15, 16, 21, 22]. The Kondo effect involves the coherent superposition of a cotunneling process through the molecules which contain unpaired electron acting as localized spin. Suppose that the molecule and the electrodes are strongly coupled and there exists an unpaired spin in the molecule. The localized spin is antiferromagnetically coupled to the spin of conduction electrons in the source electrode by the spin exchange interaction. The localized spin can escape from the well state in the molecule virtually to the drain electrode since the Heisenberg uncertainty principle allows the process quantum mechanically for a short time around h/μ_0, where h is the Plank constant and μ_0 is the energy level of the electron below the Fermi energy. Within this time scale, another electron from the source electrode may occupy the same state with an opposite spin. This mechanism makes the localized spin effectively flip. Many such events introduce a tunneling density of states aligned to the Fermi energy of the two electrodes, leading to an enhancement of conductance or a conductance peak at zero bias at low temperatures. The Kondo effect vanishes above certain temperature, the so-called Kondo temperature T_K, which is determined by the spin exchange interaction. A good description of the Kondo effect in single-electron devices can be found in reference [23].

In Fig 7.2 (a), the electrodes are in superconducting state. The zero-bias conductance peak disappears and two conductance peaks appear at the bias voltage of 2.6 mV or 2Δ. The peaks at 2Δ can be explained as the onset of the quasiparticle cotunneling process. The cotunneling process happens when the lower singularity of density of states of the source electrode is aligned with the upper singularity of the density of states of the drain electrode. A quasiparticle can be created in the source electrode and tunnel into the molecule while at the same time another quasiparticle leaves the molecule and tunnels to the drain electrode. This process can give finite conductance peaks at the bias voltage of 2Δ.

We measured the temperature and magnetic field dependence of the conductance peak features. Fig 7.3 (a) plots the differential conductance versus bias voltage at a gate voltage of 2 V at the temperatures varying from 4.2 K to 8 K. As the temperature increases, the center of the two separated peaks moves to lower bias with the height decreasing. The peaks finally disappear as the temperature reaches 8 K. Fig 7.3 (b) shows the conductance as a function of bias voltage at magnetic fields varying from zero through 0.6 T. As the magnetic field increases, the conductance peak moves to lower bias and the peak height decreases. As the superconductivity is suppressed eventually by the magnetic field, the peak does not disappear; a single conductance peak at zero bias is

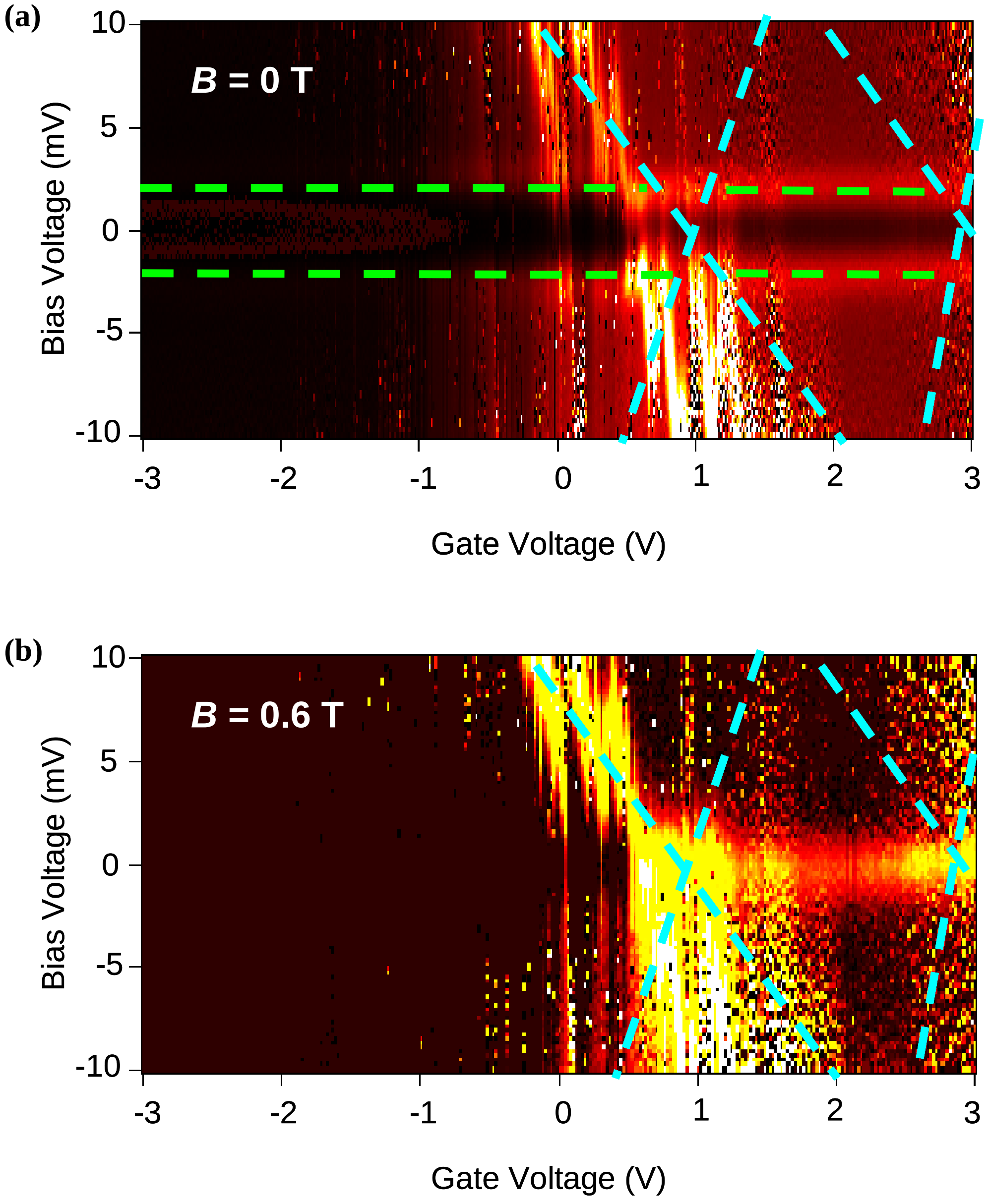

Figure 7.2: Two-dimensional color plot of conductance as a function of bias voltage and gate voltage from a Co-porphyrin SMT with superconducting electrodes at *T* = 4.2 K with (a) *B* = 0 T (b) *B* = 0.6 T. A light (dark) color corresponds to high (low) conductance. The plotted conductance ranges from 10^{-12} to 2×10^{-7} S. The sky blue dashed lines indicate the boundaries of the conductance suppression regimes. The green dashed lines indicate the horizontal line features observed when the electrodes are in superconducting state.

manifested.

This observation in Fig 7.3 could be explained by the competition between two energy scales. One is the superconducting gap Δ, which is the energy requirement to realize the cotunneling process described before. Another one the Kondo temperature: $k_B T_K$. If $\Delta > k_B T_K$, the Kondo effect is suppressed. Otherwise, if $\Delta < k_B T_K$, the Kondo effect survives. At zero magnetic field, $\Delta = 1.3\,\mathrm{meV} > k_B T_K$, where $T_K < 8\,\mathrm{K}$. As B increases, Δ decreases. At certain magnetic field, $\Delta < k_B T_K$ and the Kondo effect is allowed.

In Fig 7.3 (a), as temperature increases, the superconducting gap Δ decreases, which cause the peak position move to low bias and the peak height decrease. At T = 8 K, the superconductivity is suppressed and the Kondo effect is not observed. The Kondo peak height decreases as temperature increases [24] and vanishes above the Kondo temperature. The Kondo peak is not observed at T = 8 K, therefore, the Kondo temperature of this system must be lower than 8 K. The Kondo temperature $k_B T_K \leq 0.7\,\mathrm{meV}$ is less than the superconducting gap energy ~1.3 meV. This Kondo energy value is also much smaller than the previous observation [21]. In the plot of Fig 7.3 (a), as temperature increases, both the superconductivity and the Kondo effect are smeared out.

In Fig 7.3 (b), at low magnetic field, $\Delta > k_B T_K$, the cotunneling of quasiparticles is observed and the Kondo effect does not appear. As magnetic field increases, the superconducting gap Δ decreases to less than the Kondo energy, the Kondo effect is exhibited and the cotunneling process is suppressed. A single conductance peak is observed at zero bias as the signature of the Kondo effect at high magnetic field.

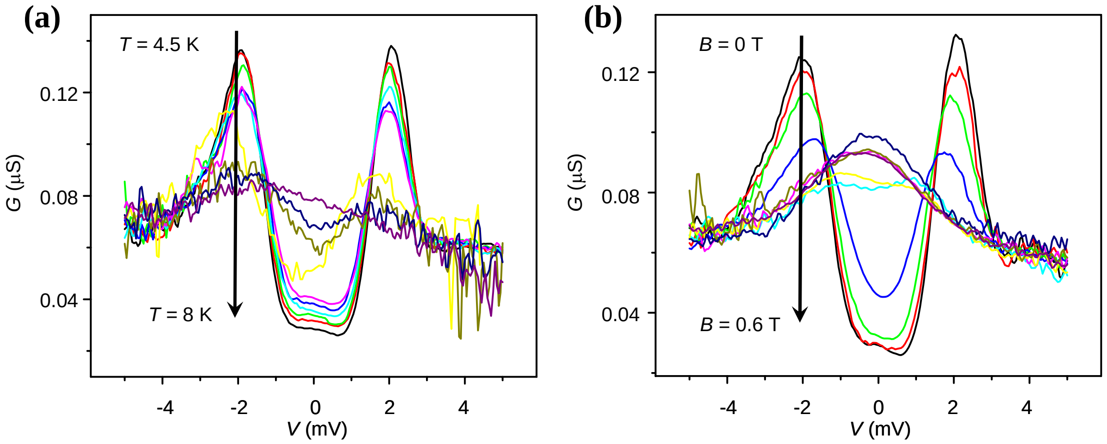

Figure 7.3: Differential conductance as a function of gate voltage from a Co-porphyrin SMT with superconducting electrodes at various temperatures and magnetic fields. (a) at temperatures of 4.5, 4.8, 5.0, 5.2, 5.4, 5.6, 6.0, 7.0, 7.5 and 8.0 K with zero magnetic fields. (b) with magnetic fields of 0, 0.05, 0.10, 0.15, 0.20, 0.25, 0.30, 0.40, 0.50, and 0.60 T at T = 4.2 K.

To gain more quantitatively understanding of these features, the transport through Co-porphyrin SMTs in different regimes should be studied with more samples. This project is still ongoing for more results.

REFERENCES

[1] C. W. J. Beenakker, Phys. Rev. Lett. **97** (2006).

[2] H. B. Heersche, P. Jarillo-Herrero, J. B. Oostinga, L. M. K. Vandersypen and A. F. Morpurgo, Nature **446**, 56 (2007).

[3] A. F. Morpurgo, J. Kong, C. M. Marcus and H. Dai, Science **286**, 263 (1999).

[4] A. Y. Kasumov, R. Deblock, M. Kociak, B. Reulet, H. Bouchiat, Khodos, II, Y. B. Gorbatov, V. T. Volkov, C. Journet and M. Burghard, Science **284**, 1508 (1999).

[5] M. R. Buitelaar, T. Nussbaumer and C. Schonenberger, Phys. Rev. Lett. **89** (2002).

[6] M. R. Buitelaar, W. Belzig, T. Nussbaumer, B. Babic, C. Bruder and C. Schonenberger, Phys. Rev. Lett. **91** (2003).

[7] H. I. Jorgensen, K. Grove-Rasmussen, T. Novotny, K. Flensberg and P. E. Lindelof, Phys. Rev. Lett. **96** (2006).

[8] P. Jarillo-Herrero, J. A. van Dam and L. P. Kouwenhoven, Nature **439**, 953 (2006).

[9] D. C. Ralph, C. T. Black and M. Tinkham, Phys. Rev. Lett. **74**, 3241 (1995).

[10] J. von Delft and D. C. Ralph, Phys. Rep. **345**, 61 (2001).

[11] H. Park, J. Park, A. K. L. Lim, E. H. Anderson, A. P. Alivisatos and P. L. McEuen, Nature **407**, 57 (2000).

[12] J. Park, A. N. Pasupathy, J. I. Goldsmith, C. Chang, Y. Yaish, J. R. Petta, M. Rinkoski, J. P. Sethna, H. D. Abruna, P. L. McEuen and D. C. Ralph, Nature **417**, 722 (2002).

[13] W. J. Liang, M. P. Shores, M. Bockrath, J. R. Long and H. Park, Nature **417**, 725 (2002).

[14] S. Kubatkin, A. Danilov, M. Hjort, J. Cornil, J. L. Bredas, N. Stuhr-Hansen, P. Hedegard and T. Bjornholm, Nature **425**, 698 (2003).

[15] A. N. Pasupathy, R. C. Bialczak, J. Martinek, J. E. Grose, L. A. K. Donev, P. L. McEuen and D. C. Ralph, Science **306**, 86 (2004).

[16] L. H. Yu, Z. K. Keane, J. W. Ciszek, L. Cheng, M. P. Stewart, J. M. Tour and D. Natelson, Phys. Rev. Lett. **93**, 266802 (2004).

[17] A. N. Pasupathy, J. Park, C. Chang, A. V. Soldatov, S. Lebedkin, R. C. Bialczak, J. E. Grose, L. A. K. Donev, J. P. Sethna, D. C. Ralph and P. L. McEuen, Nano Lett. **5**, 203 (2005).

[18] D. H. Chae, J. F. Berry, S. Jung, F. A. Cotton, C. A. Murillo and Z. Yao, Nano Lett. **6**, 165 (2006).

[19] L. P. Kouwenhoven, C. M. Marcus, P. L. McEuen, S. Tarucha, R. M. Westervelt and N. S. Wingreen, in *Mesoscopic Electron Transport*, edited by L. P. Kouwenhoven, G. Schon and L. L. Shon (Kluwer Academic Publishers, Dordrecht, The Netherlands, 1997).

[20] D. Dolphin, *The Porphyrins* (Academic, New York, 1978).

[21] D. H. Chae, Ph. D. Thesis, the University of Texas at Austin, (2006).

[22] L. H. Yu, Z. K. Keane, J. W. Ciszek, L. Cheng, J. M. Tour, T. Baruah, M. R. Pederson and D. Natelson, Phys. Rev. Lett. **95**, 256803 (2005).

[23] L. Kouwenhoven and L. Glazman, Phys. World **14**, 33 (2001).

[24] D. Goldhaber-Gordon, J. Gores, M. A. Kastner, H. Shtrikman, D. Mahalu and U. Meirav, Phys. Rev. Lett. **81**, 5225 (1998).

Chapter 8: Summary

In this thesis, we have discussed examples of single-electron transistors that are made from various nanoparticles, including gold nanoparticles, Pb nanoparticles. With these examples, we demonstrated that how single-electron tunneling spectroscopy can be used to explore the physics associated with various nanometer scale structures in normal and superconducting states.

To measure such small nanostructures, we demonstrate several techniques (Chapter 3) to fabricate gold electrodes with nanometer-sized gap. All these techniques are based on the electromigration breaking of nanowires. Metallic gold nanoparticle single-electron transistors are fabricated with these electrodes. The successful fabrication of SETs suggests that these electrodes can be suitable to wire-up the nanometer scale structures.

In the electron transport study of smaller gold nanoparticles (~1 nm) fabricated by the self-assembly of alkanedithiol molecules, large addition energies (>200 meV) are consistently observed due to the extreme small size of the gold nanoparticles, which enables the singe-electron tunneling operating at room temperature. Additionally, excitation features are observed accompanying the Coulomb blockade regime as extra conductance peaks outside of the suppression regime, which are associated with the vibrations of attached alkanedithiol molecule.

We adopted electromigration technique to Pb nanowire to create superconducting Pb electrodes with nanometer separation. The superconductivity of the electrodes are characterized by the tunneling spectroscopy, which agrees well with the conventional BCS theory. The superconducting Pb single-electron transistors are fabricated by incorporating Pb nanoparticles into the nanometer gaps. Various quasiparticle tunneling processes are investigated by electron transport spectroscopy.

The superconducting electrodes are suitable for single molecule study. Preliminary results from Co-porphyrin SMTs show promising new physics to be explored in this field, including the cotunneling of quasiparticles and the Kondo effect.

In this thesis, we discussed the fabrication and measurement of single-electron transistors with various nanoparticles. We found that the electron transport can be significantly modified by the interaction between conduction electrons and nanostructure internal degree of freedom. The results of this thesis can be utilized to investigate fundamental electronic properties of nanostructures and to develop novel electronic devices.

Vita

Kang Luo was born in Yingshan, Sichuan Province, the People's Republic of China on December 4th, 1976, the son of Yirong Luo and Cuibi Kang. After completing high school at Yingshan High School, Yingshan, Sichuan Province, China in 1995, he attended Peking University, Beijing, China, majoring in physics. After completing Bachelor's degree in Physics in 1999, he started his master project under the supervising of Professor Zheng-Xiang Gao in Physics department at Peking University. He carried out the vortex dynamics study of high temperature superconductors using magneto-optic imaging technique until he finished his master degree in July, 2001. In August 2001, he entered the Graduate School at the University of Texas at Austin.

Permanent address:
Fangyi Zhan, Yingshan, Sichuan Province, the People's Republc of China, 637700

This dissertation was typed by the author.